CHARACTERIZATION OF POST-ANNEALING MECHANICAL BEHAVIOR OF PREFORMED ALUMINUM ALLOY 5182-O

by

Jingjing Li

A dissertation submitted in partial fulfillment
of the requirements for the degree of
Doctor of Philosophy
(Mechanical Engineering)
in The University of Michigan
2011

Doctoral Committee:

Professor S. Jack Hu, Co-Chair

Paul E. Krajewski, Co-Chair, GM

Professor J. Wayne Jones

Professor Albert J. Shih

Jingjing Li

2011

ACKNOWLEDGMENTS

I would like to express my sincere thanks to my advisors, committee members, friends, colleagues, family, and many others for their guidance, help, and support. Without them, I would never have been able to finish this dissertation.

This work would not have been possible without the advice of my advisor, Professor S. Jack Hu. I am fortunate to have such a great advisor who gave me the freedom to explore on my own and at the same time the guidance to recover when my steps faltered. Professor Hu taught me how to think critically and express clearly. I would like to thank him more than I can say for his absolute advice, kindness and encouragement.

I would like to express my gratitude to my co-chair Dr. Paul Krajewski and Dr. Blair Carlson, laboratory group manager at GM, for their support and valuable discussions along my studies. I am also grateful to Drs. John Carsley, Lou Hector, Jr., Thomas Stoughton, and Aihua Luo who always showed their excellent research and great dedication in our discussions. I really appreciate their insightful vision, knowledge and support on my research. I would like to thank Theresa M. Lee, Wei Ji, Drs. Sooho Kim and Susan Hartfield-Wünsch for their technical suggestions and encouragement to overcome difficulties. I want to express my thanks to the technical staff at GM, Willie Dixon, Joshua

TABLE OF CONTENTS

LIST OF FIGURES

ix

LIST OF TABLES

ABSTRACT

CHARACTERIZATION OF POST-ANNEALING MECHANICAL BEHAVIOR OF PREFORMED ALUMINUM ALLOY 5182-O

by

Jingjing Li

Chairs: S. Jack Hu and Paul E. Krajewski

Preform annealing is a new technology for forming aluminum sheets where aluminum panels are formed by a sequence of preform stamping, annealing and final stamping. The total formability is enhanced compared to conventional one-step stamping. The post-annealing mechanical behavior is different from the as-received material; thus it is important to understand the changes in material behavior due to preforming and annealing for formability analysis, process simulation and optimization. This dissertation presents studies on the kinetic behavior of AA5182-O during static recovery and recrystallization, tensile behavior and its relationships with different pre-strain and annealing conditions, and a stress-based forming limit criterion. Microstructure and texture evolution were also investigated to help understand the mechanical property changes.

Three research topics are carried out in this dissertation:

- *Development of kinetic modeling of AA5182-O during static recovery and recrystallization*: Two empirical models for the yield stress of post-annealed

AA5182-O were developed in terms of the applied pre-strain, annealing temperature, and time for static recovery and recrystallization processes. The effects of pre-strain and annealing on post-annealing elongation, total effective elongation and strain-hardening exponent were also investigated.

- *Post-annealing mechanical properties and their relationships with pre-strain and annealing conditions*: Tensile and anisotropic behavior subjected to different pre-strain paths, levels and annealing conditions have been characterized. Statistical methods were applied to indentify the important process variables and their influences on the post-annealing properties. Microstructure and texture evolution show that the post-annealing strength is related to grain size and grain average misorientation and *R*-value is strongly dependent on texture.

- *Stress-based forming limit criterion for preform annealing:* A method to account for the preforming and annealing effects on the strain hardening behavior has been presented. With this method, the forming limit criterion in the stress space was transformed from the strain space for this two-stage forming process with annealing, where the strain information on localized necking was directly observed via the digital image correlation method. The strain-based forming limits showed the dependence on pre-straining and annealing history; however, the stress-based forming limits are independent of these processing histories, and converge to a single forming limit curve that is close to the as-received forming limit. This finding is critical to the finite element simulation of this complex forming process with local annealing. The single forming limit criterion is suitable for the different pre-strained and annealed portions of a stamped part.

CHAPTER 1

INTRODUCTION

1.1   MOTIVATION

The automobile industry is actively looking for solutions to reduce vehicle weight in order to improve fuel economy while meeting all safety requirements. Aluminum alloys are good substitutes for steels in many applications to save mass.   The advantages include recyclability, one-third the mass density of steel, and the ability to meet torsion and stiffness requirements.

One challenge for applying aluminum sheet in automotive components is its lower formability compared to conventional steels.   For example, automotive aluminum alloys, such as 5xxx and 6xxx, often tear or break if they are stamped using the same die geometry that was designed for steel sheets. Tensile elongation of aluminum alloys at room temperature is generally lower than 30% [Aluminum Autodesign Review, 1998]; while the elongation of commercial steel is approximately 40% [U. S. Steel, 2011].

In the past, several technologies were attempted to form aluminum sheets into

complex shapes, including:

1) Multiple piece assembly: The stamped pieces are welded together to make complex panel shapes. The concern of this process is the extra-cost for the sub-assembly of multiple pieces.

2) Warm forming (WF): The sheets are formed at an elevated temperature, where the die and blank holders are heated to 200-300°C [Toros, et al., 2008]. The ductility increase, especially in aluminum alloy 5xxx, is associated with an increase in strain-rate sensitivity caused by the solute drag effect [Taleff, et. al., 1998] developing more slowly, allowing additional deformation outside of the neck and increasing the limit strain [Hosford and Duncan, 1999]. The main challenges in WF include lack of a proper warm forming lubricant, die maintenance costs, and control of part dimensions in a process environment with drastic thermal gradients [Ribes, 2007].

3) Hot blow forming: The sheets are formed by hot gas-pressure, including superplastic forming (SPF) and quick-plastic forming (QPF). In SPF, the initial alloy must have an ultra-fine grain size on the order of 10µm; the material is heated, such as 450–520°C for aluminum alloy 5083; and then the panel is formed at a low strain rate of 10^{-3} to 10^{-4} s^{-1} [Mishra, et al., 1997]. QPF was developed based on the technology of SPF, in which a less expensive aluminum alloy is formed relatively quickly into an automotive panel with modified tooling for high-volume production [Krajewski and Schroth, 2007].

2

4) Fluid forming: A fluid medium is applied as a soft punch with flexible pressure on one or both sides of sheet metal to make a complex-shaped surface. Examples of fluid forming include hydroforming and viscous pressure forming (VPF). VPF can generate more uniform thickness distribution than that with hard punch forming. Some defects, such as wrinkling, fracture, local serious wall-thickness reduction and low dimensional accuracy, can be avoided [Wang, et al., 2004].

5) Electromagnetic forming (EMF): The part is formed by electromagnetic forces with a high velocity on the order of 200 m/s. The high forming rate enables the sheet to be stretched without fracturing, a phenomenon referred to "hyperplasticity" [Daehn, 2011]. In addition to enhanced formability, the process also reduces springback and wrinkling of the sheet during the forming process. This method can be applied directly to high conductivity materials, e.g., aluminum and magnesium alloys. This technology is still being developed in the lab environment for sheet metal forming.

Manufacturing complex aluminum shapes in an efficient and cost-effective process is still challenging to the auto industry. Preform annealing [Krajewski, 2007] is a promising method to form one-piece aluminum panels at a relatively high production rate. In preform annealing, as illustrated in Figure 1.1, an aluminum panel is partially formed in a stage 1 forming, annealed at an elevated temperature to eliminate the cold work partially (or entirely), and then formed to the final shape using the same die in a stage 2 forming

operation. This process is able to form aluminum panels into more complex shapes than conventional one-step forming using dies designed for steel sheets, as demonstrated in the stamping of a door inner panel for an SUV using non-age hardenable aluminum alloy 5182-O with a convection heating method [Lee, et al., 2006].
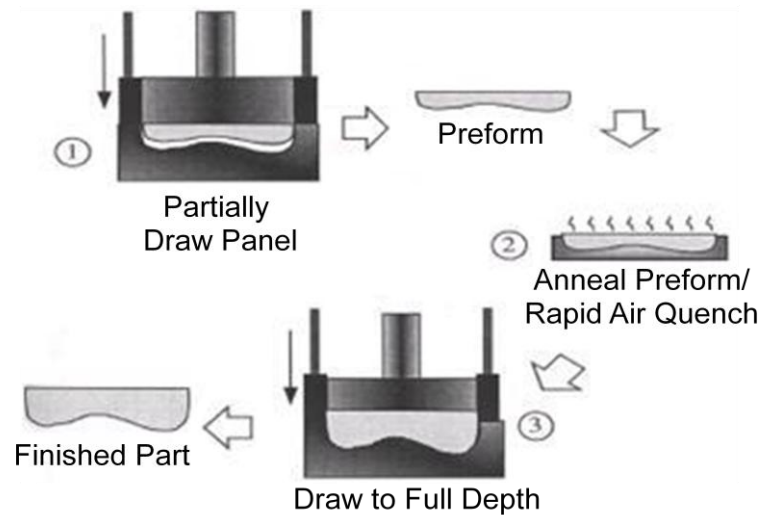
Figure 1.1 The preform annealing process [Lee, et al., 2006]

There is limited research on how preforming and annealing alter the material properties subjected to different pre-strain and annealing conditions. Preform annealing restores the ductility of single phase alloys partially (or entirely) after cold work (stage 1) through static recovery, recrystallization and grain growth. Although the metallurgical phenomena occurring during annealing have been intensively studied [Lee and McNelley, 1987; Nes, 1995; Sun and Hawbolt, 1997; Hamana et al., 1998; Verdier et al., 1998; Verdier et al., 1999; El Wahabi, et al., 2005; Kugler and Turk, 2006; Kuc et. al., 2006; Kazeminezhad, 2008; Liu et al., 2009; Roumina and Sinclair, 2010], the material behavior

4

after combined preforming and annealing has not been fully investigated. To better understand the preform annealing process, it is important to characterize the post-annealing material properties, such as tensile behavior, anisotropy, formability, etc, and to investigate the relationship between macro (e.g. mechanical) behavior and microstructure or texture evolution. In addition, these post-annealing properties are the key inputs to formability prediction using the finite element method (FEM). For this complex two-stage forming with annealing, a single forming limit criterion is needed for the FEM failure prediction since the preform and annealing history differs from point to point throughout the material.

Another issue is that preform annealing needs a cost effective heating method to reduce cycle time. One feasible solution is to employ rapid induction heating on portions of the sheet, which requires computational modeling to optimize the process design. Preform anneal has been demonstrated to be feasible using an intermediate convection heat treatment process which takes ~15 minutes [Lee, et al., 2006]. To reduce the cycle time to a period of seconds (e.g., 5 seconds or so), induction heating could be conducted on selected pre-strained regions. For this purpose, accurate FEM with optimization programming becomes important to determine the efficient annealing strategies. In addition, proper material model/properties are one of the most important elements of a computer simulation.

1.2   RESEARCH OBJECTIVES

The objective of this research is to characterize the mechanical properties of AA5182-O subjected to different preforming and annealing histories, and to develop a forming limit criterion that can be easily applied in FEM simulation for this two-stage forming with annealing process. The specific tasks are:

1) To characterize the post-annealing material properties, especially the tensile properties, such as yield stress, ultimate tensile stress, elongation and hardening behavior.

2) To develop an empirical model for the purpose of material behavior prediction, for example, a constitutive model which is primarily intended for computation of yield stress.

3) To identify the important process variables, including pre-strain path, level and annealing time, and their effects on the post-annealing mechanical properties;

4) To develop a forming limit criterion for this two-stage forming process with intermediate annealing.

This dissertation will focus the material behavior, empirical modeling and forming limit criterion development. The fulfillment of the objectives will provide a comprehensive understanding of the effects of preforming and annealing on the mechanical properties of AA5182-O and will aid the computational modeling of this complex forming process.

1.3   ORGANIZATION OF DISSERTATION

This dissertation is presented in a multiple manuscript format. Chapters 2, 3 and 4 are written as individual research papers that are partially revised for this dissertation and include abstract, main body section and references.

Chapter 2 presents the effects of pre-strain level (along uniaxial tension), annealing time and temperature on the post-annealing tensile behaviors. The standard tensile specimens were pre-strained to four levels in uniaxial tension, annealed at 300, 350, and 400 °C for holding times from 5 seconds to 1 hour and then tested in a tensile system. The effects of pre-strain level on elongation, yield stress and strain-hardening exponent were investigated and two empirical models of yield stress regarding process parameters were developed.

Chapter 3 investigates the post-annealing mechanical properties, their relationships with pre-strain and annealing, and how microstructure and texture evolution help understand the mechanical property changes. Aluminum sheet 5182-O was pre-strained in uniaxial, plane strain and equibiaxial tension to various equivalent strain levels, annealed at 350°C for short (10-second) and long (20-minute) durations, and then tested for post-annealing mechanical properties, including tensile properties and anisotropy (i.e. R_0, R_{45} and R_{90}). The importance of the process variables and their effects were identified via statistical methods, such as designed experiments and analysis of variance. The evolutions of texture and microstructure were characterized to aid the understanding of mechanical

material property changes.

Chapter 4 develops the forming limit criterion in both strain and stress spaces for this two-stage forming process with immediate annealing. AA5182-O specimens were pre-strained to two levels in uniaxial, near-plane-strain, and equibiaxial tension; specimens with three smaller shapes were extracted, annealed, and tested in limiting dome height (LDH) tests to obtain forming limits along three strain paths. Strain history was recorded with stereo digital image correlation (DIC) during each LDH test. The use of DIC provided a direct observation of localized necking at which the corresponding major/minor stresses were utilized to construct the stain and stress-based forming limits for use in stage 2. The effects from pre-strain and annealing were accounted for with the "effective plastic strain," a constant determined by overlapping the tensile flow curve of the recovery (or pre-strained) material with that of the as-received material. This constant was used as an input to transform stress history from the strain history.

Chapter 5 summarizes the investigation and proposes the future work.

REFERENCES

Aluminum Autodesign Review, (1998), The aluminum Society, 6 (3).

Daehn, G. E., Professor of Department of Materials Science and Engineering, The Ohio State University, 18 June 2011, <http://mse-gsd1.matsceng.ohio-state.edu/~glenn/hyperplasticity/Hyperplasticty%20Main%20Page.html>.

Hamana, D., Bouchear, M., Derafa, A., (1998), "Effect of plastic deformation on the formation and dissolution of transition phases in Al-12 wt.% Mg alloy," *Materials Chemistry and Physics*, 57, 99-110.

Hosford, W. F., Duncan, J. L., (1999), "Sheet metal forming: a review," *JOM Journal of the Minerals, Metals and Materials Society*, 51 (11), 39-44.

Kazeminezhad, M., (2008), "On the modeling of the static recrystallization considering the initial grain size effects," *Materials Science and Engineering A*, 486 202-207.

Krajewski, P. E., 2007, "Method for production of stamped sheet metal panels," US Patent 7,260,972, B2.

Krajewski, P. E., Schroth, J. G. , (2007), "Overview of quick plastic forming technology," *Materials Science Forum*, 551-552, 3-12.

Kuc, D., Niewielski, G., Cwajna, J., (2006), "Influence of deformation parameters and initial grain size on the microstructure of austenitic steels after hot-working processes," *Materials Characterization*, 56, 318-324.

Kugler, G., Turk, R., (2006), "Study of the influence of initial microstructure topology on the kinetics of static recrystallization using a cellular automata model," *Computational Materials Science*, 37, 284-291.

Lee, T. M., Hartfield-Wünsch, S. E., Xu, S., (2006), "Demonstration of the preform anneal process to form a one-piece aluminum door inner panel," SAE, 2006-01-0987.

Lee, W. E., McNelley, T. R., (1987), "Microstructure evolution during processing and superplastic flow in a high magnesium Al---Mg alloy," *Materials Science and Engineering* 93, 45-55.

Liu, X., Pan, Q., He, Y., Li, W., Liang, W., Yin, Z., (2009), "Flow behavior and microstructural evolution of Al–Cu–Mg–Ag alloy during hot compression deformation," *Materials Science and Engineering A*, 500, 150-154.

Mishra, R. S., Bieler, T. R., Mukherjee, A. K., (1997), "Mechanism of high strain rate superplasticity in aluminum alloy composites," *Acta Materialia*, 45 (2), 561-568.

Nes, E.,(1995), "Recovery revisited," *Acta Materialia*, 43, 2189-2207.

Ribes, H., (2007), "Warm forming of aluminum parts: a way to bridge the gap between aluminum and steel," 8 August 2011, <http://www.eaa.net/en/applications/automotive/aludrive-newsletter/_newsletter/25/_nlarticle/176/>.

Roumina,R., Sinclair, C. W., (2010), "Recovery kinetics in the presence of precipitates: The softening response of an Al–Mg–Sc alloy," *Acta Materialia*, 58, 111-121.

Sun, W. P., Hawbolt, E. B., (1997), "Comparison between static and metadynamic recrystallization – an aplication to the hot rolling of steels," *ISIJ International*, 37, 1000-1009.

Taleff, E. M., Henshall, G. A., Nieh, T. G., Lesuer, D. R., Wadsworth, F., (1998), "Warm-Temperature Ductility in Al-Mg Alloys," *Metallurgical and Materials Transactions A*, 29A, 1081-1091.

Toros, S., Ozturk, F., Kacar, I., (2009), "Review of warm forming of aluminum-magnesium alloys," *Journal of Materials Processing Technology*, 1-12.

U. S. Steel, (2011), "Commercial Steel (CS) Type B," 8 August 2011, <http://www.ussteel.com/corp/auto/tech/grades/lowcarbon/cs_type_b.asp>.

Verdier, M., Brechet, Y., Guyot, P., (1999), "Recovery of AlMg alloys: flow stress and strain-hardening properties," *Acta Materialia*, 47, 127-134.

Verdier, M., Janecek, M., Bréchet,Y., Guyot, P., (1998), "Microstructural evolution during recovery in Al–2.5%Mg alloy," *Materials Science and Engineering A*, 248, 187-197.

El Wahabi, M., Gavard, L., Montheillet, Cabrera, F., J. M., Prado, J.M., (2005), "Effect of initial grain size on dynamic recrystallization in high purity austenitic stainless steels," *Acta Materialia*, 53, 4605-4612.

Wang, Z. J., Liu, J.G, Wang, X.Y., Hu, Z.Y., Guo, B., (2004), "Viscous pressure forming (VPF): state-of-the-art and future trends," *Journal of Materials Processing Technology*, 151, 80-87.

CHAPTER 2

THE EFFECT OF PRE-STRAIN AND SUBSEQUENT ANNEALING ON THE TENSILE BEHAVIOR OF AA5182-O[1]

ABSTRACT

The effect of uniaxial tensile pre-strain and subsequent annealing on the post-annealing mechanical properties (elongation, yield stress and strain-hardening exponent) of AA5182-O was investigated. Experiments were performed at four pre-strain levels (5, 10, 15, and 20%) and three annealing temperatures (300, 350, and 400°C), with holding times ranging from 5 seconds to 1 hour. Empirical models for the yield stress of post-annealing AA5182-O were developed in terms of the applied pre-strain, annealing temperature, and time for static recovery and recrystallization processes. The strain-hardening exponent was shown to have a linear correlation with the logarithm of yield stress. The above models can be used in formability analyses and forming process optimization.

11

2.1 INTRODUCTION

Aluminum alloys are becoming increasingly desirable for automotive applications because of their high strength-to-weight ratio. However, aluminum alloys have lower formability than conventional steels, and therefore the fabrication of complex auto body shapes is more difficult. The tensile elongation of aluminum alloys at room temperature is generally lower than 30% [Aluminum Auto design Review, 1998], whereas the elongation of aluminum-killed steels is about 50% [Wagoner and Laukoni, 1983]. The ability to improve the formability of aluminum alloys through alloying and heat treatment has been limited, thus alternative forming technologies have been developed [Verma, et al., 1995; Valiev et al., 1997; Li, and Ghosh, 2003; Naka et al., 2003; Zhang et al., 2010; Toros and Ozturk, 2010]. Preform annealing [Krajewski, 2007] is a new technology developed to address this formability challenge by introducing an annealing step to soften the strained areas between preforming and forming operations. In this process, an aluminum panel is first formed to an initial shape through conventional stamping (stage-1 forming), annealed at an elevated temperature to eliminate the cold work or strain hardening through recovery and recrystallization. It is then formed to the desired shape with a second stamping operation (stage-2 forming) [Li, et al., 2010]. At this point, the panel can be trimmed and flanged if necessary. This process enables aluminum sheets to be formed into more complex shapes than conventional one-step forming, as demonstrated in the stamping of an automotive door inner panel using aluminum alloy 5182-O [Lee et al., 2006].

Accurate forming simulation of this process is critical to its use on production parts. The simulation of this technology using finite element method (FEM) requires a comprehensive understanding of the effect of pre-strain and annealing on the post annealing material behavior, such as elongation, yield stress, strain-hardening exponent, and yield strength coefficient. The assumption currently used in the engineering simulations, e.g., ABAQUS and LS-DYNA, is that the material properties are fully recovered after annealing (yield stress returns to as-received level). However, this approach is not consistent with our preliminary experimental findings, limiting the accuracy of the FEM predictions.

There is limited published knowledge on the behavior of AA5182-O, during pre-straining and subsequent annealing. Especially important is the lack of a post-annealing material model that can be used in the process simulation. During annealing, two fundamental metallurgical processes that can affect the post-annealing material properties are static recovery and recrystallization. For these two processes, much work has been devoted to determining the kinetic behaviors and mechanical properties [Nes, 1995; Sun and Hawbolt, 1997; Liu et al., 2009; Roumina and Sinclair, 2010], as well as grain growth and microstructure evolution [Lee and McNelley, 1987; Hamana et al., 1998; Verdier et al., 1998]. In modeling development, the factors, such as initial grain size [El Wahabi, et al., 2005; Kugler and Turk, 2006; Kuc et. al., 2006; Kazeminezhad, 2008], annealing temperature and time [Verdier et al., 1999], and strain rate or temperature during

hot forming [Sun and Hawbolt, 1997; Verdier et al., 1999; Kuc et. al., 2006, Abedrabbo et al., 2006] were well studied. However, there is no clear relationship between pre-strain and annealing process variables as well as the subsequent mechanical properties (flow stress, strain hardening, formability, etc) for aluminum alloy AA5182-O.

The goal of the present paper is to experimentally investigate the effect of pre-straining and annealing on the post-annealing mechanical properties of AA5182-O; and to develop an empirical model relating the process variables to the post-annealing yield stress and strain-hardening exponent that can be used in post anneal process simulation. Experimental observations are based on uniaxial tensile tests. The identified mechanical properties will be interpreted using kinetics models for static recovery and recrystallization, such as the Cottrell and Aytekin equation [1950] and the Johnson-Mehl-Avrami-Kolmogorov (JMAK) model [Johnson and Mehl, 1939; Avrami, 1939; Kolmorgorov, 1937. The parameters in the empirical model will be determined using a best fit of the experimental data.

The remainder of this paper is organized as follows: Section 2 describes the incoming material properties and experiment procedures; the observations are shown in Section 3; Section 4 discusses the results with derived empirical models; and Section 5 is summarizes and concludes the paper.

2.2   MATERIALS AND EXPERIMENTS

Commercial, 1.1 mm aluminum alloy AA5182-O sheet was used to investigate the effects of pre-strain and annealing on the post-annealing mechanical behavior.   An optical micrograph of as-received AA5182-O is shown in Figure 2.1, and the chemical compositions are listed in Table 2.1.

The experimental procedure is as follows: 1) sample sheets of AA5182-O were pre-strained in uniaxial tension at four different levels of uniaxial strain (5, 10, 15, and 20%); 2) they were then annealed in a salt bath at three different temperatures (300, 350 and 400°C) for various exposure times (from 5 seconds to 1 hour) followed by air cooling; 3) the samples were subjected to standard uniaxial tensile tests [ASTM E8, 2008]. The post-annealing mechanical properties of AA5182-O are characterized in terms of the pre-strain levels, annealing temperatures and exposure times.   There are 88 test conditions in total and 3 duplicates at each condition.
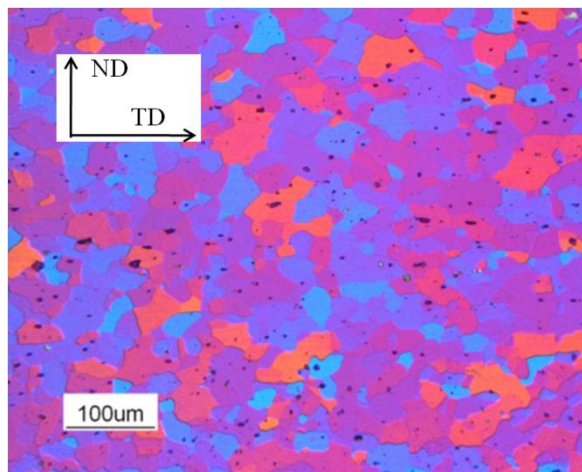
Figure 2.1 Microstructure of AA5182-O sheet in the as-received condition: ND is the normal direction through the thickness and TD is the transverse direction

Table 2.1 Chemical composition of AA5182-O (wt %)

Al	Mg	Mn	Fe	Si	Cu	Ni	Ti	Zn
Bal	4.3	0.34	0.21	0.03	<0.01	<0.01	<0.01	<0.01

A. Uniaxial pre-straining

The sheet samples were sheared into 12.5mm wide standard tensile bars at 90º to the rolling direction (the transverse direction) [ASTM E8, 2008]. Uniaxial tensile pre-straining was conducted at a constant strain rate of 10^{-3} s^{-1} on an Instron 5582 universal testing machine. Pre-strains were introduced as levels of 5, 10, 15, and 20% in engineering strain measured by a 50-mm extensometer.

B. Annealing

All samples were subjected to isothermal heat-treatments using a salt bath heater equipped with an auto tune temperature controller. The annealing temperatures were 300, 350, and 400°C with holding or dwell times ranging from 5 seconds to 1 hour. The temperatures of the salt bath were monitored by a K-type thermocouple with variation of ±5°C.

C. Post-annealing mechanical properties

Post-annealing elongation, yield stress and the strain-hardening exponent were measured using standard uniaxial tensile tests, which were performed at room temperature in the transverse direction using the same strain rate as applied in the pre-strain process.

The post-annealing elongation is the maximum engineering strain of a sample at failure in the post-annealing tensile test. The *total effective elongation* is the summation of pre-strain and post-annealing elongations:

$$Total\ effective\ elongation=Pre\text{-}strain+Post\text{-}annealing\ elongation \qquad (2.1)$$

Yield stress was determined from the engineering stress-strain curve according to the standard 0.2% offset method. Strain-hardening exponent (*n*) was derived by fitting true stress-strain curve using Hollomon's equation in a power law:

$$\sigma = K\varepsilon_p^n \qquad (2.2)$$

where σ is the true stress, K is the strength coefficient, and is the true plastic strain[Marciniak et al., 2002].

2.3   RESULTS

2.3.1 Mechanical Properties of As-received AA5182-O

Table 2.2 lists the mechanical properties of AA5182-O. The stress-strain curve of as-received material is shown in Figure 2.2, which also shows the flow curves for pre-strained samples at four different pre-strain levels (5, 10, 15, and 20%). After pre-straining in uniaxial tension, the samples were held at room temperature for 30 days, and reloaded in uniaxial tension for mechanical testing. Portevin-Le Chatelier (PLC) serrations are found for both as-received and pre-strained AA5182-O. A distinct static

strain aging effect is observed, where pre-strained materials show higher stress than the as-received one. The occurrence of this phenomenon associates with the occurrence of PLC (a type of dynamic strain aging behavior [Dieter, 1986].

Table 2.2 Typical room-temperature tensile properties of AA5182-O as-received

Yield stress (MPa)	Ultimate tensile stress (MPa)	Uniform elongation (%)	Total elongation (%)	K (MPa)	n-value
128	282	23.4	25.4	582	0.33
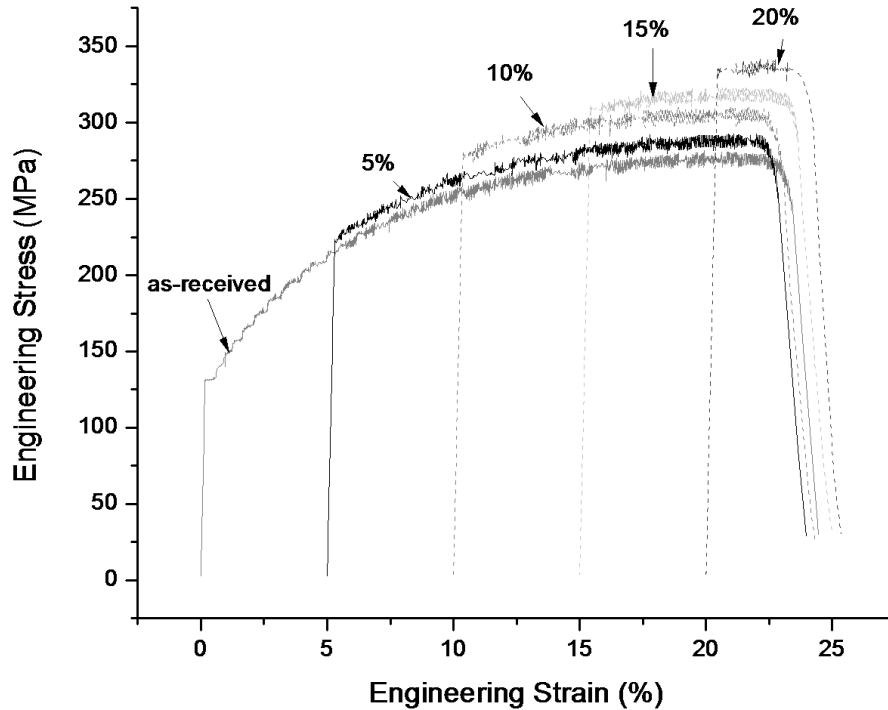
Figure 2.2 Stress-strain curves of as-received and pre-strained AA5182-O

2.3.2 Post-annealing Material Properties

Figure 2.3 (a-c) shows the post-annealing elongation at three different annealing temperatures. Each of the four lines corresponds to the four different pre-strain levels.
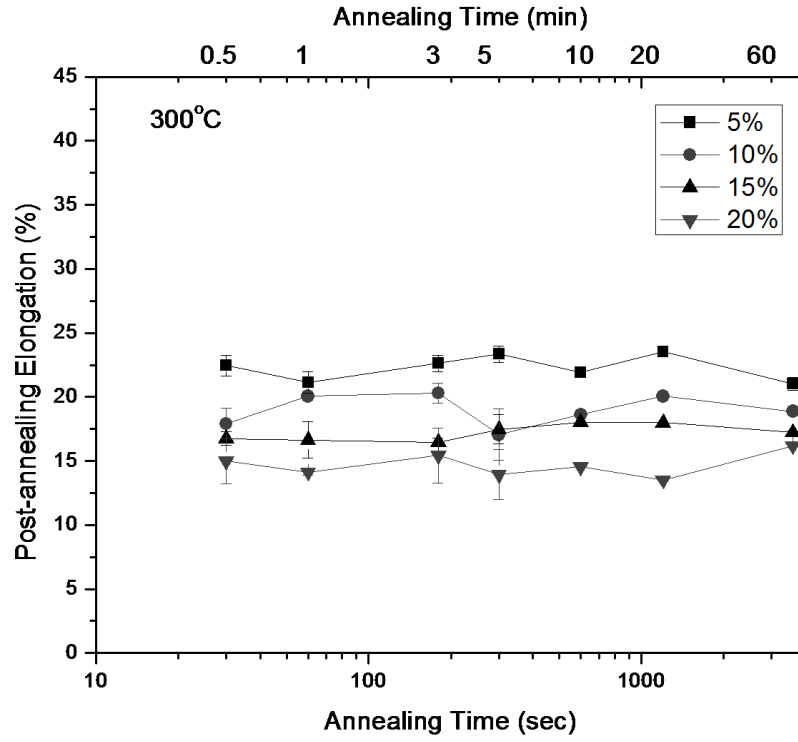
(a)
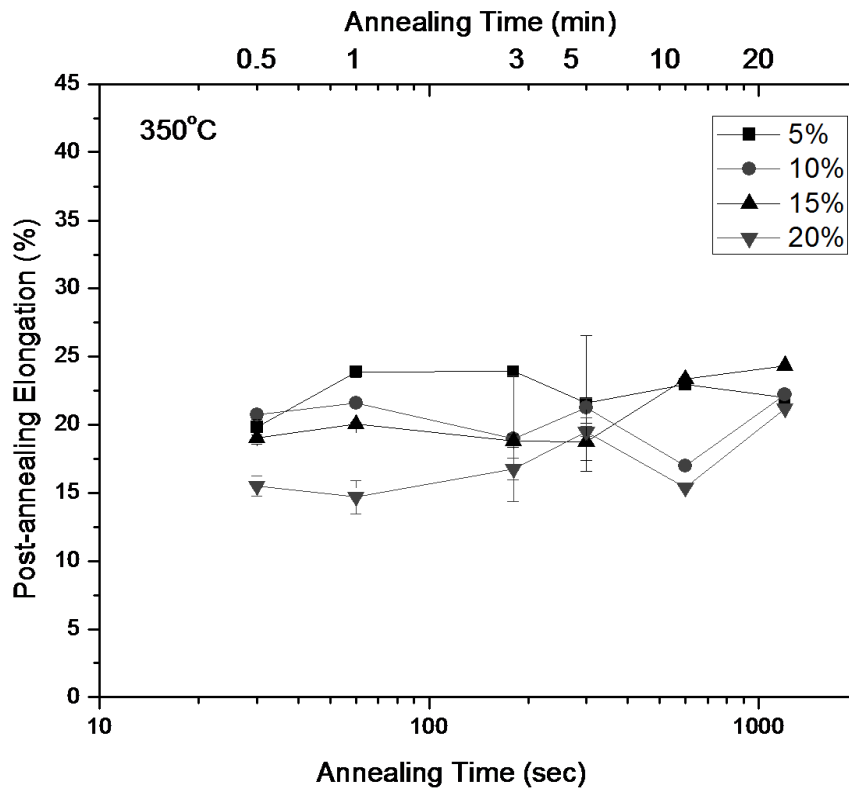
(b)
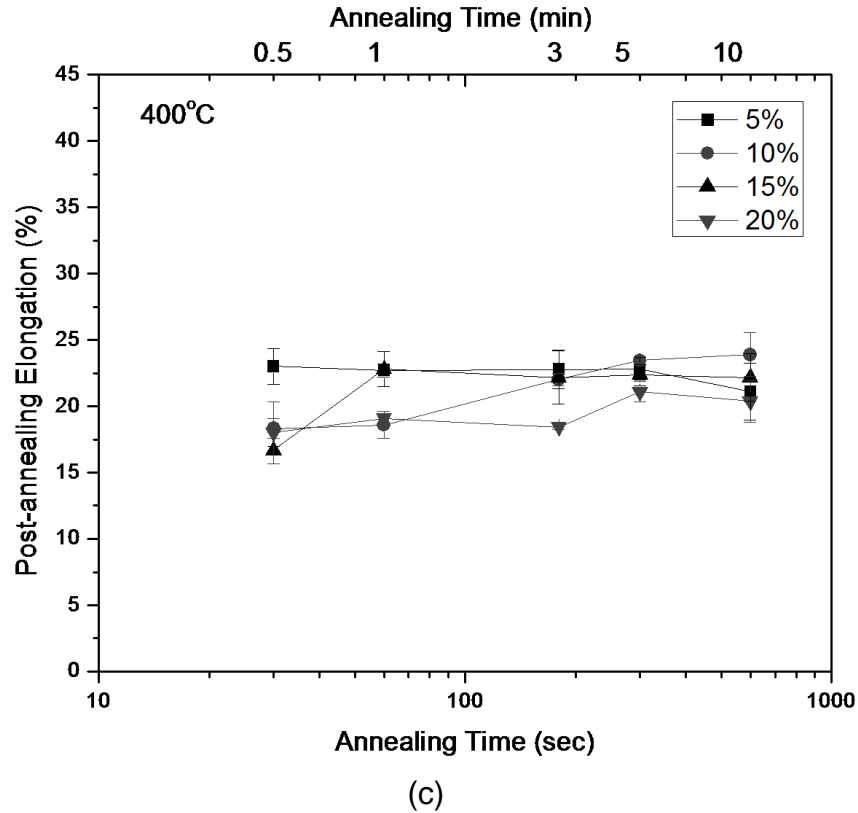
Figure 2.3 Experiments at annealing temperatures of (a) 300°C, (b) 350°C, and (c) 400°C, show independence of post-annealing elongation on annealing time

20% pre-strain leads to lower post-annealing elongations for these three temperatures. At 300°C, the curves are roughly parallel, where pre-straining is an important factor for the post-annealing elongation and with increased pre-straining the elongation decreases. Overall, the post-annealing elongations are within 14-24%.

The comparison of total effective elongation is shown in Figure 2.4 (a-d), where (a) and (c) are plotted as a function of exposure times, and (b) and (d) as a function of pre-strain levels. The total effective elongation is highly dependent on pre-strain: more pre-strain leads to a higher effective elongation. The time effect is less significant when

(a)

(b)

21
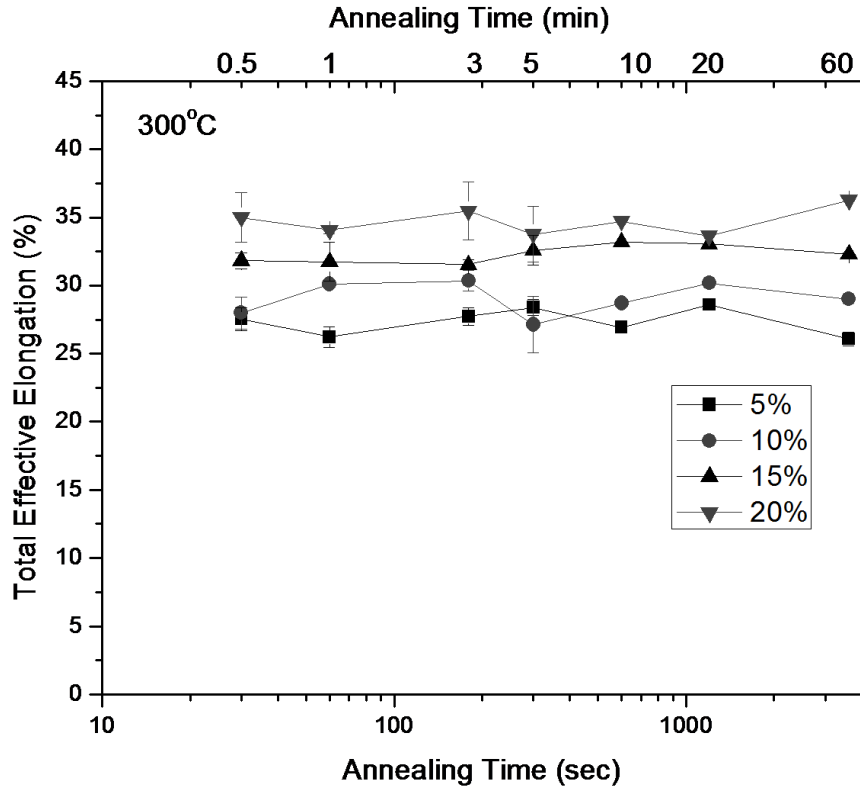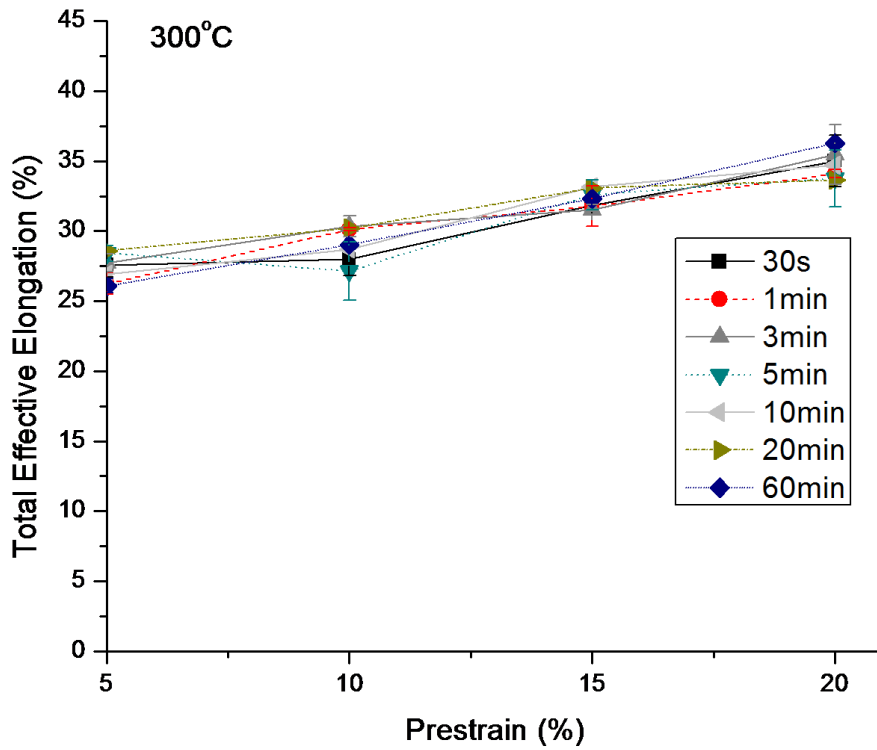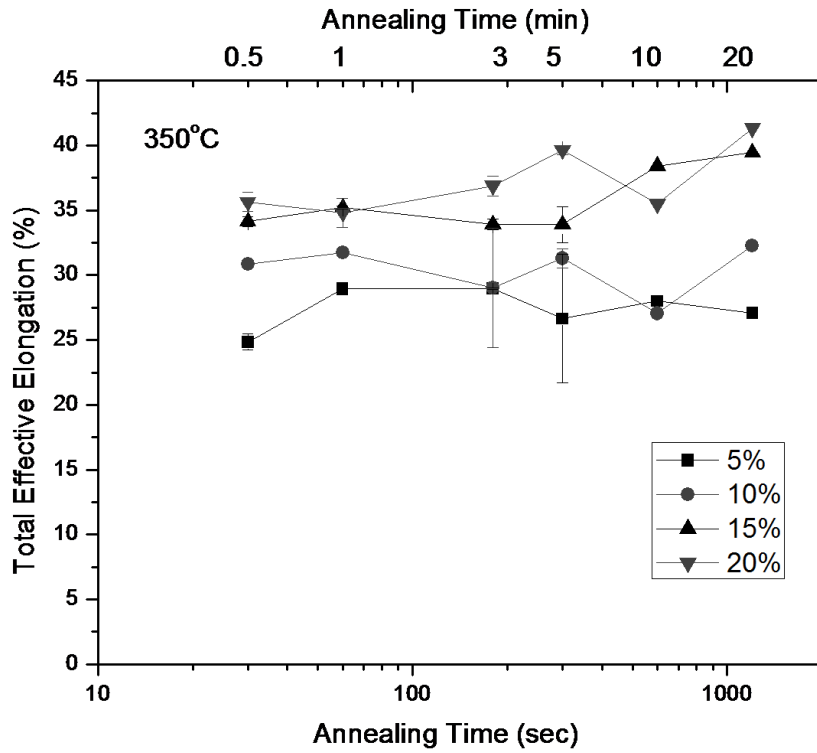
(c)
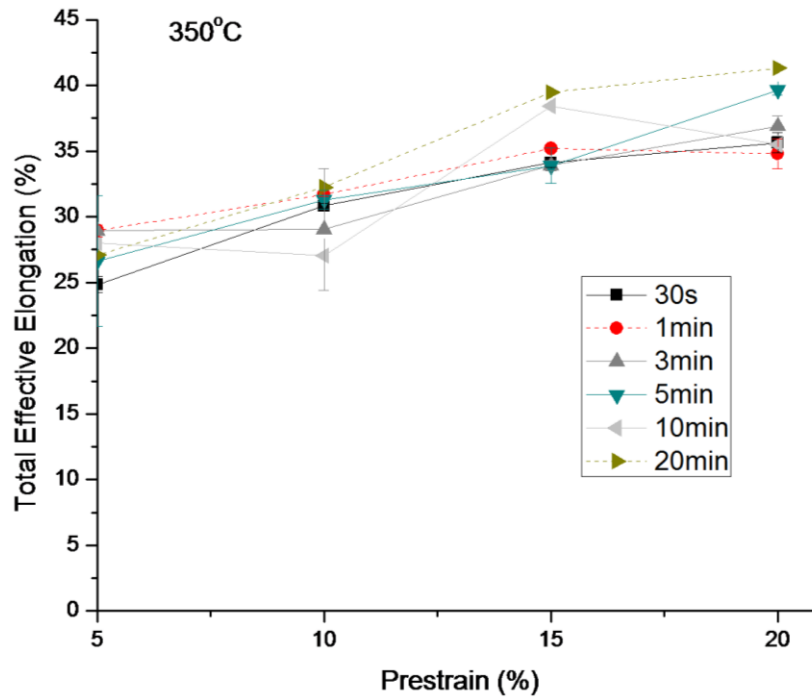
(d)

Figure 2.4 Total effective elongation increases with pre-strain: (a) annealed at 300°C, vs. annealing time; (b) annealed at 300°C, vs. pre-strain; (c) annealed at 350°C, vs. annealing; (d) annealed at 350°C, vs. pre-strain

annealing temperature is 300°C, as is demonstrated by the flat curves. At 20% pre-strain, the total effective elongation for aluminum can reach as much as 35%~40% for the heating temperatures of both 300 and 350°C, respectively.

The evolutions of yield stress for three temperatures are shown in Figure 2.5 (a-c). At all temperatures (i.e. 300, 350, and 400°C), post annealing yield stress drops quickly for samples pre-strained to $\geq 10\%$, and approaches a constant value ~105MPa after a long exposure time. This value is lower than the yield stress of incoming material. Optical metallography (Figure 2.6) confirms that these changes correspond to a change in the grain structure of the material, likely due to recrystallization and grain growth. The final plateau in the curve indicates that the material was fully recrystallized, which agrees with others [Sarkar et al., 2006]. The drop in yield stress occurs at shorter times for higher pre-strain levels or annealing temperature.

(a)

23
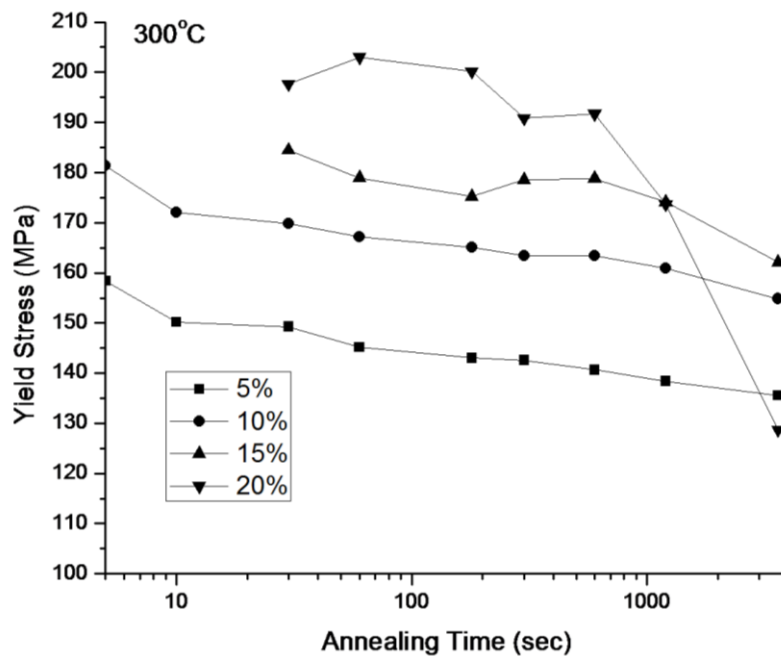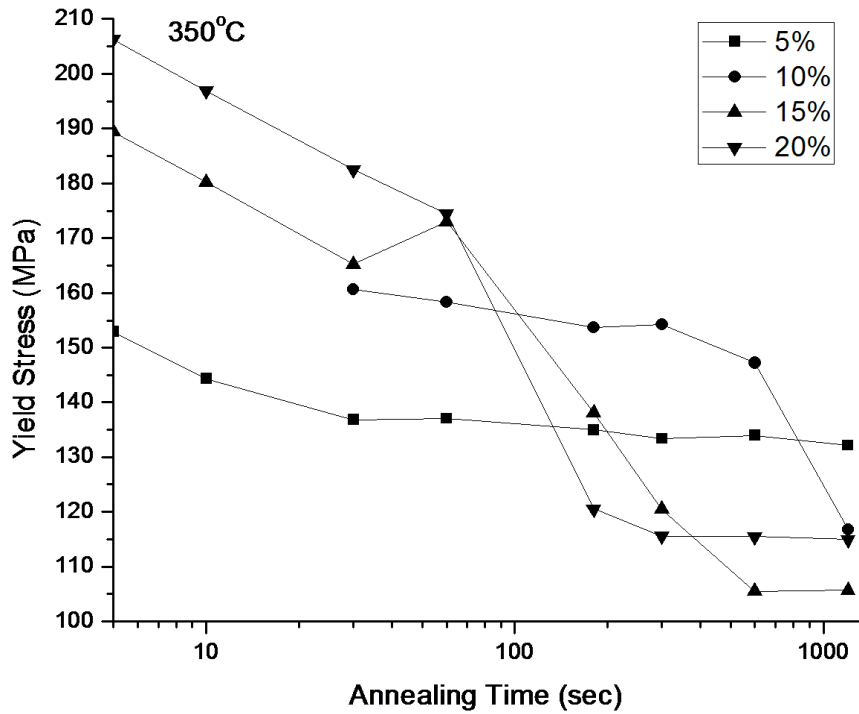
(b)
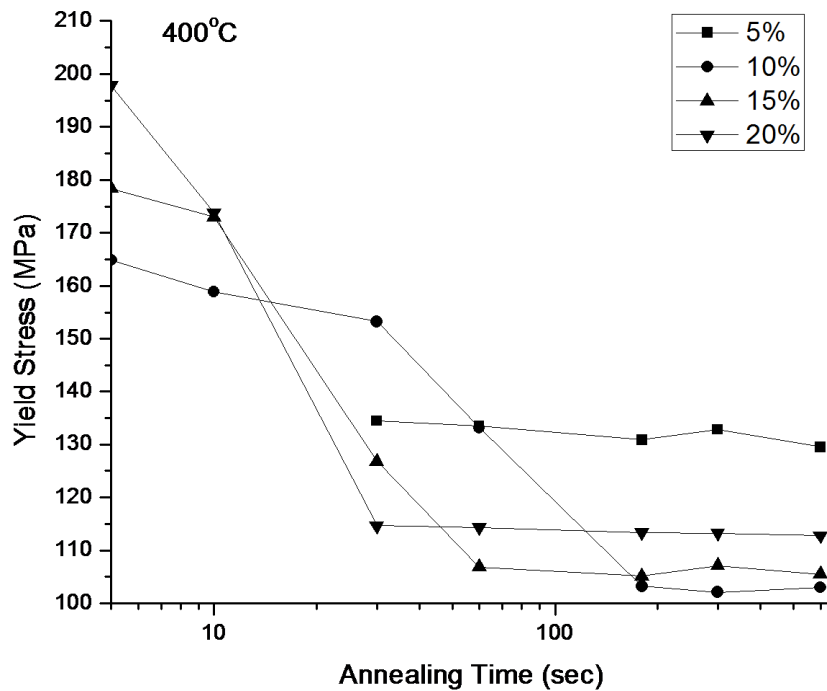
(c)

Figure 2.5 The effects of pre-stain and annealing time on post-annealing yield stress in AA5182-O, at temperatures of: (a) 300°C, (b) 350°C, and (c) 400°C
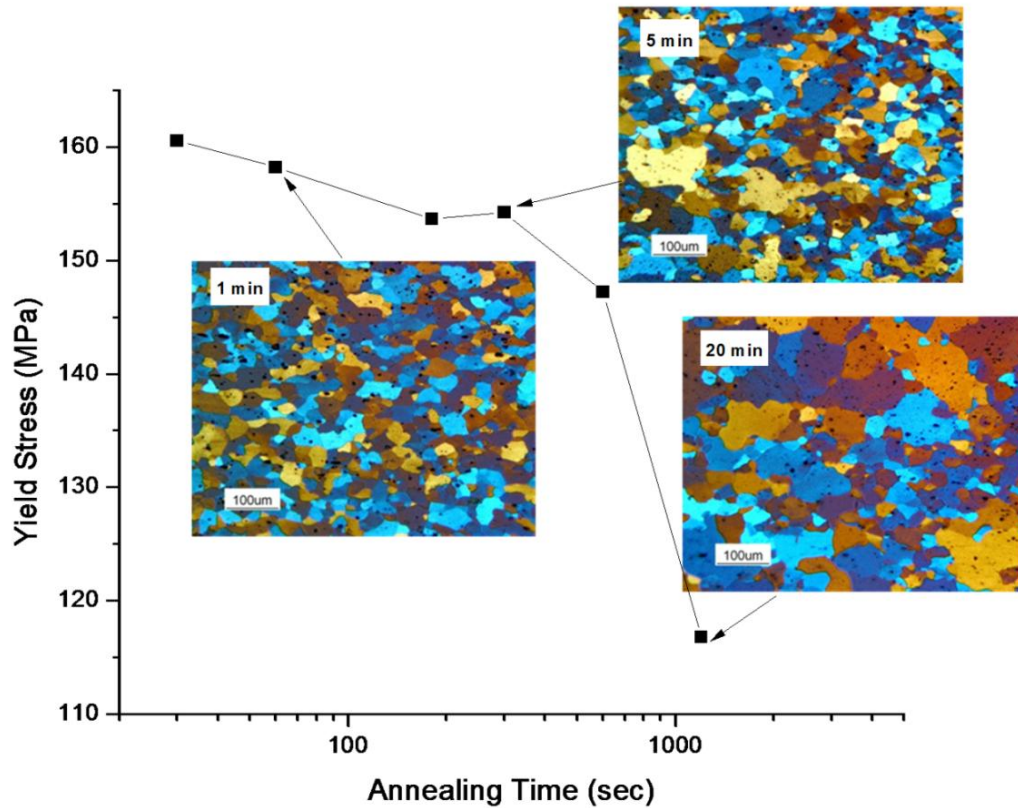
Figure 2.6 The effects of pre-strain and annealing time at 350°C on
post-annealing yield stress and grain structure in AA5182-O

Strain-hardening exponents (*n*) were plotted as a function of annealing time for
different temperatures and pre-strains, as shown as Figure 2.7 (a-c). The increasing
n-values versus $\log t$ produced an "S"-shaped curve for post-annealing aluminum. The
strain hardening exponent increased after annealing because dislocations can move more
easily [Zhang et al., 1989]. At the final plateau, *n*-values reach to 0.33 at 350°C and 0.34
at 400°C, respectively, which are comparable with the initial value 0.33 (Table 2.2). From
Figures 2.5 and 2.7, an opposite correlation between *n*-value and yield stress curves can be
seen. Strength coefficients (*K*) of post-annealing AA5182-O are shown in Figure 2.8.
Most *K* values of post-annealing materials are close to the incoming value 582 MPa
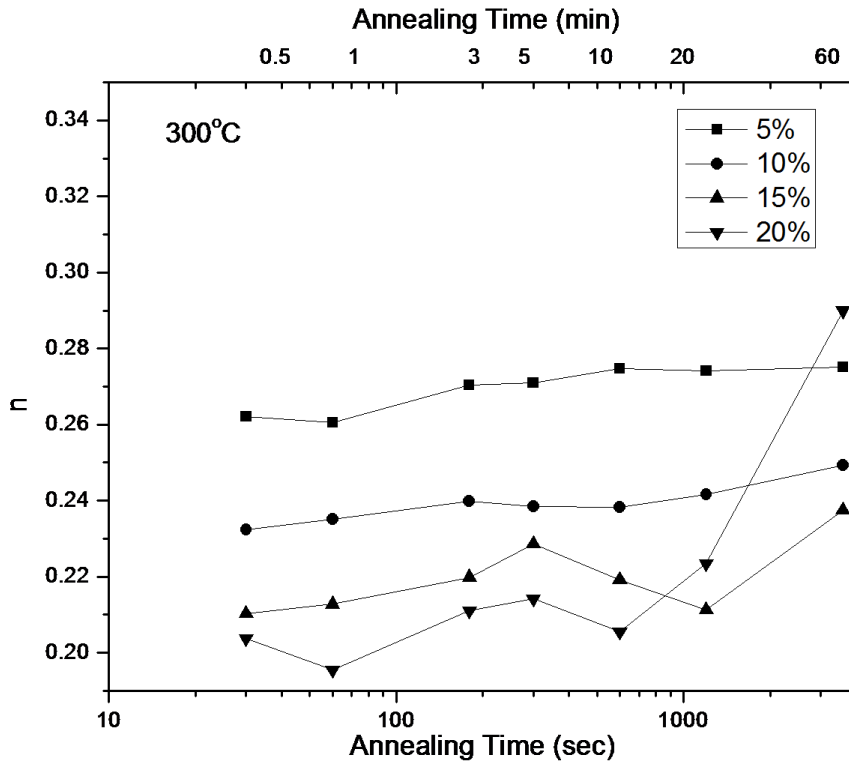
(a)
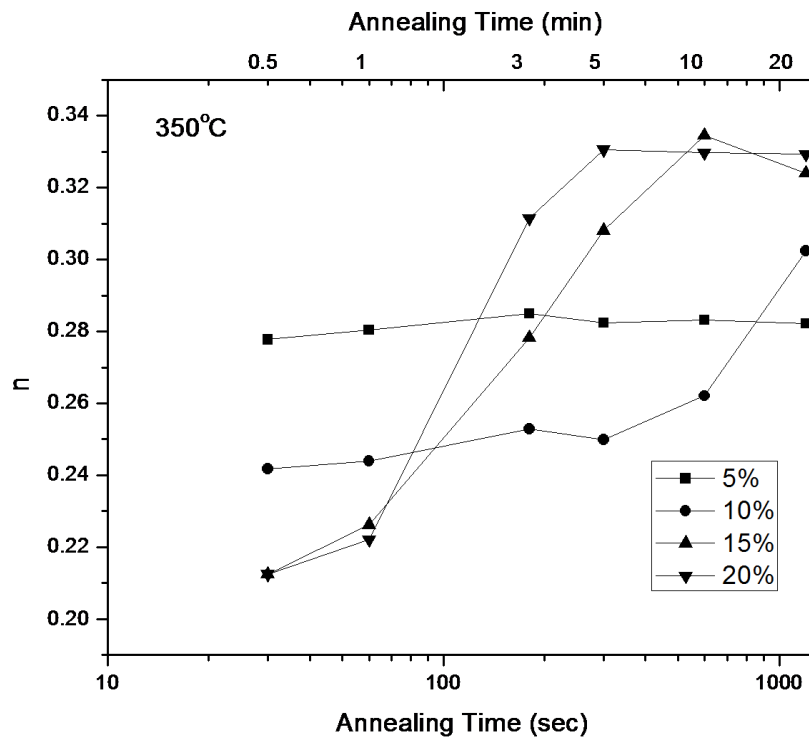
(b)
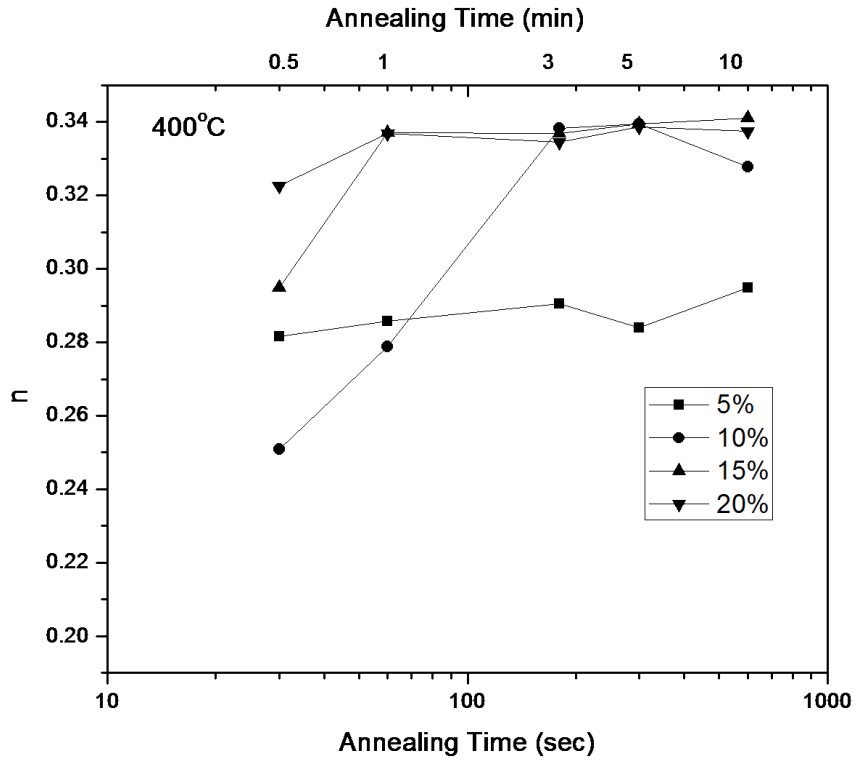
(c)

Figure 2.7 The effects of pre-stain and annealing time on strain hardening exponent (n) in AA5182-O, at annealing temperatures of: (a) 300°C (b) 350°C, and (c) 400°C
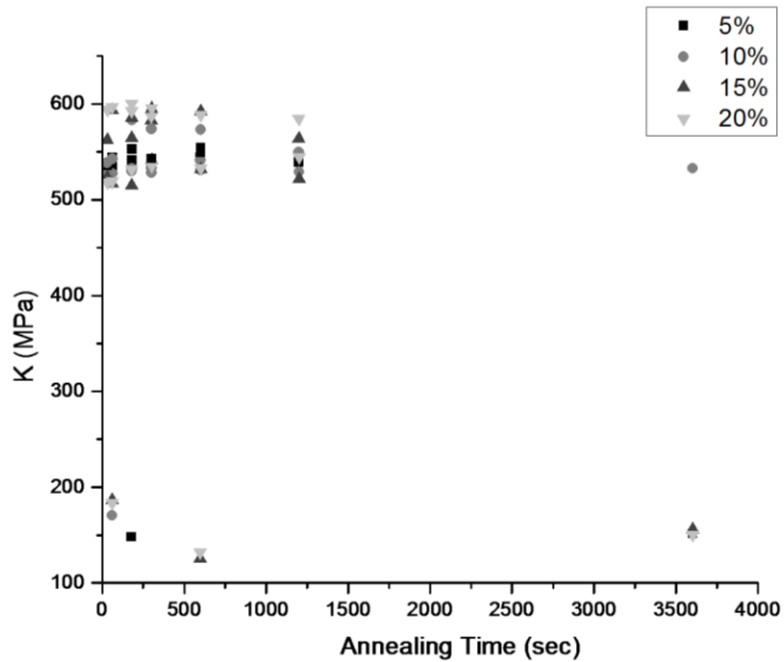
Figure 2.8 The effects of pre-stain and annealing time at three temperatures on *K* value in AA5182-O

(Table2.2), and 9 observations (among 52 in total) fall in the range of 100-200 MPa.

Since *K* value is more consistent with original value, it is less dependent on cold work,

annealing temperature, and time in comparisons to the *n*-value and yield stress.

2.4   MODEL DEVELOPMENT

In this section, kinetic models are developed to describe the post-annealing yield

stress and its dependence on annealing temperatures, times, and pre-strains for static

recovery and recrystallization. A linear relationship of log yield stress and strain-hardening

exponent (*n*) will be proposed.

2.4.1 Kinetic Model of Yield Stresses for Static Recovery

Recovery is controlled by two mechanisms [Humphreys and Hatherly, 2004]:

dislocation climb and thermally activated glide of dislocations. A good fitting using

thermal activation mechanism (Eq. 2.3) for the recovery behavior of AA5182-O shows that

it is thermally activated dislocation glide or cross-slip. If the activation energy (*Q*) is a

function of the yield stress (σ_{ys}), then the rate of recovery is calculated as [Cottrell, 1953].

$$\frac{d\sigma_{ys}}{dt} = -c_1 \exp(-\frac{Q(\sigma_{ys})}{RT}) \qquad (2.3)$$

where c_1 is an unknown constant, *R* is gas constant ($8.314 \dfrac{J}{Kmol}$), and *T* is temperature.

The activation energy is expected to decrease with increased dislocation density or cold

work [Humphreys and Hatherly, 2004], and can be written as a function of yield stress

$$Q(\sigma_{ys}) = Q_0 - c_2 \sigma_{ys} \qquad (2.4)$$

Equation (3) becomes

$$\frac{d\sigma_{ys}}{dt} = -c_1 \exp(-\frac{Q_o - c_2 \sigma_{ys}}{RT}) \qquad (2.5)$$

By integration of Eq. (2.3), Cottrell and Aytekin [1950] gave

$$\sigma_{ys} = \sigma_i - \frac{RT}{c_2} \ln(1 + \frac{t}{t_0}) \qquad (2.6)$$

where c_1 and c_2 are constants, and σ_i is the flow stress at $t = 0$ (i.e., the start moment of the annealing process). σ_i can be calculated by multiplying the maximum flow stress after pre-strain with a ratio, in a Power law relation

$$\sigma_i = aK\varepsilon^n \qquad (2.7)$$

where a is a constant that $0 < a < 1$, ε is the pre-strain, K is the strength coefficient, and n is strain-hardening exponent shown in Table 2.2. t_0 is defined by

$$t_0 = \frac{RT}{c_1 c_2} \exp(\frac{Q_0 - c_2 \sigma_i}{RT}) \qquad (2.8)$$

Thus, the yield stress can be interpreted in terms of pre-strain ε, annealing temperature T, and exposure time t in the following expression

$$\sigma_{ys} = aK\varepsilon^n - \frac{RT}{c_2} \ln\left[1 + \frac{t}{\dfrac{RT}{c_1 c_2} \exp(\dfrac{Q_0 - c_2 aK\varepsilon^n}{RT})}\right] \qquad (2.9)$$

2.4.2 Kinetic Model of Yield Stresses for Static Recrystallization

The most common method for modeling recrystallization kinetics is the JMAK model, which has the following form:

$$X_v = 1 - \exp(-Bt^p) \tag{2.10}$$

where is X_v is the fraction of recrystallized material, B is a function of the nucleation rate and growth rate, and p is the JMAK or Avrami exponent.

Denote $t_{0.5}$ as the time for 50% recrystallization. JMAK equation can be rearranged as

$$X_v = 1 - \exp\left[\ln(0.5) \times (\frac{t}{t_{0.5}})^p\right] = 1 - \exp\left[-0.693(\frac{t}{t_{0.5}})^p\right] \tag{2.11}$$

$t_{0.5}$ has the following expression [35]

$$t_{0.5} = b_1 \varepsilon^{b_2} \exp(\frac{Q_r}{RT}) \tag{2.12}$$

where b_1 and b_2 are constants, $\bar{\varepsilon}$ is the applied strain (the pre-strain in this work), and Q_r is the activation energy for recrystallization.

The fraction of recrystallization can be determined from the softening data by using a softening fraction (S) [Sun and Hawbolt, 1997].

$$X_v = \frac{S - C}{1 - C} \tag{2.13}$$

where C is a constant representing the critical softening fraction where recrystallization starts. Thus the recovery effects can be eliminated from the recrystallization model [14].

Softening fraction (S) is a function to assess the normalized changes in yield stress

that took place during annealing (Figure 2.9), and defined using the following equation [36]

$$S = \frac{\sigma_i - \sigma_{ys}}{\sigma_i - \sigma_0} \qquad (2.14)$$

where σ_i is the flow stress at the beginning of the annealing, the same definition in Eq. (2.6); σ_0 is the yield stress of completed softening material; and σ_{ys} is the yield stress of post-annealing material. The softening fraction includes the hardening and softening contributions from all physical process involved in the pre-strain and annealing.
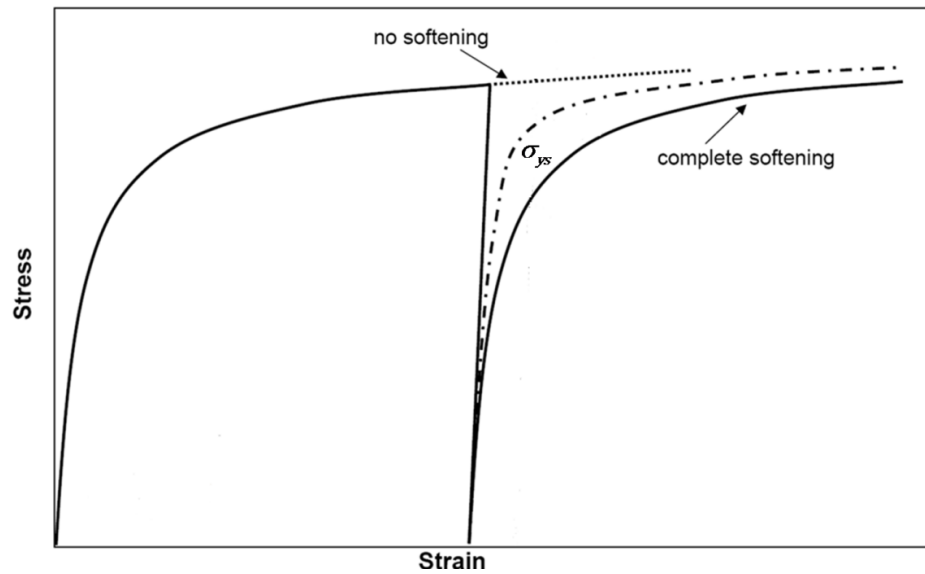
Figure 2.9 Estimation of softening fraction using yield stress, the figure is from Ref. [Zurob et al., 2004]

By combining Eqs. (2.7, 2.11-2.14), the post-annealing yield stress (σ_y) can be expressed in terms of pre-strain ε, annealing temperature T, and exposure time t by the following equation

$$\sigma_{ys} = (aK\varepsilon^{n} + \sigma_0)(1-C)\exp\left\{-0.693 \times \left[\frac{t}{b_1\varepsilon^{b_2}\exp(\frac{Q_r}{RT})}\right]^{p}\right\} + \sigma_0 \qquad (2.15)$$

2.4.3 Classification of Static Recovery and Recrystallization Process using Kinetic Models

Recovery and recrystallization processes are difficult to separate since recovery progresses gradually with time and there is no readily identifiable ending of the process [Verdier et al., 1999]. A statistical approach is proposed to discriminate the recovery and recrystallization processes by fitting the kinetics models using regression method.

From previous analyses, the rate of recovery is a log function of time (t), which can be simplified as

$$\sigma_{ys} = A - B \times \log(1 + t/D) \qquad (2.16)$$

The rate of recrystallization is an exponential function of time (t). From literature [Go, 2001], the exponent p in Eq. 2.15) can be approximated as 1, and then the rate of recrystallization has the following simple formula

$$\sigma_{ys} = E \times \exp(-t/F) + G \qquad (2.17)$$

where A, B, D, E, F, and G are fitting constants.

Using regression analysis, the fitting constants and *Adjusted R^2* are shown in Table 2.3. *Adjusted R^2* is a measure of how well future outcomes are likely to be predicted by the fitted model and a larger value suggests a better prediction capability [Minitab, 2009].

Table 2.3 Discrimination of static recovery and recrystallization processes using Eq. (2.16-17)

	$\sigma_{ys} = A - B \times \log(1 + t/D)$				$\sigma_{ys} = E \times \exp(-t/F) + G$			
	A	B	D	Adj. R^2	E	F	G	Adj. R^2
300°C, 5%	157.8	3.242	1.444	0.977	11.45	541	136.3	0.872
300°C, 10%	189.1	1.846	0.0004	0.987	13.89	1375	154.1	0.881
350°C, 5%	152.8	3.451	0.6392	0.954	5.139	234.6	132.6	0.833
350°C, 10%	162.6	508.3	13750	0.913				0.912
350°C, 15%	197.9	22.20	13.21	0.852	80.2	216.3	102.9	0.937
350°C, 20%	389.1	20.45	0.0009	0.696	104.2	87.93	113.3	0.954
400°C, 5%	136.4	1.59	12.12	0.468	7.08	587.5	127.2	0.427
400°C, 10%	332.7	17.91	0.0009	0.739	89.09	55.81	101.7	0.993
400°C, 15%	183.3	5.686	0.0004	0.101	456.96	9.72	105.9	0.987

Note: the light gray color represents recovery process, and the dark gray color is for recrystallization process.

For the conditions at 300°C with 5-10% pre-strain and 350°C with 5% pre-strain, the *Adjusted R^2* is above 0.95 for logarithmic fitting (a fitting for recovery process), whereas is only 0.85 for exponential fitting (the one for recrystallization process), therefore the above processes were dominated by recovery. The *Adjusted R^2* for annealing at 350°C with 15-20% pre-strain and 400°C with 10-15% pre-strain are high for exponential fittings with values around 0.95, and low for logarithmic fittings. Thus, recrystallization was more likely to happen for these conditions. There are unusual observations with very low *Adjusted R^2* or uncommon coefficients, such as 350°C with 10% pre-strain and 400°C with 5% pre-strain, which cannot be classified as either recovery or recrystallization, these may be explained by a combination of both. Overall, the *Adjusted R^2* can be used to discriminate whether the process is recovery or crystallization through a mathematical regression analysis.

2.4.4 Empirical Kinetics Model of Yield Stresses

Kinetic models of recovery and recrystallization are applied to evaluate yield stresses in terms of pre-strain, annealing temperature, and annealing times, according to Cottrell-Aytekin recovery and JMAK recrystallization models.   For recovery process, the empirical model is

$$
\sigma_{ys} = aK\varepsilon^n - \frac{RT}{c_2}\ln\left[1 + \frac{t}{\frac{RT}{c_1 c_2}\exp(\frac{Q_0 - c_2 aK\varepsilon^n}{RT})}\right]
$$

$$
= 407\varepsilon^{0.33} - \frac{RT}{1482}\ln\left[1 + \frac{t}{\frac{RT}{1482\times 2.88\times 10^4}\exp(\frac{275,000 - 1482(407\varepsilon^{0.33})}{RT})}\right]
$$

(2.18)

where the activation energy for dislocation glide is 275 kJ/mol.   This value for Q is similar to values published elsewhere for other Al-Mg alloys (273 kJ/mol for AA5754 [Go, 2001].

The kinetic model for recrystallization is

$$
\sigma_{ys} = (aK\varepsilon^n + \sigma_0)(1-C)\exp\left\{-0.693\times\left[\frac{t}{b_1\varepsilon^{b_2}\exp(\frac{Q_r}{RT})}\right]^p\right\} + \sigma_0
$$

$$
= 0.25(407\varepsilon^{0.33} + 105)\exp\left[-0.693\frac{t}{3\times 10^{-17}\varepsilon^{-4}\exp(\frac{186,690}{RT})}\right] + 105
$$

(2.19)

As before, the value for the activation energy of 186.69 kJ/mol is similar to other published work on Al-Mg alloys [Koizumi et al., 2000; Go, 2001].   The initial yield stress is the value after pre-straining and at the start moment of annealing ($t = 0$), which shows

dependence on the pre-strain and empirically expressed as

$$\sigma_{ys}(t=0)=(aK\varepsilon^{n}+\sigma_{0})(1+C)+\sigma_{0} \qquad (2.\ 20)$$

For the fully recrystallized materials ($t=\infty$), the yield stresses become a constant, i.e., σ_{0}.

The yield stress evolutions are characterized using the Cottrell-Aytekin recovery and the JMAK recrystallization models. Figures 2.10 and 2.11 show good agreements between the experimental data and fit to the equation. The softening effect of recovery was removed by introducing a softening fraction value, i.e., the constant C in Eq. (2.15), when modeling the recrystallization process. This value can be calculated for the
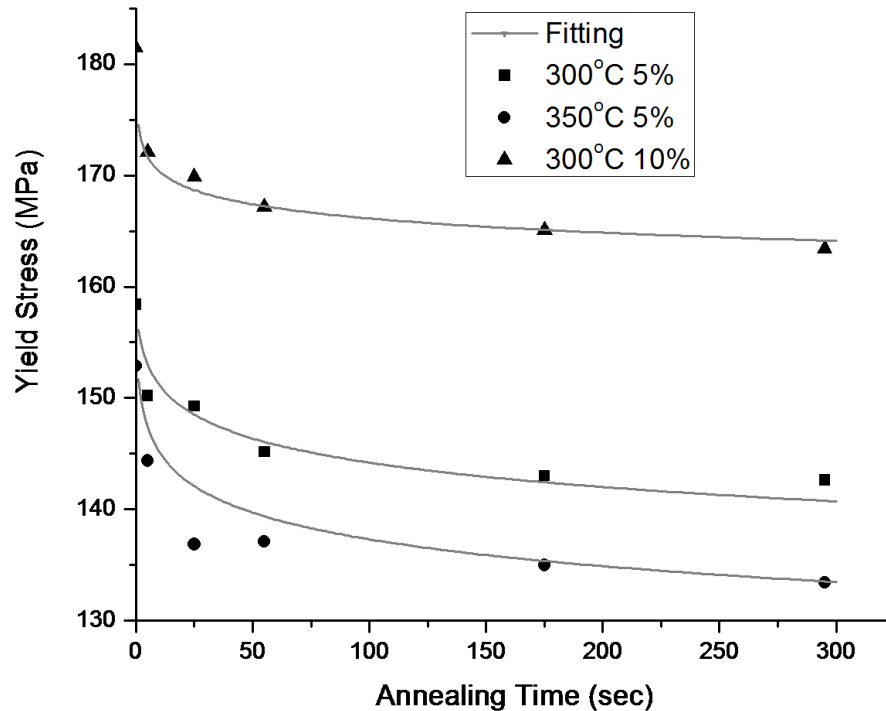
Figure 2.10 Comparison between experimental data and fitting results using Cottrell-Aytekin recovery model

softening fraction evolution curves [Sun and Hawbolt, 1997; Yanagida and Yanagimoto, 2008] or derived from regression analysis.
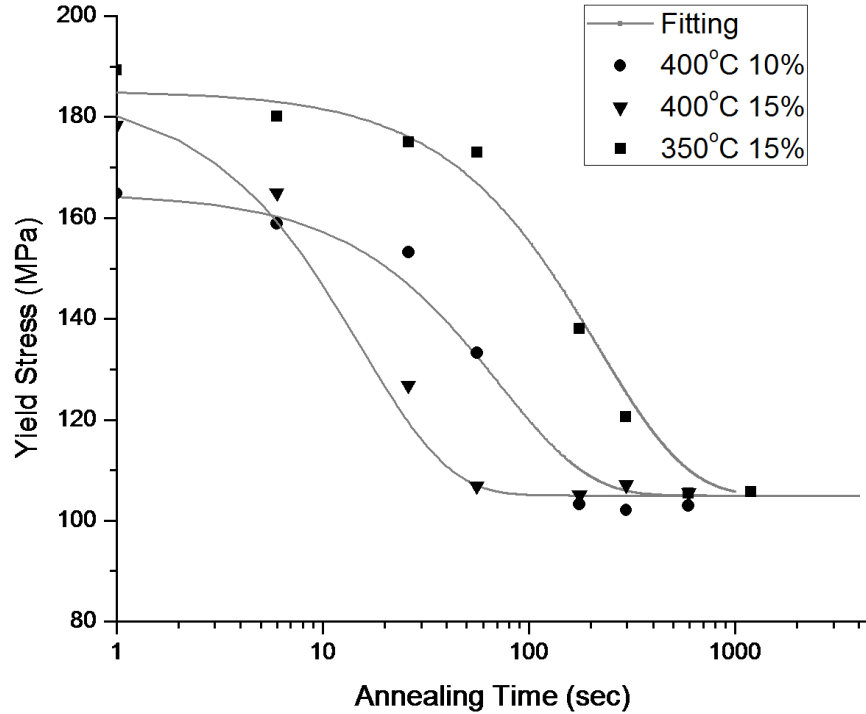
Figure 2.11 Comparison between experimental data and fitting results using JMAK recrystallization model

2.4.5 Relationship between Yield Stress and Strain-hardening Exponent

Section 2.3.2 shows an opposite correlation between yield stress and strain-hardening exponent. The regression model of n and $\ln \sigma_{ys}$ is shown in Figure 2.12, which exhibits an excellent linear relationship with a high *Adj. R^2* value of 0.97. The linear regression model is

$$n = -0.22669 \times \ln \sigma_{ys} + 1.3946 \tag{2. 21}$$

By using Hollomon's equation, the linear relationship can be shown as follows:

36

$$\sigma = K\varepsilon_p^n$$

$$\Rightarrow \ln \sigma = \ln K + n \ln \varepsilon_p \tag{2.22}$$

$$\Rightarrow n = \frac{1}{\ln \varepsilon_p}(\ln \sigma - \ln K) = \frac{1}{\ln \varepsilon_p} \ln \sigma - \frac{\ln k}{\ln \varepsilon_p}$$

where K is the strength coefficient of post-annealing AA5182-O, and is close to the incoming value, as seen as Figure 2.8. Based on the definition of 0.2% yield stress and using engineering values to approximate a small true stress and strain values, Eq. (2.22) becomes

$$n = \frac{1}{\ln \varepsilon_{ys}} \ln \sigma_{ys} - \frac{\ln K}{\ln \varepsilon_{ys}} \tag{2.23}$$

where ε_{ys} is the strain at σ_{ys}; and by comparing $ln\,K$, i.e., ln582 and $\left|\dfrac{\text{intercept}}{\text{slope}}\right|$, the
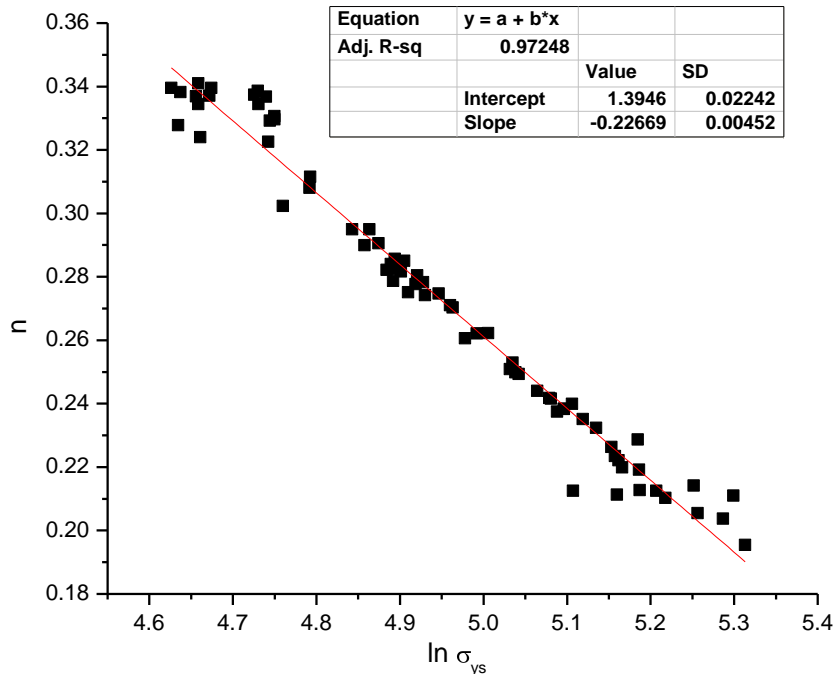
Figure 2.12 Linear relationship between strain-hardening exponent (*n*) and log yield stress ($\ln \sigma_{ys}$)

difference is calculated by

$$\text{difference} = \left| \frac{\ln K - \left| \frac{\text{intercept}}{\text{slope}} \right|}{\ln K} \right| \qquad (2.24)$$

That is 3.37%, where the intercept and slope values are the constants in Eq. (2.21).

Strain-hardening exponent (*n*) has a linear correlation with yield stress. The linear relationship was seen by other researchers [Bowen and Partidge, 1974; Samuel, 2006]. Thus, *n*-values can be estimated by yield stress and using the yield stress empirical models, Eqs. (18)- (19), it can be written in a function of pre-strain, annealing temperature and time.

2.5   CONCLUSIONS

The post-annealing mechanical behaviors of AA5182-O were studied using uniaxial tensile tests, where pre-strain, annealing temperature and time were the key variables investigated. The post-annealing tensile properties of AA5182-O vary with the process conditions (pre-strain, annealing time, and annealing temperature) and they cannot be exactly reset to incoming values. These actual post anneal properties will be incorporated into the finite element simulation of the preform anneal process for formability assessment and improvement.

Specific conclusions are:

1) For post-annealing elongation and total effective elongation, pre-strain is a more important factor than annealing time. Total effective elongation increases with pre-strain. A 20% pre-strain can yield about 40% total effective elongation of aluminum.

2) Post-annealing yield stress depends on pre-strain and annealing conditions. Two empirical kinetic models of yield stress were developed in terms of pre-strain, annealing temperature and exposure time for static recovery and recrystallization. Since the yield stress can also be correlated to metallographic observations, the developed yield stress model helps to estimate the microstructure from the process conditions.

3) At a given strain rate, the strain-hardening exponent (n) showed a linear relationship with log yield stress. Combined with 3), the strain-hardening exponent of post-annealing materials can be represented as a function of pre-strain, annealing temperature and annealing time for static recovery and recrystallization processes.

4) The strength coefficient (K) of post-annealing AA5182-O did not significantly change after pre-strain and annealing. It was also independent of the yield stress.

It is possible to control the yield stress or strain-hardening exponent to different values while ensuring the same post-annealing elongation through different combinations of pre-strain and annealing.

REFERENCES

Abedrabbo, N., Pourboghrat, F., Carsley, J., (2006), "Forming of aluminum alloys at elevated temperatures – Part 1: Material characterization," *International Journal of Plasticity*, 22, 314-341.

Aluminum Auto design Review, (1998), The Aluminum Society, 6 (3).

ASTM E8/E 8M-08, (2008), "Standard test methods for tension testing of metallic materials," ASTM International, West Conshohocken, PA.

Avrami, M., (1939), "Kinetics of phase change. I general theory," *Journal of Chemical Physics*, 7, 1103-1112.

Bowen, A. W., Partidge, P. G., (1974), "Limitations of the Hollomon strain-hardening equation," *Journal of Physics D: Applied Physics*, 7, 969-978.

Cottrell, A. H., Aytekin, V., (1950), "The flow of zinc under constant stress," *Journal Institute of Metals*, 77, 389-422.

Cottrell, A. H., (1953), "Dislocations and plastic flow in crystals," Clarendon Press, Oxford.

Dieter, G. E., (1986), "Mechanical Metallurgy," third ed., McGraw-Hill, New York.

Go, J., (2001), "Recovery and recrystalization behavior of AA5754 and IF-Boron Steel during Annealing," MASc thesis, UBC Retrospective Theses Digitization Project.

Hamana, D., Bouchear, M., Derafa, A., (1998), "Effect of plastic deformation on the formation and dissolution of transition phases in Al-12 wt.% Mg alloy," *Materials Chemistry and Physics*, 57, 99-110.

Humphreys, F. J., Hatherly, M., (2004), "Recrystallization and related annealing phenomena," second ed., Elsevier Ltd., Oxford.

Johnson, W. A., Mehl, R. F., (1939), "Reaction kinetics in processes of nucleation and growth," *Transaction Metallurgical Society AIME*, 135, 416-442.

Kazeminezhad, M., (2008), "On the modeling of the static recrystallization considering the initial grain size effects," *Materials Science and Engineering A*, 486 202-207.

Koizumi, M., Kohara, S., Inagaki, H., (2000), "Kinetics of recrystallization in Al-Mg alloys," *Zeitschrift fuer Metallkunde/Materials Research and Advanced Techniques*, 91

460-467.

Kolmorgorov, A. N., (1937), "Zur statistik der k   nge in metallen," *Izvestiya Rossiiskoi Akademii Nauk. Seriya Matematicheskaya*, 355-359.

Krajewski, P. E., (2007), "Method for production of stamped sheet metal panels," US Patent 7,260,972, B2.

Kuc, D., Niewielski, G., Cwajna, J., (2006), "Influence of deformation parameters and initial grain size on the microstructure of austenitic steels after hot-working processes," *Materials Characterization*, 56, 318-324.

Kugler, G., Turk, R., (2006), "Study of the influence of initial microstructure topology on the kinetics of static recrystallization using a cellular automata model," *Computational Materials Science*, 37, 284-291.

Lee, T. M., Hartfield-Wünsch, S. E., Xu, S., (2006), "Demonstration of the preform anneal process to form a one-piece aluminum door inner panel," *SAE*, 2006-01-0987.

Lee, W. E., McNelley, T. R., (1987), "Microstructure evolution during processing and superplastic flow in a high magnesium Al---Mg alloy," *Materials Science and Engineering* 93, 45-55.

Li, D. Li, Ghosh,A. K., (2003), "Tensile deformation behavior of aluminum alloys at warm forming temperature," *Materials Science and Engineering A*, 352, 279-286.

Li, J. J., Zhou,Y., Hu, S. J., Izquierdo, L. E., Krajewski, Lee, P. E., Lee, T. M., (2010), "Optimization of localized annealing for preform anneal forming of aluminum alloys," *Transactions of NAMRI*, 38, 411-418.

Liu, X., Pan, Q., He, Y., Li, W., Liang, W., Yin, Z., (2009), "Flow behavior and microstructural evolution of Al–Cu–Mg–Ag alloy during hot compression deformation," *Materials Science and Engineering A*, 500, 150-154.

Marciniak, Z., Duncan, J. L., J. L., Hu, S. J., (2002), "Mechanics of Sheet Metal Forming," second ed., Butterworth-Heinemann, Oxford.

Minitab, version 15, (2009), Minitab Inc. http://www.minitab.com/

Naka, T., Nakayama, Y., Uemori, T., Hino,R., Yoshida, F., (2003), "Effects of temperature on yield locus for 5083 aluminum alloy sheet," *Journal of Materials Processing Technology*, 140, 494-499.

Nes, E.,(1995), "Recovery revisited," *Acta Materialia*, 43, 2189-2207.

Roumina,R., Sinclair, C. W., (2010), "Recovery kinetics in the presence of precipitates: The softening response of an Al–Mg–Sc alloy," *Acta Materialia*, 58, 111-121.

Samuel, K. G., (2006), "Limitation of Hollomon and Ludwigson stress-strain relations in assessing the strain hardening parameters," *Journal of Physics D: Applied Physics*, 39, 203-212.

Sarkar, S., Wells, M. A., Poole, W. J., (2006), "Softening behaviour of cold rolled continuous cast and ingot cast aluminum alloy AA5754," *Materials Science and Engineering A*, 421, 276-285.

Sun, W. P., Hawbolt, E. B., (1997), "Comparison between static and metadynamic recrystallization – an aplication to the hot rolling of steels," *ISIJ International*, 37, 1000-1009.

Toros, S., Ozturk, F., (2010), "Modeling uniaxial, temperature and strain rate dependent behavior of Al–Mg alloys," *Computational Materials Science*, 49, 333-339.

Valiev, R. Z., Salimonenko, D. A., Tsenev, N. K., Berbon, P. B., Langdon, T. G., (1997), "Observations of high strain rate superplasticity in commercial aluminum alloys with ultrafine grain sizes," *Scripta Materialia*, 37, 1945-1950.

Verdier, M., Brechet, Y., Guyot, P., (1999), "Recovery of AlMg alloys: flow stress and strain-hardening properties," *Acta Materialia*, 47, 127-134.

Verdier, M., Janecek, M., Bréchet,Y., Guyot, P., (1998), "Microstructural evolution during recovery in Al–2.5%Mg alloy," *Materials Science and Engineering A*, 248, 187-197.

Verma, R., Ghosh, A. K., Kim, S., Kim, C., (1995), "Grain refinement and superplasticity in 5083 Al," *Materials Science and Engineering A*, 191, 143-150.

Wagoner, R. H., Laukonis, J. V., (1983), "Plastic behavior of aluminum-killed steel following plane-strain deformation," *Metallurgical Transactions A*, 14, 1487-1495.

El Wahabi, M., Gavard, L., Montheillet, Cabrera, F., J. M., Prado, J.M., (2005), "Effect of initial grain size on dynamic recrystallization in high purity austenitic stainless steels," *Acta Materialia*, 53, 4605-4612.

Yanagida, A., Yanagimoto, J., "Formularization of softening fractions and related kinetics for static recrystallization using inverse analysis of double compression test," *Materials Science and Engineering A*, 487 (2008) 510-517.

Zhang, C., Leotoing, L., Guines, D., Ragneau, E., (2010), "Experimental and numerical study on effect of forming rate on AA5086 sheet formability," *Materials Science and*

Engineering A, 527, 967-972.

Zhang, F., Huang, M., Shi, D., (1989), "The relationship between the strain-hardening exponent *n* and the microstructure of metals," *Materials Science and Engineering A*, 122, 211-213.

Zurob, H. S., Hutchinson, C. R., Brechet, Y., Purdy, G. R., (2004), "Formularization of softening fractions and related kinetics for static recrystallization using inverse analysis of double compression test," *Materials Science and Engineering A*, 382, 64-81.

CHAPTER 3

POST-ANNEAL MECHANICAL PROPERTIES OF PRE-STRAINED

AA5182-O SHEETS[2]

ABSTRACT

The effects of different pre-strain levels, paths and subsequent annealing on the post-annealing mechanical properties of AA5182-O were investigated. Aluminum sheet specimens were pre-strained in uniaxial, plane strain and equibiaxial tension to several equivalent strain levels, annealed at 350°C for short (10 seconds) and long (20 minutes) durations, and then tested for post-annealing mechanical properties, including tensile properties and anisotropy. The tensile properties and *R*-values exhibited dependencies of pre-strain and annealing history. The importance of the process variables and their effects were identified via designed experiments and analysis of variance. Texture in the as-received and deformed sheets was investigated with electron backscattered diffraction and provided a means for linking pre-strain and static recovery or recrystallization with

---

microstructure. This guided the understanding of the mechanical property changes observed after preforming and annealing.

3.1   INTRODUCTION

Aluminum alloys are considered to be good substitute materials for steels in automotive applications where vehicle weight reduction and improved fuel efficiency are required. The formability of aluminums is lower than conventional steels: this has limited the application of aluminum alloys in formed parts with complex shapes. For example, the tensile elongation of aluminum alloys at room temperature is generally lower than 30% [Aluminum Auto design Review, 1998]; while the elongation of aluminum-killed steels is approximately 45% [Jun and Hosford, 1986]. Consequently, the application of 5xxx and 6xxx series aluminum alloys to the fabrication of automotive body and closure panels may require specialized forming techniques [Fridlyander et al., 2002]. One technique holding great promise is preform annealing [Krajewski, 2007], which is a two-step process including an annealing heat treatment between initial and final forming operations. Specifically, an aluminum panel is partially formed to an initial shape through conventional stamping resulting in a "preform." The preform is then annealed to eliminate or reduce the effects of cold work, and formed to the final shape or "final form" with a second stamping operation. The final panel can then be flanged and otherwise processed in a conventional line die as necessary. Lee et al. [2006] showed how preform

annealing can be used to produce an automotive liftgate inner panel with AA5182-O by requiring only minor design modifications to the original steel product geometry.

Annealing "resets" the material properties through static recovery and/or recrystallization of the cold worked material. However, the post-annealing properties are not always reset to the original properties [Li et al., 2011]. It is thus necessary to understand how the pre-strain path, amount of pre-strain and annealing affect the post-annealing mechanical characteristics, such as yield strength and forming limits, in order to fully utilize such a process for product design and manufacturing.

There is limited published knowledge on how pre-strain and annealing affect the mechanical behavior of AA5182-O, a candidate aluminum alloy for automotive applications. Most previous work focused on the effect of changing pre-strain path or annealing condition on flow stress, strain hardening behavior, and forming limits. One of the earlier studies found that different pre-strain paths affected the increase of flow stress [Achni et al., 2009]. Under linear or non-linear loading, strain hardening was reduced anisotropically and controlled by different mechanisms, such as the Bauschinger effect, dislocation structure, and texture evolution [Barlat et al., 2008]. Narayanasamy et al. [2009] showed that annealing AA5052 can increase R-values, strain-hardening exponent (n), and raise the forming limit curve vertically indicating increased formability. Nevertheless, there is a paucity of information on the combined effects from these two processes and the relative importance of pre-strain and heat treatment variables.

The objective of this paper is to assess the post-annealing mechanical behavior of AA5182-O subjected to different pre-strain paths, levels and annealing times at 350°C. Pre-strain paths were introduced by nearly linear deformation consisting of uniaxial, plane strain, and equibiaxial tension. Depending on the annealing durations, static recovery and recrystallization took place during annealing [Li et al., 2011] and caused changes in material properties and the extent to which these changes are beneficial for forming was investigated. The post-annealing mechanical properties were estimated using standard tensile testing and *R*-value testing. Microstructure and texture evolution were characterized by electron backscattered diffraction (EBSD) to understand the changes in post-annealing material behavior.

The remainder of paper is organized as follows: Section 2 presents the incoming material properties and experimental procedures for pre-straining, annealing and post-annealing tests; Section 3 describes the results on post-annealing ultimate tensile strength (*UTS*), yield stress (*YS*), strains, and *R*-values; and Section 4 concludes the paper with a summary.

3.2   MATERIALS AND EXPERIMENTAL PROCEDURE

Commercial grade AA5182-O aluminum alloy of 1.1 mm thickness was used to investigate the effects of pre-strain and annealing on post-annealing properties. The experimental procedure included three steps: pre-straining, annealing, and testing.

3.2.1 Materials

The chemical composition of the AA5182-O alloy was 4.3% Mg, 0.34% Mn, 0.21% Fe and 0.03% Si, with the balance of Al. The texture and grain size distribution of the as-received AA5182-O specimen are presented in Figure 3.1, where the inverse pole figure (IPF) map, (001) pole figure (PF) and grain size distribution are summarized in Figures 3.1a to 3.1c, respectively. The as-received specimens are fully recrystallized as their grain average misorientation (GAM) value is 0.3 and the average grain size is nominally 30 µm

(a)

(b)   (c)
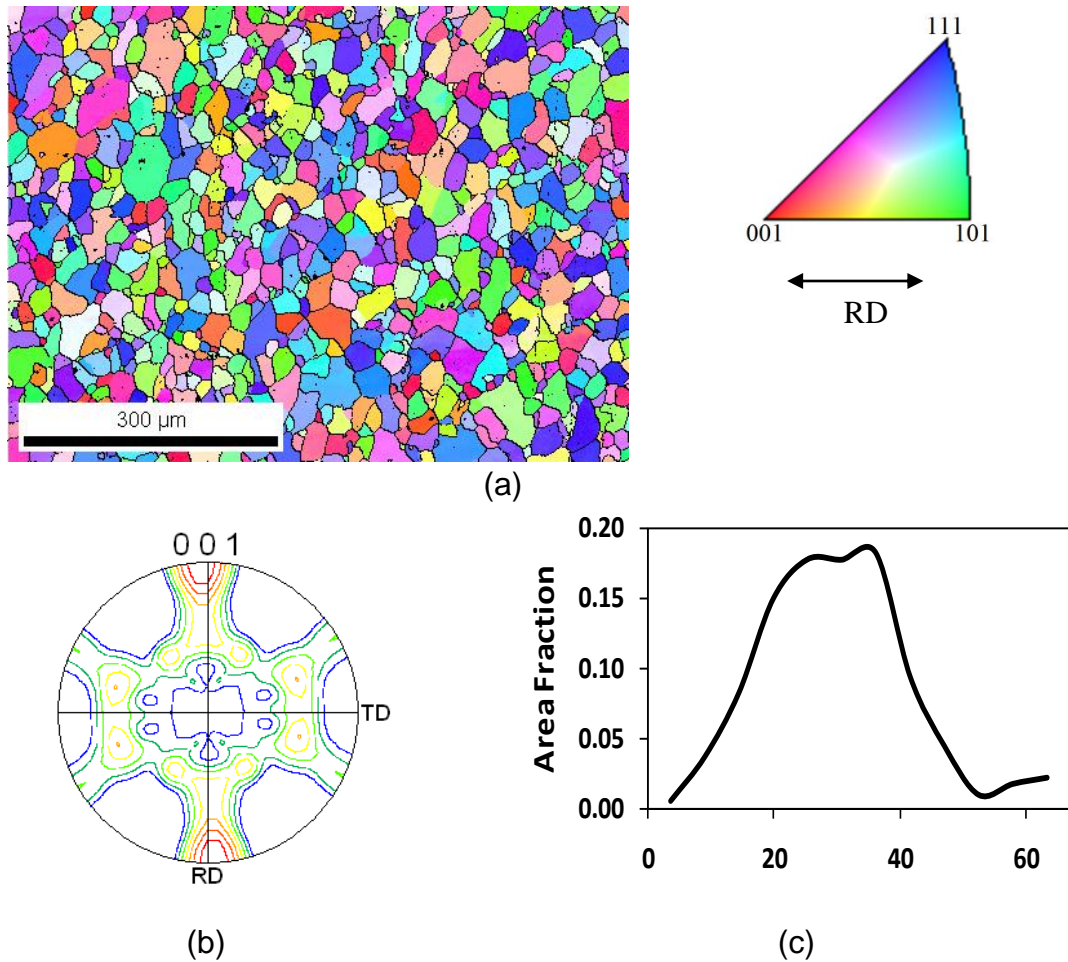
Figure 3.1 Inverse pole figure, pole figure map and grain size distribution of AA5182-O as-received: (a) IPF, (b) PF, and (c) grain size distribution

(Figure 3.1c). Table 3.1 summarizes the mechanical properties tested along transverse direction (TD), which were provided by the supplier.

Table 3.1 Typical room-temperature mechanical properties of AA5182-O as-received

Yield stress (MPa)	Ultimate tensile stress (MPa)	Uniform elongation (%)	Total elongation (%)	K (MPa)
128	282	23.4	25.4	582
n-value	R_0	R_{45}	R_{90}	R_{avg}
0.33	0.75	0.85	0.85	0.83

3.2.2 Experimental Procedure

AA5182-O sheets were pre-strained, annealed, and tested via tensile tests and plastic strain ratio (R-value) tests. EBSD analyses were used to investigate the post-annealing microstructure and texture. Each test is briefly summarized here.

Strain Measurement by Circle Grid Analysis

Pre-strain levels were measured by circle grid analysis but with square shape stencils. Before pre-straining, the specimens were electrochemically etched using solution LNC-2 with a stencil pattern of 2 mm $\times$ 2 mm squares, and washed by #3 cleansers. Both etching and washing chemicals were supplied by the Lectroetch Company. The etching power was 15V DC. After the specimens were pre-strained, strain was measured from the distortion of the etched square on the outer surface of a deformed part. A camera was used to capture the images of the deformed patterns while the Grid Analyzer software recorded the data. The hardware and software were developed by FMTI Systems, Inc.

Pre-straining

Sheets of AA5182-O were pre-strained in uniaxial, plane strain and equibiaxial tension to different levels, and the stretching directions were along TD, which is a worse case in formability analysis compared to rolling direction (RD). All three strain paths were used for tensile and testing; however, only uniaxial pre-strain was used to test for *R*-values.

The pre-strain levels were calculated in terms of equivalent true strain, where two assumptions were made to simplify the calculation: (a) the material was isotropic; and (b) the material volume remains constant during plastic deformation. Major and minor pre-strains were checked by grid analysis, and used to calculate equivalent strains via the formulas listed in Table 3.2.

Table 3.2 Formulas for the calculation of equivalent strains

	Strain ratio $\beta = \varepsilon_2 / \varepsilon_1$	Equivalent strain $\bar{\varepsilon} = \sqrt{\dfrac{4}{3}(1+\beta+\beta^2)}\varepsilon_1$
Uniaxial tension	-1/2	ε_1
Plane Strain	0	1.1547 ε_1
Equal-biaxial tension	1	2 ε_1

A. Pre-strain in uniaxial tension

AA5182-O blanks, 762 mm long, 190.5 mm wide, were sheared along the TD, as presented in Figure 3.2. The specimens were pre-strained at an initial strain rate of 10^{-3} s^{-1} on an Instron 5582 universal testing machine to pre-set strains controlled with a 50 mm axial extensometer. This arrangement enabled a maximum true pre-strain of 0.24.

Therefore, the true pre-strain levels were set at 0.10, 0.15 and 0.20 for the *R*-value tests and

0.15 and 0.20 for tensile testing.
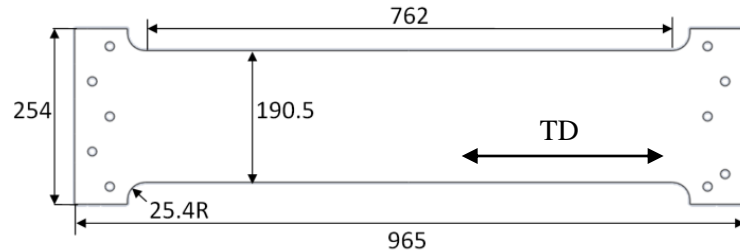
Figure 3.2 Specimen design for pre-strain in uniaxial tension (unit: mm)

B. Pre-strain in plane strain

A rectangular specimen, 305 mm wide, 635 mm long, was used for plane pre-straining

in the TD. Near plane pre-straining was performed on a hydroforming press system,

WF250, from Interlaken Technologies Corporation (ITC). A 305 mm-diameter hollow

punch and a ring-shaped (584 mm-outer diameter and 203 mm-inner diameter) mild steel

carrier blank (first suggested by Marciniak and Kuczynski [1967]) were used. To minimize

the friction between tooling and specimen surfaces, a Teflon sheet was placed between the

punch and the carrier blank, and the die radii were kept lubricated with mill oil. Lubrication

was avoided between the aluminum and carrier blanks to maximize the stretching effect in

the center of the specimen. Using the above setup, fracture occurred at an equivalent true

strain of 0.17. The maximum repeatable plane pre-strain level was set at 0.15.

C. Pre-strain in equibiaxial tension

Pre-straining in equibiaxial tension was conducted in the same ITC press, with the

same die set, carrier blank and lubricants. The only difference was the specimen geometry, where a 635 mm × 635 mm square blank replaced the rectangular shape. Fracture of the AA5182 sheet with this setup occurred at an equivalent true strain of 0.22. Thus, pre-strain levels were set at 0.15 and 0.20.

Preparation of Testing Specimens

The various tests had different requirements for specimen preparation. Specimen geometry information was listed in Ref. [Li et al., 2010]. The specimens for the tensile tests were cut from the center of pre-strained pans or blanks along the TD, into a dog-bone shape with 25 mm gage length, which geometry is referred to as "sub-sized," (following ASTM E8 [2009]) using a water jet cutter.

For *R*-value testing, the specimens were machined individually along 0°, 45°, and 90° directions with respect to RD, from the large pre-strained tensile bars that were worked to 0.10, 0.15 and 0.20 uniaxial pre-strains. Machining was employed to remove cold-worked edges and the design geometry was a standard 50-mm dog-bone shape [ASTM E517-00, 2006].

Annealing

Before mechanical testing, the pre-strained specimens were subjected to isothermal heat-treatments using a salt bath heater equipped with an auto tune temperature controller. The annealing temperature was 350°C with holding times of 10 seconds and 20 minutes. Choice of these times was based upon the fact that 10 seconds would allow recovery to

occur without grain coarsening while 20 minutes would allow recovery, recrystallization and grain coarsening [Li at al., 2011]. The temperatures of the salt bath were monitored by a K-type thermocouple with a ±5°C variation.

Testing

Post-annealing material properties were evaluated at room temperature via tensile tests and *R*-value testing.

A. Tensile tests

Sub-sized tensile bars were pulled along the TD at an initial strain rate of 10^{-3} s^{-1} on an Instron 5582 universal testing machine. An extensometer was not used to monitor displacement in these tests. The software package from Instron was able to calculate the strain from crosshead displacement and the engineering stress according to the load and cross-sectional area of the initial specimen geometry. At the same time, the machine compliance was automatically corrected by the software. Therefore, the *UTS* and *YS* refer to engineering stresses; and the strain at the *UTS* and maximum strain at fracture were simply obtained from the crosshead displacements at *UTS* and fracture, respectively.

B. Plastic strain ratio *R*-value testing

R-values were automatically measured on the Instron 5582 machine via two extensometers to record transverse and longitudinal strains at an initial strain rate of 10^{-3} s^{-1}. The transverse extensometer was an Epsilon 3575 AVG-ST with a 2mm gauge travel length. Its actual gauge length was set to 12.5 mm, the same as specimen width. The static

axial clip-on extensometer was an Instron 2630 with a 50-mm gauge length which is widely used in standard tensile testing.

C. Electron back scattered diffraction

EBSD studies were performed on the as-received and 0.15 uniaxially strained specimens at different annealing conditions (i.e. without annealing, 350°C for 10 seconds, and 350°C for 20 minutes). The EBSD specimens were prepared by cutting with a low speed precision diamond saw. The EBSD surface was mechanical polished with progressively finer water based diamond suspension (down to 1.0 μm) and then polished by 0.05 μm colloidal silica. Further electro-polishing was applied on mechanically polished specimens with standard A2 electrolyte (supplied from Struers Inc.) at a voltage of 15V for 30 seconds. The EBSD data were acquired using ZEISS FEG SEM through HKL Channel-5 camera. For statistical robustness, large areas (minimum 1×1 mm) were scanned on each specimen with high spatial resolution (with a step size of 0.5 μm or lower). The Tex-SEM Ltd (TSL) analysis software was used for routine texture analysis of the EBSD data. This included measurement of grain size and distribution, GAM values, and IPF for the as-received material and post-annealing material. The GAM quantifies the average misorientation between neighboring measurement points within a grain [Schwartz et al., 2009]. In this study, GAM values were used to understand the extent of deformation within a grain and recovery of grains after the annealing.

3.3   RESULTS AND DISCUSSION

The post-annealing properties of AA5182-O, including tensile properties and *R*-values, are presented. From the results of the statistical analysis, the important pre-strain and annealing variables were identified and their effects were analyzed. These property changes were interpreted by microstructure and texture evolutions.

3.3.1 Tensile Tests of Post-Annealing AA5182-O

In this section, the important process variables for post-annealing tensile properties were indentified through a design of experiment (DOE). The DOE is detailed in Table 3.3, where the process variables included pre-strain path, pre-strain level, and annealing condition. There were 15 conditions in total and 2 replicates for each condition.

Table 3.3 Design of experiment of sub-sized tensile tests for post-annealing AA5182-O

Variables	Levels	Settings
Pre-strain path	3	uniaxial, plane*, and equibiaxial tension
Pre-strain level	2	0.15 and 0.20 equivalent strain
Annealing condition	3	w/o anneal, 350°C for 10 seconds, and 350°C for 20 minutes

*Note: for plane pre-straining, the pre-strain is only 0.15

Figure 3.3 summarizes the post-annealing *UTS* (Figure 3.3a), *YS* (Figure 3.3b), strain at the *UTS* (Figure 3.3c), and maximum strain (Figure 3.3d) at fracture at the 0.15 pre-strain condition. With longer annealing times, the *UTS* and the *YS* decreased and larger strains were observed. Pre-strain path led to the following trends: $UTS_{uniaxial} > UTS_{plane} > UTS_{equibiaxial}$ and $YS_{uniaxial} > YS_{plane} > YS_{equibiaxial}$. Note that the strain at

55

the *UTS* and maximum strain at fracture under uniaxial pre-strain are lower than the values

under plane and equibiaxial pre-strains.

The statistics software Minitab [2009] was used to perform the analysis of variance

(ANOVA) for the main effects of the processing parameters, i.e., pre-strain path, pre-strain

level, and annealing time. The results are summarized in Table 3.4. The smaller *p*-value of

a factor means that factor is more important. The zero *p*-values listed under annealing time

indicate that it has significant impact on all four post-annealing properties; pre-strain path

has more of an effect on *UTS* and *YS* than on post-annealing strains since the *p*-values

under *UTS* and *YS* are equal to zero, smaller than the values under the strains; and

pre-strain level is important to the *UTS* with zero *p*-value. The higher the *adj.R^2*, the better

the model fits the data. The *adj.R^2* values for the four tests are all above 0.97, which means

above 97% data information can be explained by the model.   Main effects plot is a plot of

the means of the response variable for each level of a factor and across other factors

[Minitab, 2009].

Figures 3.4 and 3.5 summarize the main effect plots for post-annealing strengths and

strains, respectively, where the responses are the means of interested post-annealing

property at each level of a factor. Figure 4a confirms the trend of

$UTS_{uniaxial}>UTS_{plane}>UTS_{equibiaxial}$ and shows that *UTS* decreases with increasing pre-strain
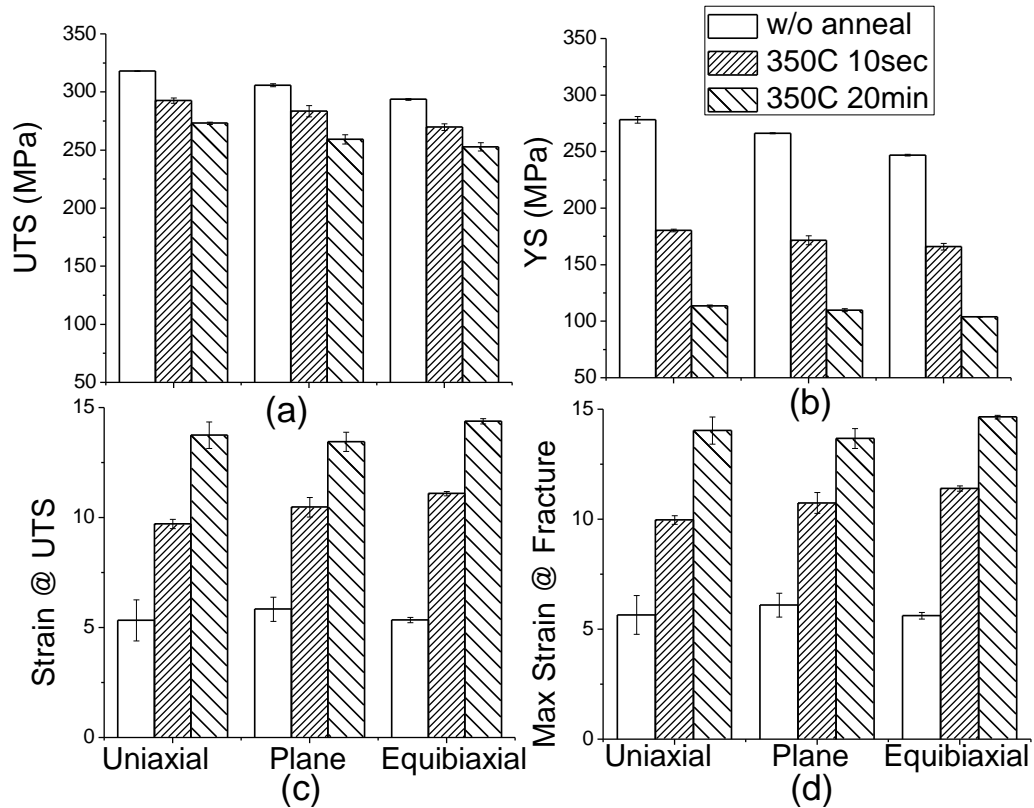
Figure 3.3 Post-annealing properties of AA5182-O for 0.15 pre-strain under different pre-strain paths and annealing conditions: (a) *UTS*, (b) *YS*, (c) Strain at *UTS*, and (d) Max Strain at Fracture

Table 3.4 Analysis of variance (ANOVA) for post-annealing mechanical properties

p-value Properties	Pre-strain Path	Pre-strain Level	Annealing	*Adj. R²*
UTS	0.000	0.000	0.000	0.973
YS	0.000	0.103	0.000	0.992
Strain @ *UTS*	0.043	0.013	0.000	0.980
Max Strain @ Fracture	0.106	0.008	0.000	0.977

level (Figure 3.4b) and extending annealing time (Figure 3.4c).   Figure 3.4d reveals that uniaxial pre-strain leads to higher *YS* values than the values at plane or equibiaxial pre-straining. Increasing pre-strain level slightly decreases *YS* (Figure 3.4e). Long

annealing time (i.e. 20 minutes) reduces the *YS* (Figure 3.4f). Annealing can extend the

post strains, i.e. strain at the *UTS* and maximum strain at fracture, as presented in Figure

3.5c and 3.5f. Compared to annealing, pre-strain path (Figure 3.5a and 3.5d) and level

(Figure 3.5b and 3.5e) have less effect on post-annealing strains, although slight decreases

in post annealing strains are observed for the conditions of high pre-strain level and

uniaxial pre-strain.
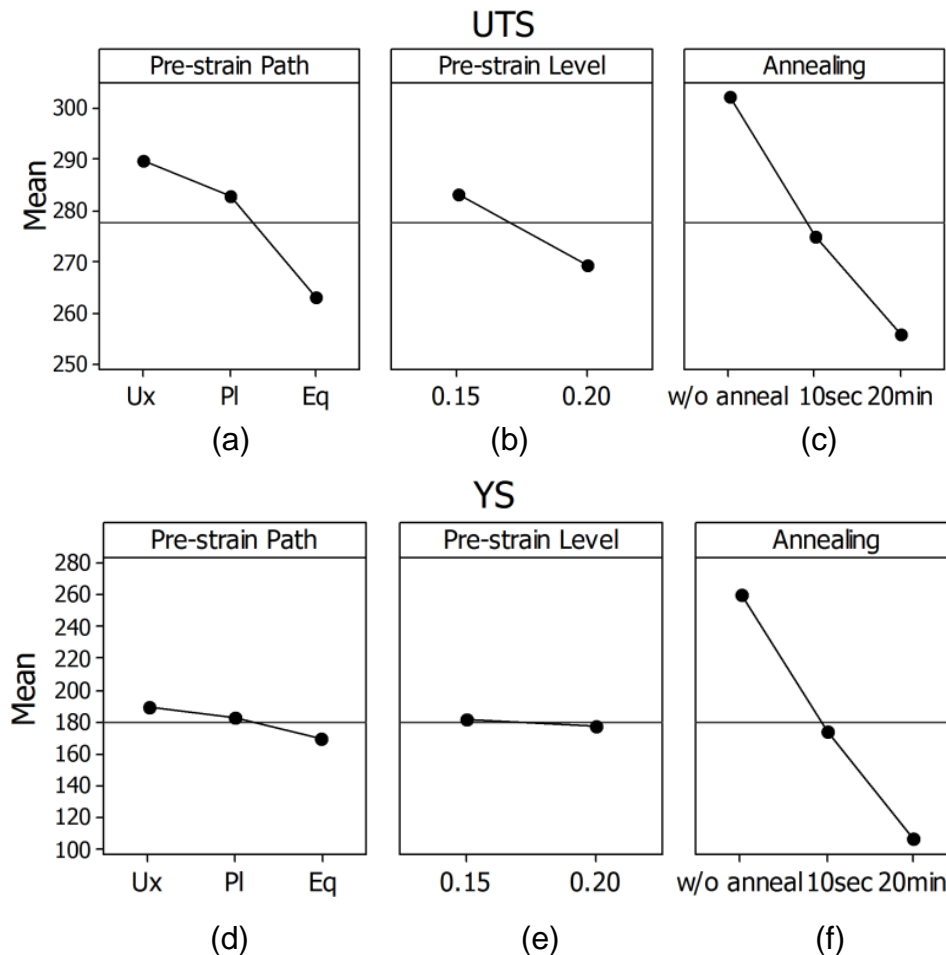
Figure 3.4 Main effect plots for post-annealing strengths of AA5182-O: (a)
pre-strain path effect on *UTS*, (b) pre-strain level effect on *UTS*, (c) annealing
effect on *UTS*, (d) pre-strain path effect on *YS*, (e) pre-strain level effect on *YS*,
and (f) annealing effect on *YS*
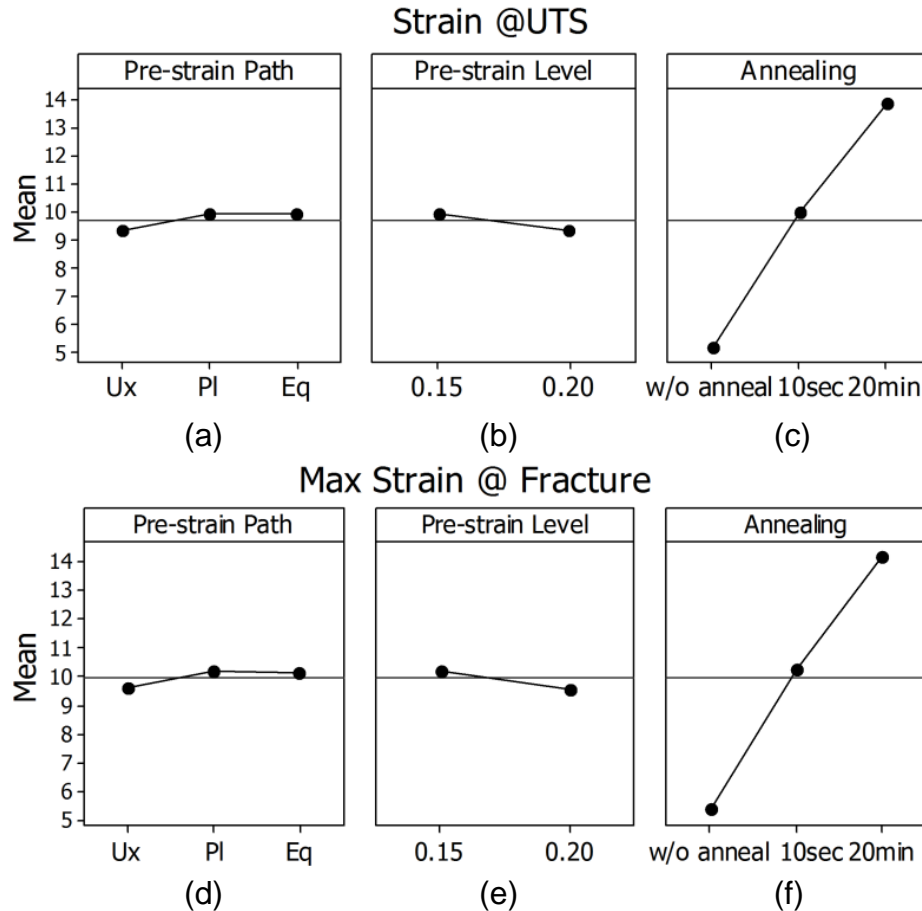
Figure 3.5 Main effect plots for post-annealing strains of AA5182-O: (a) pre-strain path effect on strain at *UTS*, (b) pre-strain level effect on strain at *UTS*, (c) annealing effect on strain at *UTS*, (d) pre-strain path effect on maximum strain at fracture, (e) pre- level effect on maximum strain at fracture, and (f) annealing effect on maximum strain at fracture

Figure 3.6 presents the IPF map and PF for 0.15 pre-strain annealed specimens. After

a 0.15 pre-strain (Figure 3.6a), a slight change in texture is observed when compared to the

specimen as-received (Figure 3.1) where the grain size did not change. It is observed from

the IPF maps of pre-strained and annealed specimens (Figure 3.6a-6c) that the grain size

increases for a long annealing time (20-minute). Texture development after 20-minute

annealing is different from the pre-strained and 10-second annealed specimen because of

complete recrystallization and grain growth. Grain size and the GAM value were plotted

(a)

(b)

Direction of the cross section

(d)

(c)
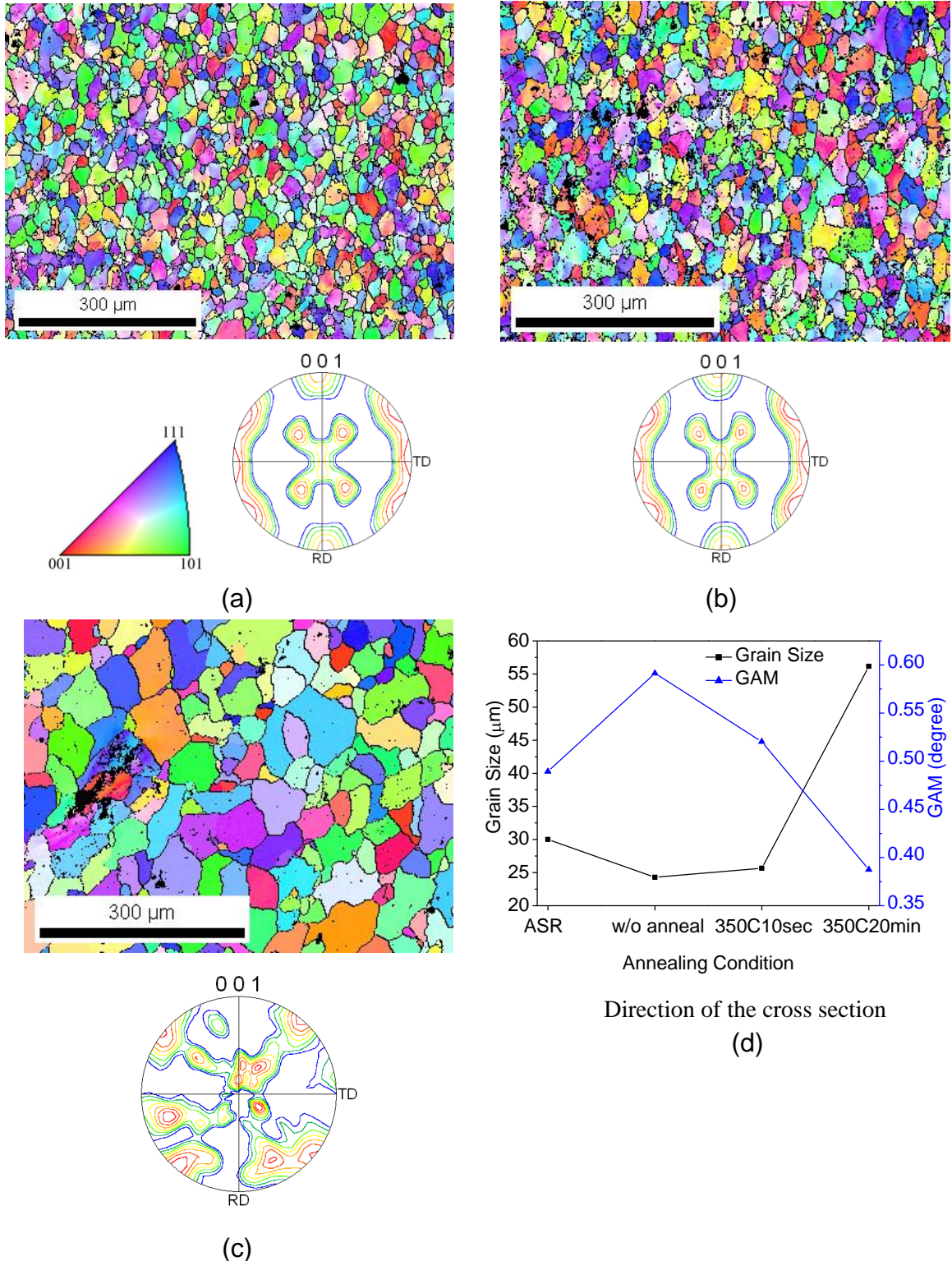
Figure 3.6 Inverse pole figure map and pole figure for 0.15 uniaxial pre-strain specimens: (a) without annealing, (b) 350°C for 10 seconds, (c) 350°C for 20 minutes, and (d) average grain size and grain average misorientation versus annealing time for 0.15 uniaxial

in Figure 3.6d, which clearly show that GAM decreases with annealing time, and after a 20-minute annealing time grain size increases enormously. The GAM value of 0.34 is approximately the same as the as-received specimen which was fully recrystallized. However, a slight decrease in GAM value as compared to the 0.15 pre-strained specimen for the specimen annealed for 10 seconds indicates a partial recovery. These results can be directly related to the mechanical properties of the post-annealing specimens. Figures 3.4c and 3.4f exhibit decreases in the *UTS* and the *YS* for a longer annealing time because of the increase in grain size [Savic et al., 2010]. On the other hand, in-grain misorientation decreased with longer annealing time, which is attributed to a decrease of stored strain energy within the grain (pre-strained grains after annealing) and this was facilitated by dislocation glide, thereby resulting in greater ductility [Hasegawa et al., 2000; Csontos and Sarke, 2005]. Therefore, larger strains occurred from longer annealing times, as shown in Figures 3.5c and 3.5f. The total effective strain was calculated by adding the equivalent pre-strain level to the post-annealing strain. In this case, the strains are in engineering scale. Figure 3.7 is an example of the total effective maximum strain at fracture that was calculated via Eq. (3.1):

$$\textit{total effective strain= equivalent pre-strain +post-anneal strain} \qquad (3.1)$$

Annealing, combined with a high pre-strain level, increases the total effective strain. An increase in total elongation after 10-second and 20-minute annealing times is caused by partial recovery and full recrystallization, respectively. This agrees with a previous study

[Li et al., 2011] of uniaxial pre-straining of tensile specimens.
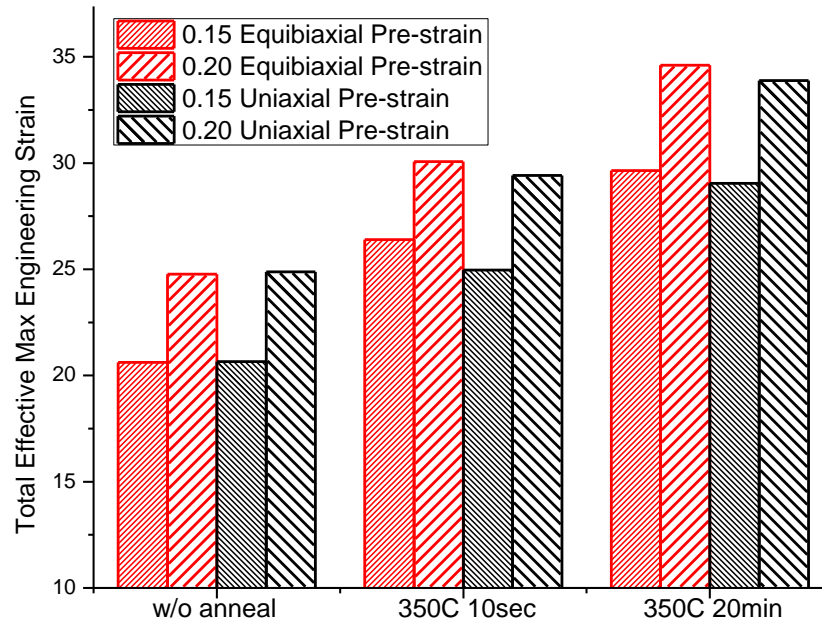
Figure 3.7 Pre-strain level and annealing effects on total effective maximum
engineering strain at fracture

3.3.2 *R*-value Testing of Post-annealing AA5182-O

R-values in different sheet directions were investigated by considering the process

variable effects detailed above. The general full factorial design is listed in Table 3.5: the

R-values were tested along 0°, 45°, and 90° directions relative to RD for 3 heating

conditions and 3 uniaxial pre-strain levels (where the uniaxial pre-strain was along 90°,

TD), and each condition was tested using 3 replicates. The *R*-values in 3 orientations were

also tested for the as-received condition as a reference, but were excluded for the DOE

analysis. The post-annealing *R*-values are plotted in Figures 3.8a to 3.8c for 0°, 45°, and 90°

directions. Figure 3.8d presents the average *R*-value ($\bar{R}$) calculated by:

$$\bar{R} = (R_0 + 2R_{45} + R_{90})/4 \tag{3.2}$$
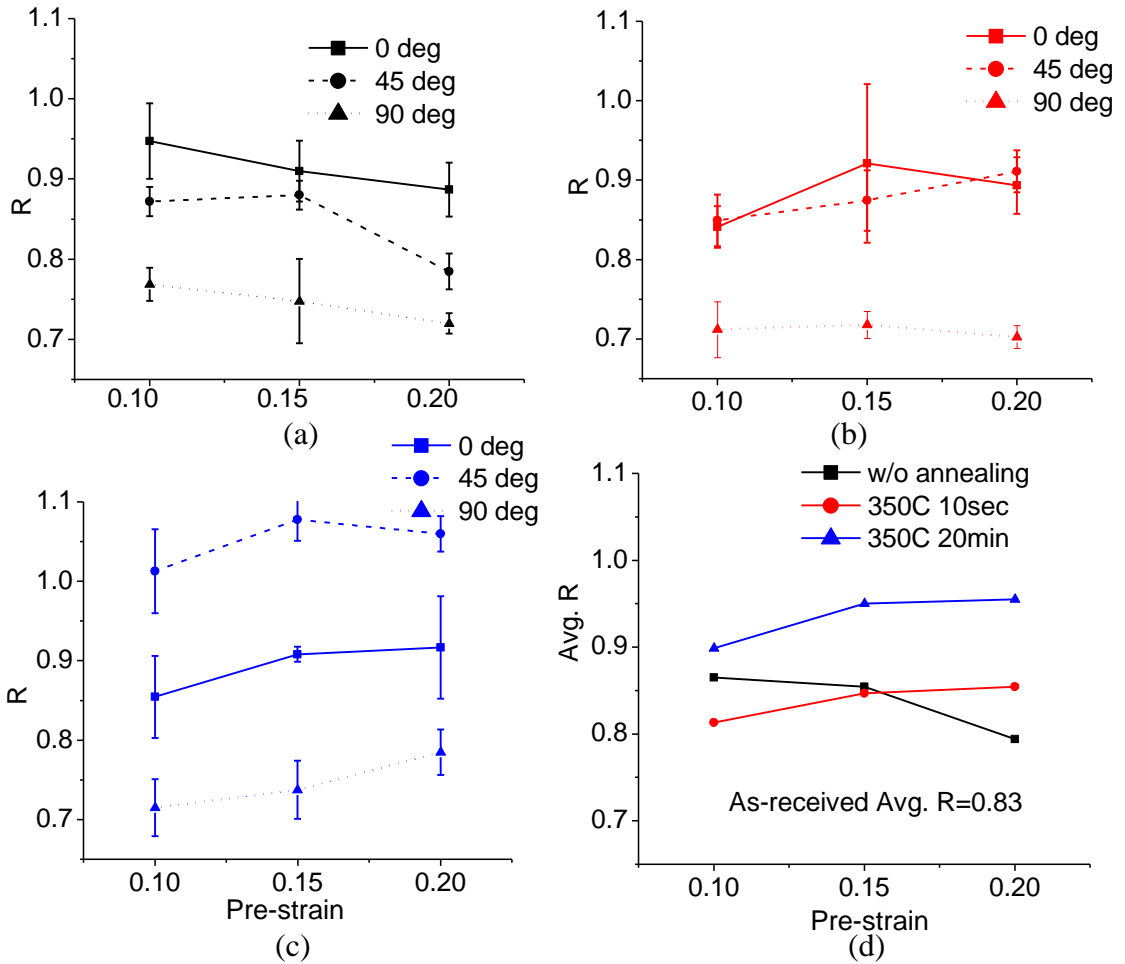
Figure 3.8 Post-annealing plastic strain ratio: (a) *R*-values along three directions for unannealed specimens, (b) *R*-values along three directions for specimens annealed at 350°C for 10 seconds, (c) *R*-values along three directions for specimens annealed at 350°C for 20minutes, and (d) *Avg.R* (from Eq. 3.2) for these three annealing conditions

The pre-strained *R*-values for unannealed AA5182-O are given in Figure 3.8a. The data points at 0.0 pre-strain refer to the *R*-value test results of the as-received AA5182-O, where R_{45} is 0.93, which is slightly higher than the supplier value (0.83) listed in Table 3.1. Since the *R*-value is defined as the ratio of the true width strain to the true thickness strain, a value that differs from 1 suggests normal anisotropy. For unannealed aluminum, as presented in Figure 3.8a, R_{90} was decreased far from unity after uniaxial pre-straining

applied along the same direction, which indicates that the anisotropy was increased. Pre-strain was found to cause first an increase in R_0 (Figure 3.8a) and then a progressive decrease. The cause of this counteraction effect was the pre-strain direction was different from the original RD. Additionally, R_{45} lies between R_0 and R_{90} when pre-strain >0.10.

After annealing, different trends of the R-values are seen at different conditions, as shown as Figures 3.8b and 3.8c. For short and long annealing times, R_{90} has a minimum value among these three directions, which is approximately 0.7. At short annealing times, i.e. 10 seconds (Figure 3.8b), the values of R_{45} and R_0 are close to each other; however, at 20 minutes (Figure 3.8c), they are separated and parallel, and $R_{90} < R_0 < R_{45}$.

Important factors affecting the post-annealing R-values were identified via ANOVA based upon the experiment detailed in Table 3.5. The ANOVA results are summarized in Table 3.6. Post-annealing R-values exhibit a high dependency of annealing conditions and specimen orientation, with a p-value of 0.000. Note that the pre-strain level with a p-value of 0.414 is not an important factor, which is also seen from the nearly flat curves for the different pre-strain levels, as shown as Figures 3.8b and 3.8c. The overall *adj. R^2* of the test is 0.686. The main effects plots are presented in Figure 3.9, and the responses are the means of a response variable at each level of a process factor and across other factors at the same time, which are different from $\bar{R}$. Annealing for 20 minutes can reduce the anisotropy and increase the R-value to 0.9; however, annealing for 10 seconds did not change the R-value significantly after pre-straining. The R_{90} has a minimum value among the three

Table 3.5 Design of experiment of *R*-value testing for post-annealing AA5182-O

Variables	Levels	Settings
Pre-strain level	3	0.10, 0.15 and 0.20
Annealing condition	3	No Anneal, 350°C for 10 seconds, and 350°C for 20minutes
Orientation	3	0, 45, and 90°

Table 3.6 Analysis of variance (ANOVA) for post-annealing *R*-value

p-value / Properties	Annealing	Pre-strain level	Orientation	*Adj. R^2*
R	0.000	0.414	0.000	0.686
$\bar{R}$	0.043	0.699		0.602
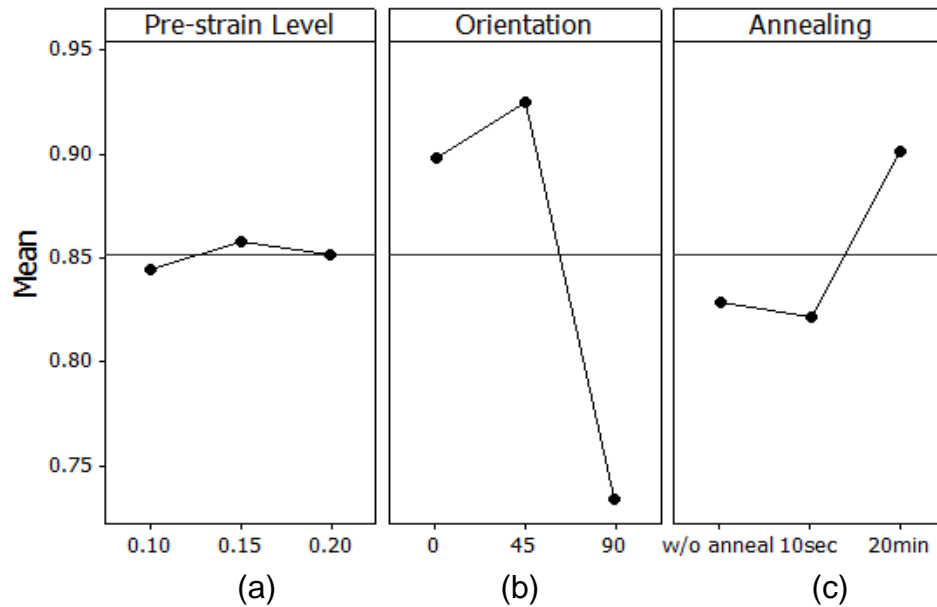
Figure 3.9 Main effects plot for post-annealing directional values of *R*: (a) pre-strain level effect, (b) orientation effect, and (c) annealing effect.

directions. Crystallographic texture of the specimen is helpful in explaining the changes in

R-value caused by annealing. The texture of the 20-minute annealed specimen is different

than both the unannealed and 10-second annealed specimens, as described in Figures 3.6a-3.6c, which is one reason for the increased R-value in the 20-minute annealed specimen.

3.4   CONCLUSIONS

The post-annealing mechanical properties of AA5182-O were investigated using uniaxial tensile testing and standard R-value testing. Pre-strain path, pre-strain level, and annealing time were the key variables investigated. Specific conclusions are as follows:

1) For post-annealing *UTS*, *YS*, strain at *UTS* and maximum strain at fracture, the pre-strain path, pre-strain level and annealing were all significant factors. It was found that for pre-strained and annealed specimens, *UTSuniaxial> UTSplane>UTSequibiaxial* and *YSuniaxial>YSplane>YSequibiaxial*; higher pre-strain levels decrease the *UTS*; and annealing reduces both *UTS* and *YS*. For the two strain levels, 0.15 and 0.20, the higher pre-strain level decreases post-annealing strains while annealing increases those strains.

2) High pre-strain levels followed by annealing were favorable for increasing the total effective strain/elongation.

3) Post-annealing R-values exhibited dependency on annealing and sheet orientation; however, pre-strain level did not show a significant effect. Long annealing time (dwell times in excess of 20 minutes) increased the R-values along three directions. Among these three directions, R_{45} was slightly higher than R_0 and R_{90}.

4) Cold work decreased the $\bar{R}$. Annealing "recovered" $\bar{R}$, increasing the value from 0.8 to 1 for a long annealing time.

5) The relationships between microstructure evolution and mechanical property changes were investigated. Annealed at 350°C for a short annealing time (10 seconds), AA5182-O partially recovered, as seen as the decrease of GAM while no significant changes in grain size and texture compared to pre-strained material. For a long annealing time (20 minutes), the grain size increased and texture became randomly. The decrease in yield stress or *UTS* after annealing was caused by the decrease of dislocation density for 10-sencond annealing (reflected by the decrease of GAM) or grain growth for 20-minute annealing. The *R*-value change was highly related to the texture change.

REFERENCES

Achni, D. Hoppersad, O. S., Lademo, O.-G., (2009), "Behaviour of Extruded Aluminum Alloys under Proportional and Non-proportional Strain Paths," *Journal of Materials Processing Technology*, 209, 4750-4764.

Aluminum Autodesign Review, (1998), The aluminum Society, 6 (3).

ASTM E517-00, (2006), "Standard Test Method for Plastic Strain Ratio r for Sheet Metal," ASTM International, West Conshohocken, PA.

ASTM E8/E8M-09, (2009), "Standard Test Methods for Tension Testing of Metallic Materials," ASTM International, West Conshohocken, PA.

Barlat, F., Ferreira Duarte, J. M., Gracio, J. J., Lopes, A. B., Rauch, E. F., (2003), "Plastic Flow for Non-monotonic Loading Conditions of An Aluminum Alloy Sheet Sample," *International Journal of Plasticity*, 19, 1215-1244.

Csontos, A. A., Sarke, E. A., (2005), "The Effect of Inhomogeneous Plastic Deformation on the Ductility and Facture Behavior of Age Hardenable Aluminum Alloys," *International Journal of Plasticity*, 21 (6), 1097-1118.

Fridlyander, I. N., Sister, V. G., Grushko, O. E., Berstenev, V. V., Sheveleva, L. M., Ivanova, L. A., (2002), "Aluminum Alloys: Promising Materials in the Automotive Industry," *Metal Science and Heat Treatment*, 44 (9-10), 365-370.

Graf, A., Hosford, W., (1993), "Effect of Changing Strain Paths on Forming Limit Diagrams of Al 2008-T4," *Metallurgical Transactions*, 24(A), 2497-2501.

Hasegawa, T. Takahashi, T., Okazaki, K., (2000), "Deformation Parameters Governing Tensile Elongation, For A Mechanically Milled Al-1.1at.%Mg-1.2at.%Cu Alloy Tested in Tension at A Constant True Strain Rates," *Acta Materialia*, 48 (8), 1789-1796.

Jun, G., Hosford, W. F., (1986), "Flow Behavior of an Aluminum-Killed Steel after Tensile Prestraining and Strain-Aging," *Metallurgical Transactions*, 17A, 1573-1575.

Krajewski, P. E., (2007), "Methods for Production of Stamped Sheet Metals Panels," US Patent 7,260,972, B2.

Lee, T. M., Hartfield-Wünsch, S. E., Xu, S., (2006), "Demonstration of the Preform Anneal Process to Form a One-Piece Aluminum Door Inner Panel," SAE Paper No. 2006-01-0987.

Li, J. J., Kim, S. Lee, T. M., Krajewski, P. E., Wang, H., Hu, S. J., (2011), "The effect of Prestrain and Subsequent Annealing on the Mechanical Behavior of AA5182-O,"

Materials Science and Engineering A, 528, 3905-3914.

Li, J. J., Hu, S. J., Carsley, J. E., Lee, T. M., Hector, Jr., L. G., Mishra, S., (2010), "Effects of Pre-strain, and Annealing on Post-Anneal Mechanical Properties and Forming Limits of AA5182-O," *Research Report*, General Motors Collaborative Research Lab in Advanced Vehicle Manufacturing, the University of Michigan.

Marciniak, Z., Kuczynski, K., (1967), "Limit Strains in the Processes of Stretch-Forming Sheet Metal," Int. J. Mech. Sci., 9, 609-620.

Minitab, version 15, (2009), Minitab Inc. http://www.minitab.com/

Narayanasamy, R., Ravindran, R., Manonmani, K., Satheesh,J., (2009), "A crystallographic texture perspective formability investigation of aluminium 5052 alloy sheets at various annealing temperatures," Mater. Design, 30, 1804-1817.

Savic. B, Hector Jr., L. G., Kim, S., Verma, R., (2010), "Local Mechanical Properties of a Magnesium Hood Inner Component Formed at Elevated Temperature," *Journal of Engineering Materials and Technology- ASME*, 132, 021006.

Schwartz, A. J., Kumar, M., Adams, B. L., Field, D., P., (2009), "Electron Backscatter Diffraction in Materials Science", Springer Science+Business Media, LLC, New York, NY, pp. 256.

APPENDIX

SPECIMEN USED IN PRE-STRAINING (UNIT: MM)

(a) Uniaxial pres-train (unformed specimen)
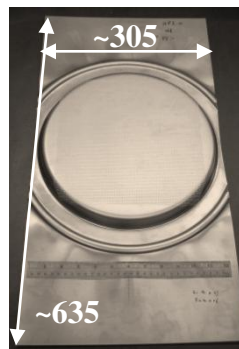
(b) Plane pre-strain (preformed specimen)
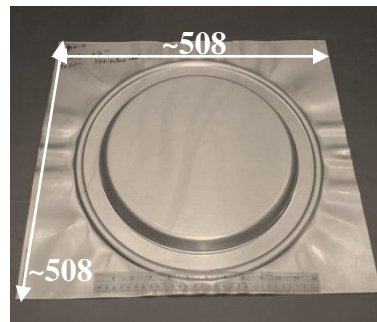
(c) Equibiaxial pre-strain (preformed part)

CHAPTER 4

FORMING LIMIT ANALYSIS FOR TWO-STAGE FORMING WITH INTERMEDIATE ANNEALING[3]

ABSTRACT

In this paper, a combined experimental/theoretical method is presented for generating stress-based forming limits for "preform annealing," a two-stage forming technique with an intermediate annealing step. Preform annealing improves the formability of Al alloys by introducing annealing which partially (or entirely) removes the cold work from the preform. Strain-based forming limits exhibit dependencies on pre-strain and annealing history that differ from point to point in the material, and hence are difficult to define and apply. We demonstrate that stress-based forming limit diagrams (σ-FLDs) exhibit dependencies on pre-strain levels, strain paths and annealing, and converge to a single forming limit curve that is close to the stress-based forming limit calculated for the as-received material. For this purpose, AA5182-O specimens were pre-strained to various levels in uniaxial, plane strain, and equibiaxial tension; specimens with smaller shapes were extracted, annealed, and tested in limiting dome height (LDH) tests. Strain fields for

---

[3] Contents of this chapter are to be submitted to *International Journal of Plasticity.*

the strain forming limit were measured with stereo digital image correlation (DIC) during each LDH test, where the onset of localized necking was identified to construct the forming limit. In the calculation of σ-FLDs, only as-received material properties were involved and the effects from pre-strain and annealing were accounted for with a proposed constant "effective plastic strain."

4.1 INTRODUCTION

Demands for reduction in vehicle mass to address the fuel efficiency have stimulated the development of new aluminum forming processes. Since aluminum lacks the formability of steels, several approaches to forming complex components have been explored in the literature. Among these are warm forming, viscous pressure forming, electromagnetic forming, superplastic forming quick plastic forming. Manufacturing complex aluminum shapes in an efficient and cost-effective process is still challenging. A promising approach is a 2-stage forming process where aluminum is partially formed only to have the work hardening partially (or completely) removed with an intermediate rapid annealing step prior to final forming. During annealing, the cold worked material releases the higher internal energy caused by preform and restores the ductility through static recovery, recrystallization and grain growth, three fairly distinct processes. Recovery decrease the dislocation density without observable change in grain size; recrystallization replaces the cold-worked microstructure by a new set of strain-free grains; and when the

new strain-free grains are annealed for an extended time, there is a progressive increase in grain size [Dieter, 1986]. However, too much annealing can lead to grain coarsening and associated degradation of mechanical properties.

So far, the combination effects of pre-strain and annealing on the forming limit criteria, such as strain-and stress-based forming limit diagrams, have not been reported. Strain-based forming limit diagram (ε-FLD) is an important tool for the numerical analysis of sheet metal forming process. They were first developed by Keeler [1964] and Goodwin [1968] to describe the failure curve on the onset of localized necking in a plot of major vs. minor true strains. ε-FLDs are changed by non-proportional strain paths, as reported in both experimental research [Nakazima et al., 1968; Graf and Hosford, 1993] and numerical simulation [Chu, 1982; Needleman and Tvergaard, 1984; Barata da Rocah et. al., 1984-1985; Gotoh, 1985, Kuroda and Tvergaard, 2000]. Thus, ε-FLD is not a useful tool in the simulation of multistage forming and the situation may become more complex when annealing was introduced. Another important formability analysis tool is stress-based forming limit diagrams (σ-FLDs) which specify the forming limit curve on the onset of localized necking in a plot of major vs. minor stresses, was shown to be path-independent [Marin et al., 1953; Gronostajski, 1984; Arrieux et al., 1987; Zhao et al., 1996; Stoughton, 2000, 2001]. The path-independence of σ-FLDs was found to be true when the material hardening behavior is close to isotropic. Both experimental [Wu et al., 2005; Yoshida et al., 2007] and theoretical [Kuwabara et al., 2005; Yoshida et al., 2005] research confirmed this

point. Additionally, the choice of material models affects on the location of σ-FLDs, but will not change their path-independence. This has been reviewed by Stoughton and Zhu [2004], who checked a wide range of material models from Von Mises, Hill, and Barlat models for the yield surface, associated and non-associated flow rules, power law and Voce law stress–strain relations. However there is no research available on how annealing changes both the ε-FLDs and σ-FLDs. The experimental studies from Li et al. [2011, 2011] showed that the yield strength, strain-hardening behavior and anisotropy of AA5182 change with different pre-strain and annealing treatments and the parameters in the material models, such as strain-hardening parameters in the Voce rule and R-value, vary during the process of preform annealing. But the changes introduced by preform and annealing on forming limits are not very clear.

The present study aims to clarify the effects of non-proportional strain paths and annealing on the forming limits and to develop a practical method by combining experimental/theoretical analysis to generate σ-FLDs for this 2-stage forming with an intermediate annealing. In this research, aluminum alloy 5182-O was pre-strained to various levels in uniaxial, near-plane-strain, and equibiaxial tension, annealed and tested in limiting dome height (LDH) tests to obtain forming limits along three strain paths. 3D digital image correlation (DIC) was applied to capture the strain history during each LDH test, which has the capability for direct observations of necking generations. A constant "effective plastic strain (*EPS*)" is proposed to evaluate the effects of pre-strain and

annealing by overlapping the strain hardening curves of post-annealed material with that of the as-received material and applied as an input with the as-received material parameters to calculate the stress stage from strain stage. This method is compared to the approach by incorporating the strain hardening parameters of post-annealed aluminum with Voce rule. The influences of pre-strain and annealing on the forming limit strain/ stress and stress history are discussed in detail.

4.2 EXPERIMENTAL PROCEDURE

Aluminum sheet 5182-O was pre-strained, annealed and tested in the LDH system to develop post-annealing FLDs in both strain and stress spaces. Specimens were pre-strained in uniaxial tension, plane strain and equibiaxial tension to different levels that were checked by circle grid analysis (CGA). Then, smaller specimens were cut from the center of the pre-strained specimens to three geometries followed by annealing treatment for short and long holding times. Finally, these three geometries were deformed in a 50-mm LDH tester or in a uniaxial tension test machine to obtain the forming limits along three strain paths and the strains were measured via CGA and DIC methods.

4.2.1 Materials

Commercially available aluminum sheet alloy 5182-O at 1.1 mm gauge was used with the chemical composition by weight percent of $Al-Mg_{4.3}-Mn_{0.34}-Fe_{0.21}-Si_{0.03}$. The average grain size measured by the ASTM E112 [2004] three-circle intercept method was

21.2 μm. Table 4.1 summarizes mechanical properties in the as-received condition.

Table 4.1 Typical mechanical properties of AA5182-O as-received

Yield stress (MPa)	Ultimate tensile stress (MPa)	Uniform elongation (%)	Total elongation (%)	Young's Modulus (GPa)
128	282	23.4	25.4	69

$\bar{R}$	Poisson's Ratio	Voce Law: $\bar{\sigma} = A - B\exp(C\bar{\varepsilon})$		
		A	B	C
0.86	0.31	358.58	230.42	-11.37

4.2.2 FLD Development

Before FLD testing, the materials were pre-strained to 2 levels (0.15 and 0.20 equivalent true strain) in uniaxial, near-plane-strain, and equibiaxial tension; and then the specimens with three smaller shapes were extracted and annealed. The experimental details pre-straining and annealing can be found in Section 3.2.3, 3.2.4 and 3.2.6. The following will introduce the testing procedure for FLD development using CGA and DIC methods.

FLD Development by CGA

CGA method was applied to measure the strains of the post-annealed specimens that were deformed on a LDH system. The experimental details on CGA measurement were introduced in Section 3.2.3. Square gridded specimens in different geometries were stretched in the LDH die set with an SP150 servo-hydraulic, double action press from Interlaken Technologies Corp. (ITC). The LDH die used a 50 mm-diameter hemispherical punch with 100 mm diameter lock beads at clamp loading of 267 kN for pure stretch

deformation of all specimen shapes that was sufficient to prevent material draw-in across the lock bead. The punch speed was 0.762 mm/s in stroke control with a load drop trigger of 5% to stop the test as strain localized into a "neck." To minimize the strain path change caused by friction, Teflon sheet was used as lubricant between the punch and the specimen. Specimen shape for the equibiaxial strain path was a 108 mm square blank. To obtain a near-plane strain path, 50 mm × 178 mm rectangular blanks were used. For strain paths on the left-hand side of FLD, a standard tensile bar [ASTM E8, 2009] with shorter grip section was stretched over the punch with Teflon lubricant, where the overall length of the tensile bar was 178 mm and gage section was 50 mm long by 6 mm wide.

FLD Development by DIC

Three-dimensional strain mapping was recorded during forming testing via 3D DIC, where the necking development and failure mode were captured. The DIC technology has the capability to identify the onset of diffuse necking and localized necking. These results cannot be achieved with the traditional circle grid method [ASTM E2218, 2008] which can only measure the surface strains over a grid of the final deformed specimens. The strain-based forming limits were determined using the localized necking strains. Strain data were subsequently used in the calculation of stress-based forming limits.

A. DIC Method and Image Acquisition Process

Stereo DIC is a non-contact optical method for measuring three-dimensional displacements and strain mapping on a surface by tracking and comparing the non-uniform

random patterns of a specimen [Reedlunn, et al., 2011]. DIC involves comparing two digital images of a deformed surface taken at different times to obtain a quantitative, point-by-point mapping of the strain fields (i.e., the deformation). The deformation is obtained by optimizing a cross-correlation function to match the local gray scale intensity values of a reference image and a subsequent image of the deformed specimen surface. A sequence of images is captured with time during the test to obtain the evolution of deformation. The reference image, usually taken as the first image of the undeformed specimen, is used to calculate the accumulated strain by comparing it with subsequent images of deformed material. Incremental strain is calculated by comparing one image to the next in the sequence. The 3D DIC method utilizes two cameras that image the specimen from two viewpoints, which enables calculation of out-of-plane displacements.

B. Pattern Application

Speckle patterns on the sample surface were required for the DIC analysis. After pre-straining, trimming and annealing processes, fine patterns of white and black spray paint were applied to each specimen. Specimens were first coated with a thin layer of white spray paint onto which was applied a light spray of black paint mist to create the random speckle pattern, as seen as Figure 4.1a. The resulting gray-scale contrast pattern facilitated the determination of pixel subsets from image to image in the DIC analysis. It was important to make sure that there was no single feature in the contrast pattern exceeding the chosen subset size. For this purpose, the black speckles ranged from 0.5 to 1 mm.

C. Forming Process for FLD Development via DIC

In addition to using the LDH test for near-plane and equibiaxial strain paths in the

FLD, standard tensile tests were used for uniaxial strain path FLD development. The

LDH test procedure was the same as described before, and two DIC cameras were placed

on the top of the press to focus on the spray painted surface. Because of its high-speed

frame rate, the DIC system is able to capture the necking development during uniaxial

tensile testing.   So for uniaxial strain development, a sub-size tensile specimen [ASTM E8,

2009] with speckle patterns was stretched on an Instron 5582 instead of the LDH test to

ensure a linear-strain path, and the DIC cameras were placed in front of the Instron tensile

machine (Figure 4.1b).
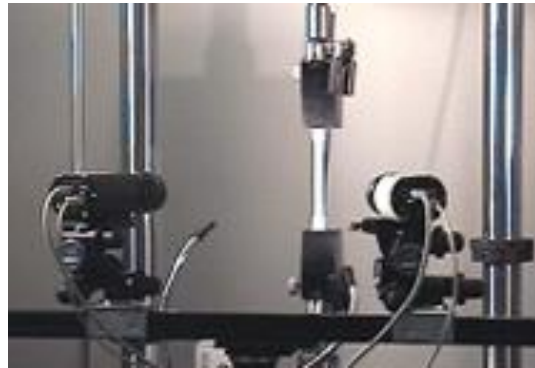
(a)   (b)
Figure 4.1 Preparation of DIC setup: (a) Pattern application, and (b) Setup of DIC
cameras [Correlated Solutions, Inc.]

D. The Current 3D DIC System

In the present study, the stereo DIC system included image acquisition software

Vic-Snap and post-processing package VIC-3D 2009 from Correlated Solutions, Inc.   The

system recorded the images using two Grasshopper™ CCD Cameras (from Point Grey Research, Inc.) and data acquisition software Vic-Snap. The cameras have a 16-bit grayscale with 2448×2048 pixel resolution and can capture images at a maximum frame rate of 15 fps. For post-processing, a set of square sub-elements was used to calculate the strain mapping. The set of sub-elements were the collections of a neighborhood of pixels with a typical size of 21×21. The image correlation algorithm tracked the location of unique contrast features corresponding to the center of each sub-element; computed an average displacement of the sub-element centers on each image from both cameras; and then these positions and displacements were analyzed to compute a strain at each point [Zavattieri et al., 2009]. In this way, the algorithm computed the entire 3D displacement and strain fields of the deformed specimen. Strain accuracy of the system is up to 0.005%.

E. The Onset of Diffuse and Localized Necking

Two types of necking were identified via DIC technology: diffuse necking or the limit of stable flow [Dewhurt et al., 1981] and localized necking - the non-uniform strains generated through thickness [Bressan et al., 1983]. From DIC images, a point with maximum major strain (ε_1) before fracture was identified by post-processing software VIC-3D. The strain history of this point was extracted and analyzed. The onset of diffuse necking can be identified by a significant increase of the strain rate ($\dot{\varepsilon}_1$) that leads to instability. For aluminum alloys, localized necking is quickly followed by fracture [Beaver, 1982]. Figure 4.2 is the strain rate history of the point with maximum major strain prior to

fracture (i.e. $\dot{\varepsilon}_1$ at the point with max ε_1 before fracture). This is an example for plane strain

path development where the specimen was pre-strained 0.15 along uniaxial tension and

without annealing. The significant increase shown as A indicates the onset of diffuse

instability and the last data point B indicates the start of localized necking. A direct

observation of thickness reduction (local necking) is observed from 3D DIC strain

mapping, which confirms the occurrence of local necking.

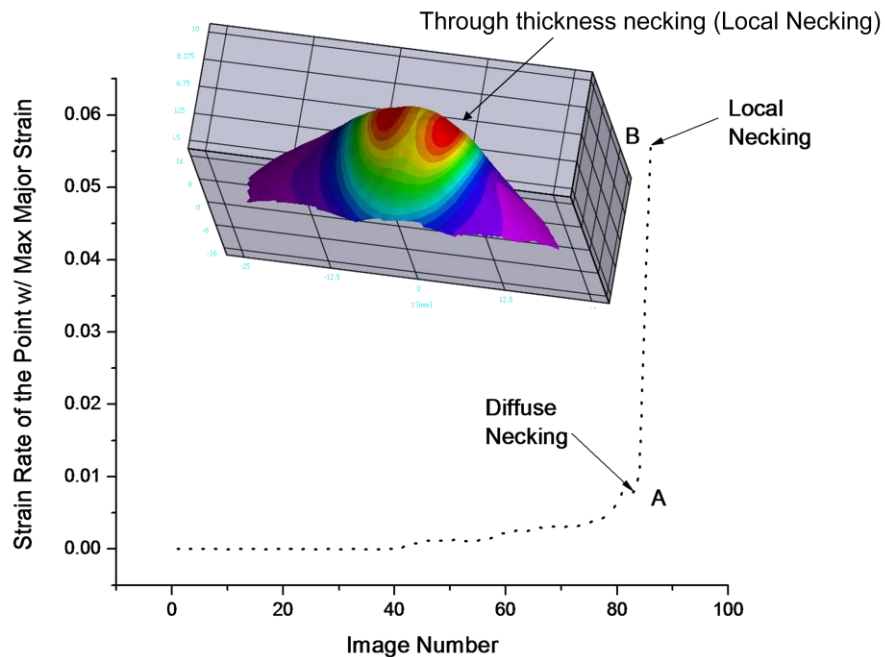Figure 4.2 Determination of diffuse and localized necks from strain rate ($\dot{\varepsilon}_1$) of the

point with maximum major strain (maxε_1)

4.3   STRAIN-BASED FORMING LIMIT DIAGRAMS (ε-FLDs)

This section describes post-annealing and total effective FLDs of AA5282-O in strain

space, and summarizes their dependence on annealing, pre-strain path and pre-strain level.

Post-annealing strain-based FLD (ε-FLD) refers to the ε-FLD measured on samples after they have been pre-strained and annealed. Total effective forming limits were calculated by adding the principle strains of pre-strain to the post-annealing forming limits, which reflect the effective or final forming limit after pre-strain and annealing. The following forming limits represent the onset of localized instability through-thickness rather than diffuse necking.

4.3.1 As-Received AA5182-O (ε-FLD)

Figure 4.3 summarizes the as-received FLDs obtained from different approaches, i.e. CGA, DIC and the supplier. In the test, the major true strain, ε_1, was parallel to the transverse direction (TD). With the CGA method, the FLC indicated as the solid green line in Figure 4.3 was artificially drawn between the good data points (safe region) and the necking region. The FLC determined via DIC was achieved by connecting the points of the onset of localized neck from different strain paths. The FLC based on localized necking is higher than the limit from diffuse necking, as expected. The forming limit measured from diffuse necking is more conservative; however, it is affected by extrinsic conditions such as sample geometry and surface quality. The FLC measured from CGA is similar to the values determined by localized necking, but higher than the curve of diffuse necking. The standard FLC (gray dashed line) is located between the curves of localized and diffuse necking, and included here to provide confidence that the current measurements are similar in magnitude.
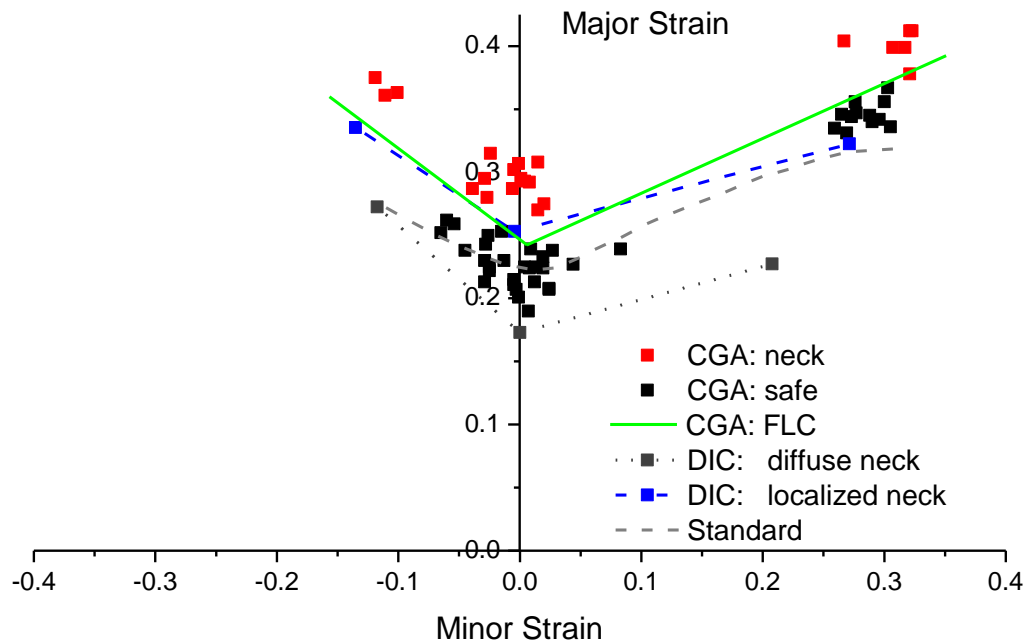
Figure 4.3 FLD of AA5182-O as-received

4.3.2 Post-Annealing ε-FLDs

Annealing Effect

Annealing can improve the formability of pre-strained aluminum by recovering the cold work, allowing dislocations to annihilate and relieve the grain structure of accumulated residual stress. The annealing effect is summarized in Figure 4.4 where three sets of conditions (i.e. no_anneal, short (30-second) and long (20-minute) annealing times) are compared for 0.15 plane pre-strained and 0.2 uniaxial pre-strained specimens. For these two pre-strain examples, it can be observed that pre-strained specimens without annealing exhibit the worst formability; the forming limits become higher after annealing; and for the long annealing time when the material is fully recrystallized and the grains have coarsened [Li et. al., 2010, 2011], the forming limits are close to the FLC of the as-received
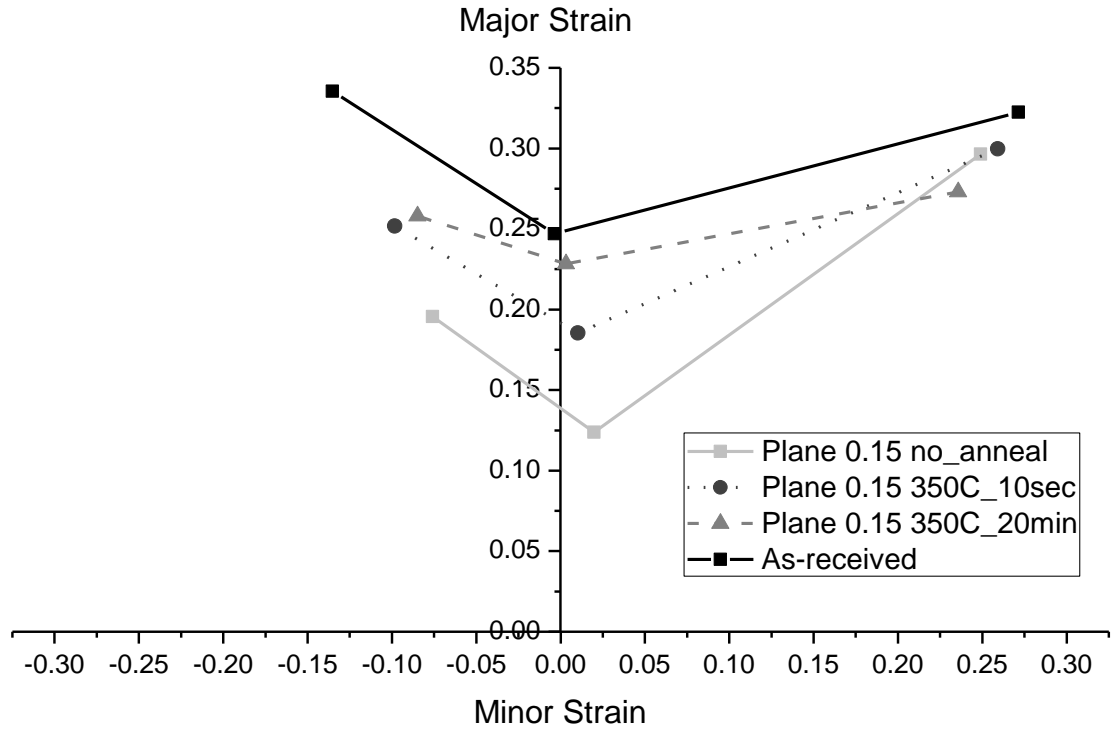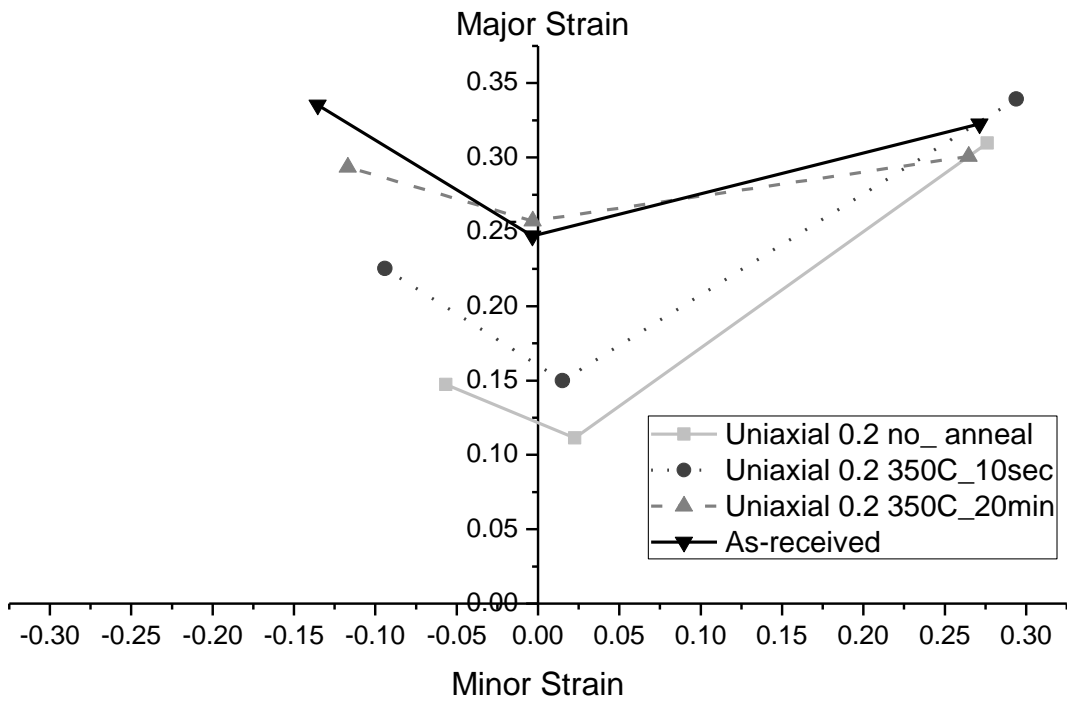
Figure 4.4 Annealing effects on post-annealing FLDs: (a) 0.15 plane pre-strain, and (b) 0.2 uniaxial pre-strain

condition. For 20-minute annealing, the forming limit for 0.15 plane pre-strained material

is slightly lower than the limit at 0.2 uniaxial pre-strain. One reason is that the lower

pre-strain level does not provide as great of a driving force for recrystallization as a higher

pre-strain level that imparts higher stored strain energy in the microstructure. Another

observation of the equibiaxial strain path of the FLD shows that the limits for different

conditions appear to be converging to a common level that may be close to the fracture

limit of this material. The plane strain limit (FLD_0) appears to be shifted to the right of the

axis with extended annealing time. This is an artifact of the non-linear strain path inherent

in the LDH test as presented in Figure 4.5. The strain history of the FLD_0 in the dome test

is plotted in strain space, where the strain path initially shifts to the left (perhaps from

elastic loading), then rapidly moves toward the right (as the sample is dominated by
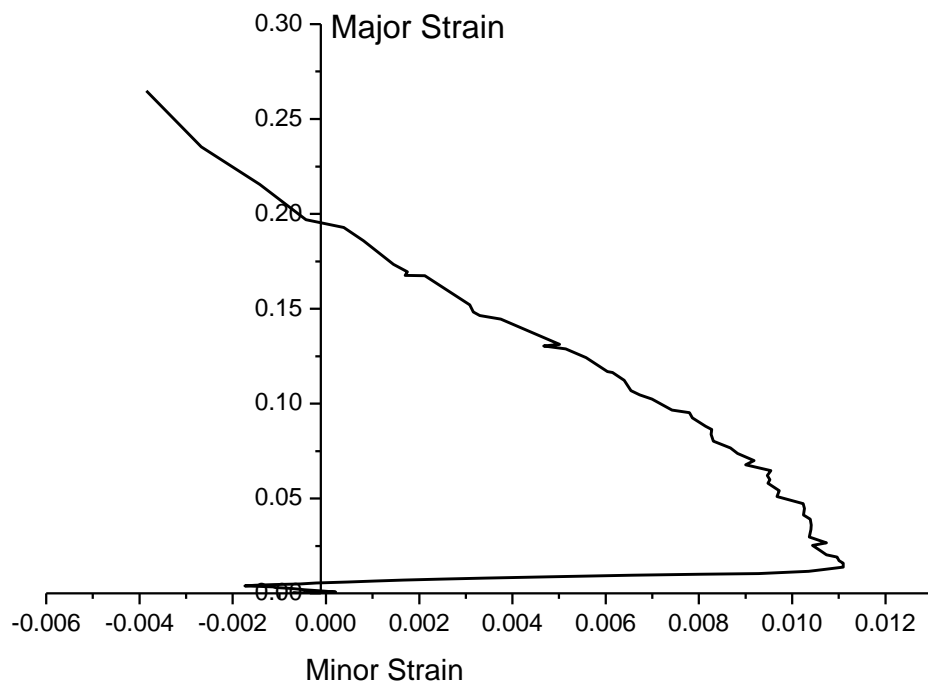
Figure 4.5 Nonlinear strain path of FLD_0 in 50mm LDH test

bending), and finally adjusts leftward back toward the axis with increasing plane stretch

deformation.

<u>Pre-Strain Path Effect</u>

The effect of varying the pre-strain path on post-annealing FLDs is summarized in

Figure 4.6. In the cases (a-c), the specimens were pre-strained at 0.15 true equivalent

strain for three heating conditions (i.e. no_anneal, 350°C_10 seconds, and 350°C_20

minutes) , and (d) is the case for 0.2 pre-strain.   In each case, the FLD of the as-received

condition is included for reference. It is found that for each case, changing pre-strain

paths has little effect on the post-annealing FLDs, and annealing effect is shown to raise the

forming limits.   The shapes of FLDs and the value of FLD_0 are similar for different

(a)

(b)

(c)

(d)
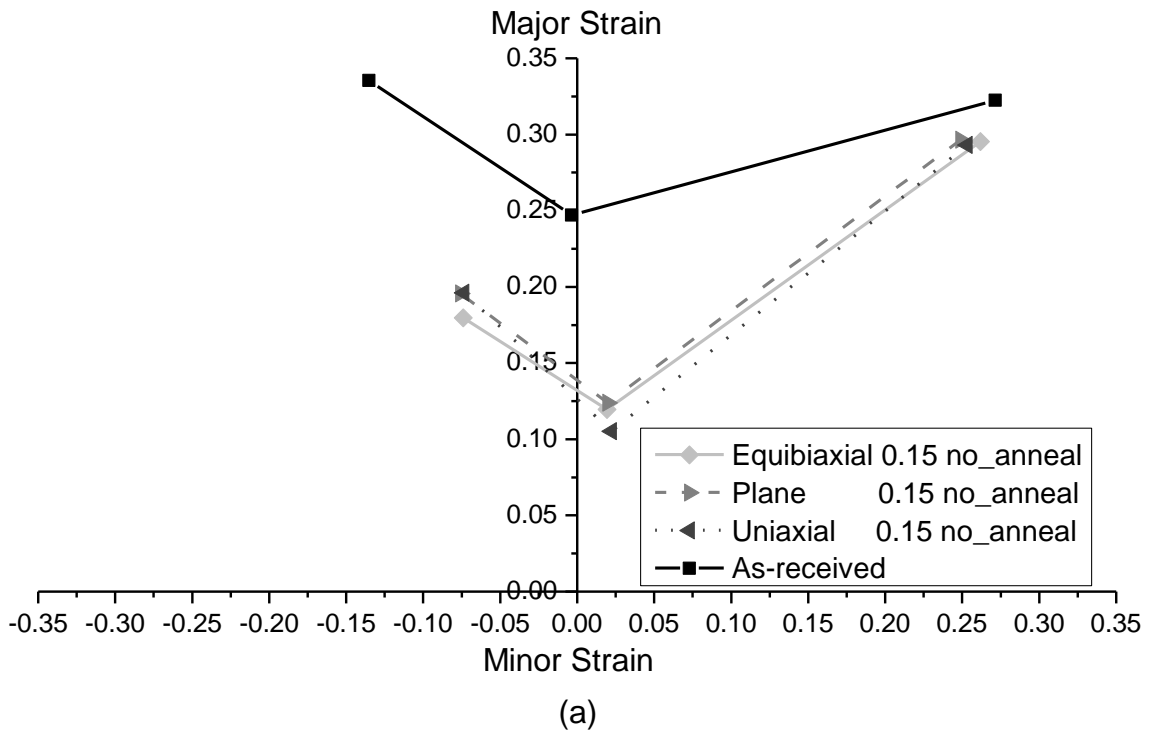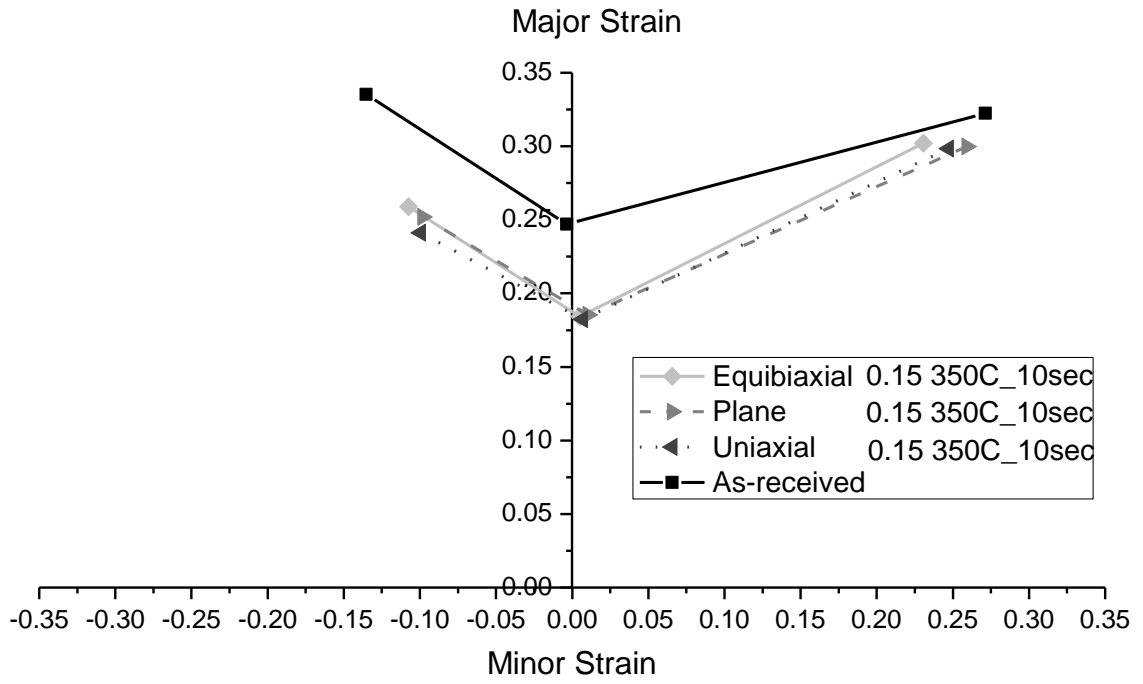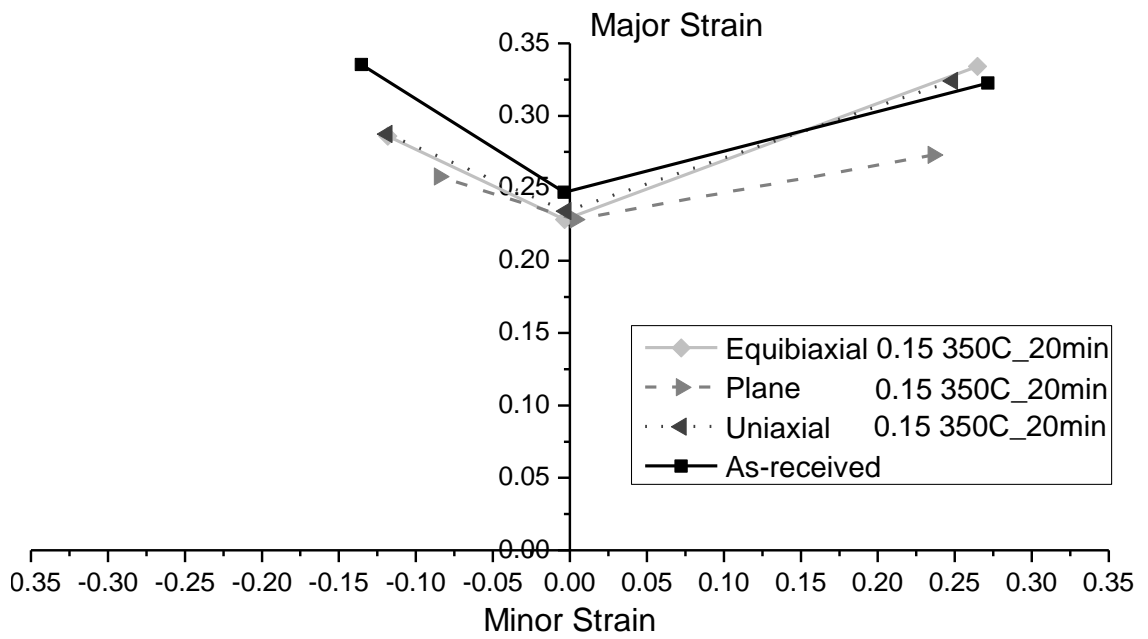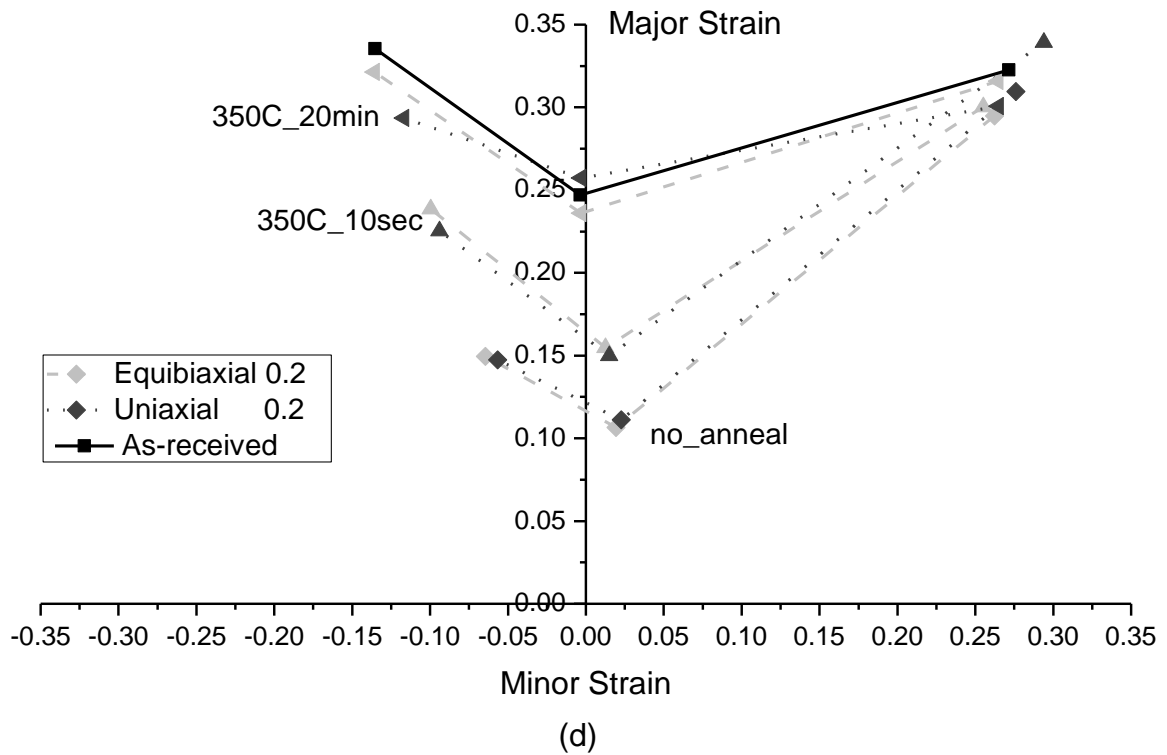
Figure 4.6 Pre-strain path effect on post-annealing FLDs: (a) 0.15 pre-strain no anneal; (b) 0.15 pre-strain, annealing at 350°C for 10 seconds; (c) 0.15 pre-strain, annealing at 350°C for 20 minutes; and (d) 0.2 pre-strain for three heating conditions

pre-strain paths at the same annealing condition. The equibiaxial thinning converges to the same point in the end. This observation is different from the results of Graf and Hosford [1993].

Pre-Strain Level Effect

Specimens with different pre-strain levels were tested for equibiaxial and uniaxial pre-strains as presented in Figures 4.7a and 6b, respectively. For equibiaxial pre-strained specimens, 0.15 pre-strain results in greater formability than 0.2 pre-strain for the no_anneal condition; this observation is more apparent on the left side of the FLD. With a

88
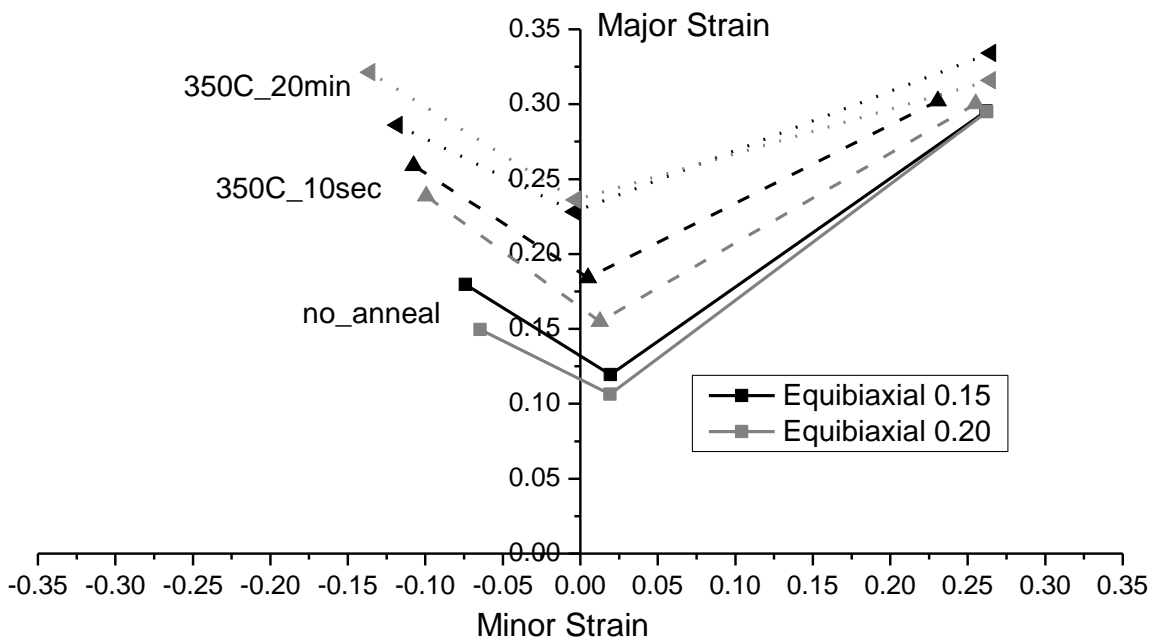
(a)
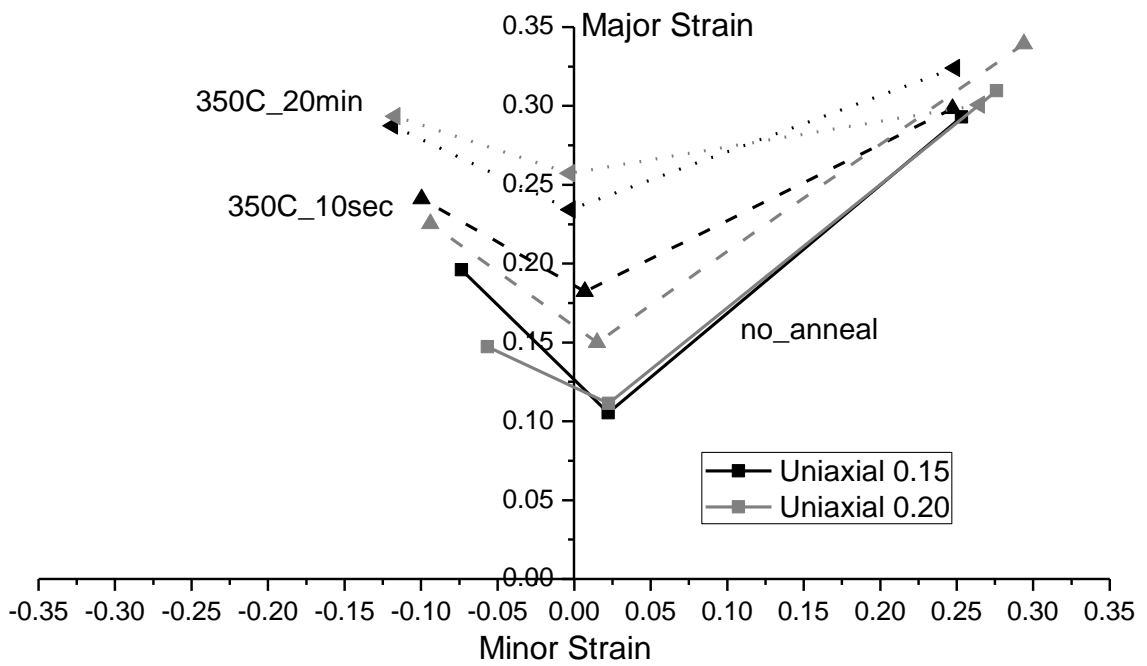
(b)

Figure 4.7 Pre-strain level effect on post-annealing FLDs: (a) pre-strain in equibiaxial tension, and (b) pre-strain in uniaxial tension

short annealing time (i.e. 10 seconds), the 0.15 pre-strained specimen still has a higher

forming limit. However, longer annealing time changes the trend: the 0.2 pre-strained

specimen exhibits higher formability because of the higher driving force for

recrystallization/grain growth. Similar behavior is observed for the uniaxial pre-strained

specimens as presented in Figure 4.7b.

4.3.3 Total Effective ε-FLDs

Annealing Effect

Figure 4.8 summarizes the 0.20 uniaxial and equibiaxial pre-strained specimens at

three annealing conditions, and the as-received data are included for reference. Annealing

is found to raise the curves, higher for a longer exposure time. The pre-strained and no_
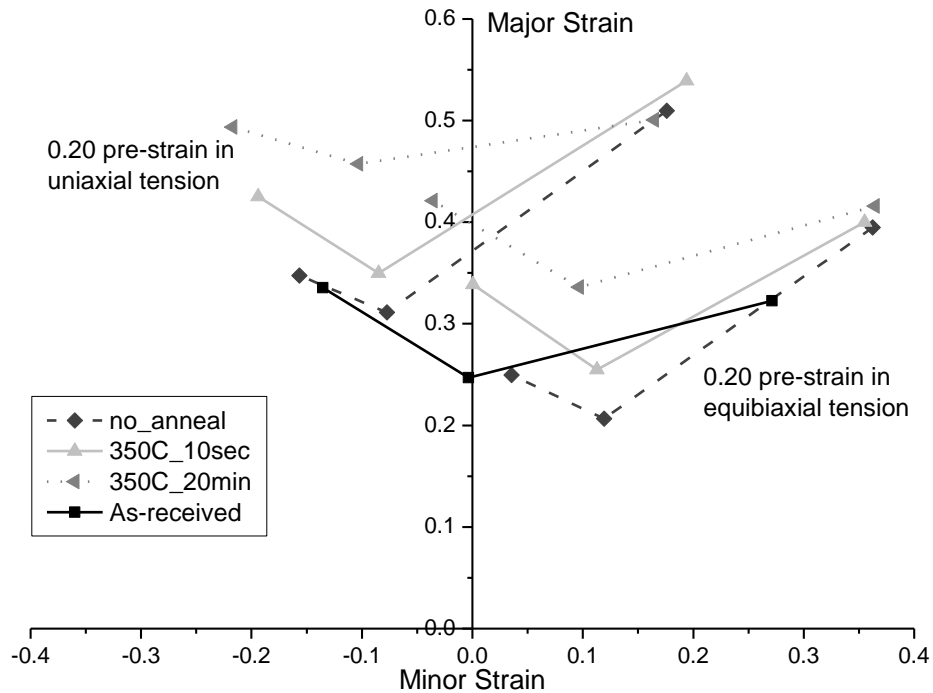
Figure 4.8 Annealing effect on total effective FLD: showing data are for 0.2
pre-strained specimens

90

anneal specimens have the lowest formability.   Specimens annealed for 20 minutes have the highest forming limits.   Formability for specimens annealed for 10 seconds is in the middle of the three conditions.   In addition, 20-minute annealing increases the FLD_0 from (-0.00, 0.25) in as-received condition to (0.10, 0.34) and (-0.10, 0.46) for equibiaxial and uniaxial pre-strained specimens, respectively, where the ε_1 is ~1.5 times the as-received value.

Pre-Strain Path Effect

Initial deformation along the pre-strain path shifted the total effective forming limit curves along those directions.   In Figure 4.9, three pre-strain paths (equibiaxial, plane strain and uniaxial tension) are compared for the 0.15 equivalent pre-strained specimens that were tested with the no-anneal condition.   The FLDs are shifted to the right and left by equibiaxial and uniaxial pre-strains, respectively, while plane pre-strain shifted the curves vertically, i.e. maintained minor strain close to zero.   In these three cases, the FLC shift for 0.15 pre-strain shows no increase in forming limits.   For the equibiaxial pre-strained case, the lower forming limit compared to the as-received data indicates a decrease in formability.   Under the same equivalent pre-strain and annealing condition, the uniaxial pre-strained specimen shows higher forming limits than the equibiaxial pre-strained sample.   A similarity is presented in Figure 4.8.
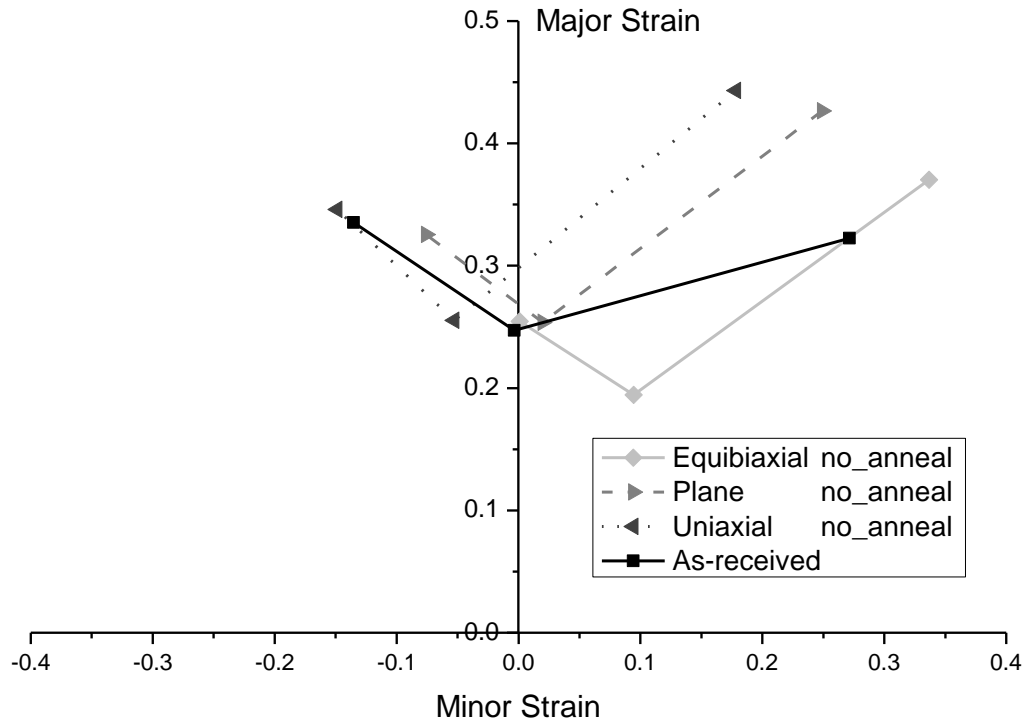
Figure 4.9 Pre-strain path effect on total effective FLD: showing data are for 0.15 pre-strained specimens

Pre-Strain Level Effect

Large pre-strains can slightly increase formability. The pre-strain level effect is presented in Figure 4.10 where three sets are given for the specimens at conditions of no_anneal, 350°C_10 seconds and 20 minutes, and they were tested for 0.15 and 0.2 uniaxial and equibiaxial pre-strains. In the equibiaxial pre-strain case, 0.2 pre-strain does not cause a significant increase in the forming limit on the right side of the diagram (i.e. equibiaxial strain path), but more apparent increase are seen in the left side, the uniaxial strain path. 0.15 and 0.2 uniaxial pre-strained specimens exhibit similar failure points along the uniaxial strain path for the no-anneal specimen (Figure 4.10a); however when the material was annealed for a short time (Figure 4.10b), the 0.2 uniaxial pre-strained sample

shows higher formability which becomes clearer with a longer annealing time (Figure
4.10c).

(a)

(b)

(c)
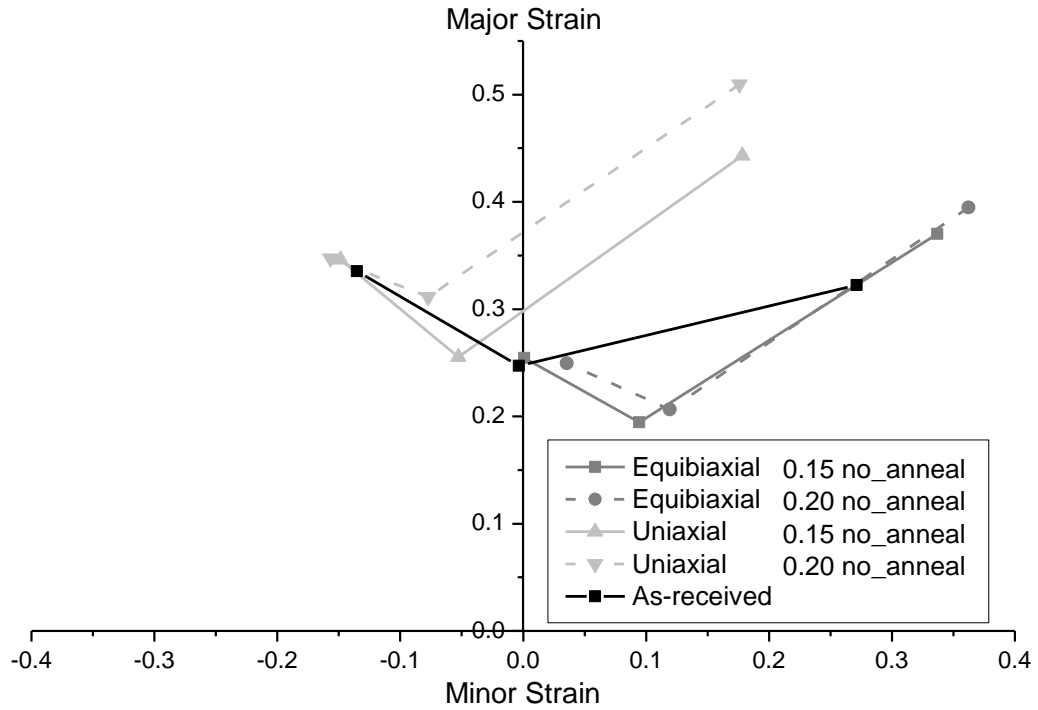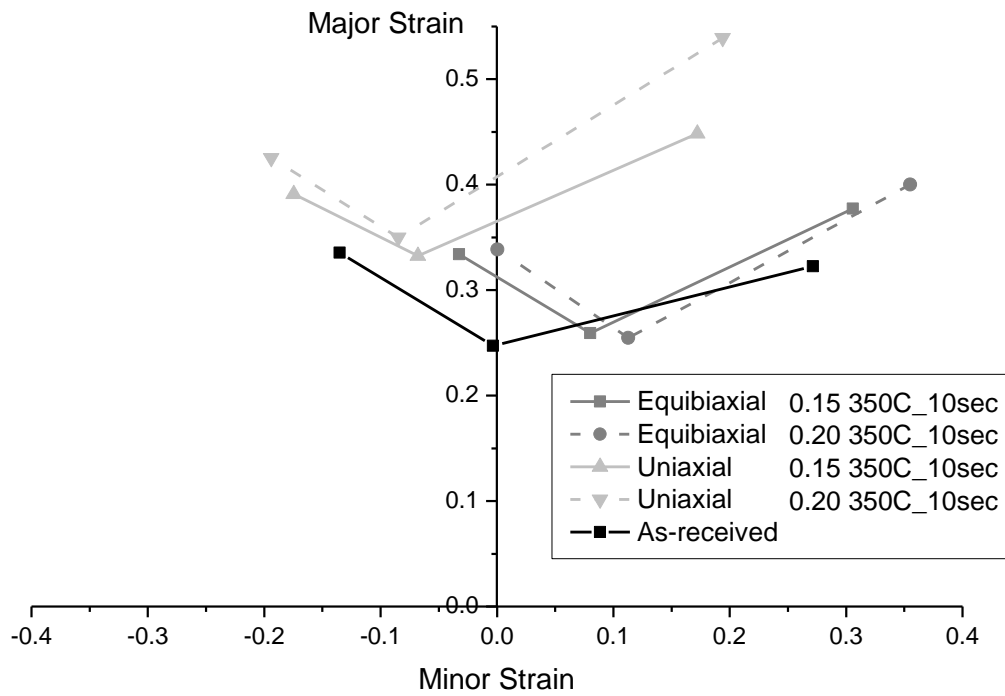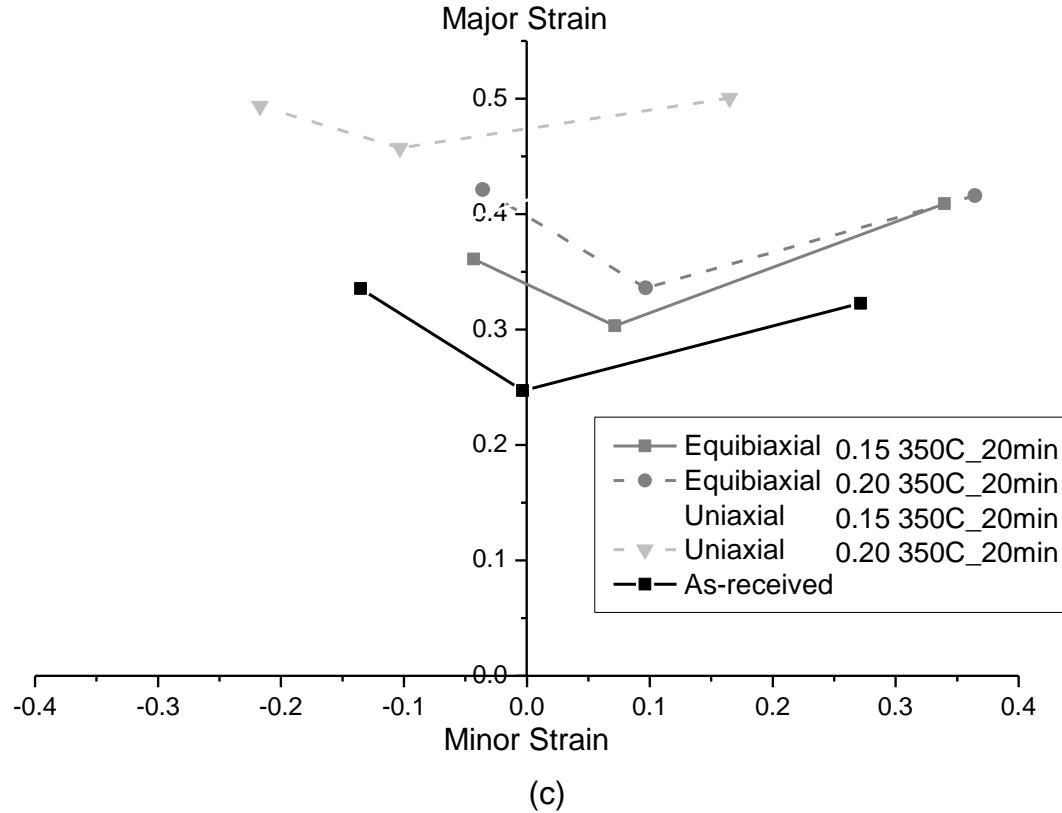
Figure 4.10 Pre-strain level effect on total effective FLDs: (a) no anneal, (b) annealing at 350°C for 10 seconds, and (c) annealing at 350°C for 20 minutes

4.4   STRESS-BASED FORMING LIMIT DIAGRAMS (σ-FLDs)

In this section, a method for generating stress-based forming limits diagrams (σ-FLDs) for two-stage forming with an intermediate annealing is presented. A constant called "*EPS* (effective plastic strain)" was proposed to account for the effects from pre-strain and annealing by overlapping the tensile flow curve of the recovery (or pre-strained) material with that of the as-received material. Then, the inputs of calculation of σ-FLDs only involved *EPS* and the incoming material properties. This method was validated by the results obtained using post-annealing material properties, i.e. Voce strain hardening

parameters and $\bar{R}$. The effects of annealing, pre-strain path and level on the σ-FLDs of post-annealing AA5182-O are also discussed.

4.4.1 Transformation between Strain and Stress Spaces

The Methodologies in the Calculation of Stress Spaces

In order to simplify the analysis, AA5182-O was assumed to exhibit in-plane isotropy, so Hill's quadratic normal anisotropic model [Hill, 1948] could be used to transform strains to stresses for plane stress condition ($\sigma_3 = 0$). This assumption would be valid for analysis as long as the same assumption is used for evaluating formability limits during finite element simulation of a panel or product. In the model, the material parameter is the normal anisotropy coefficient. The ratio of the minor stress, σ_2, to the major true stress, σ_1, is defined by parameter α:

$$\alpha = \frac{\sigma_2}{\sigma_1} \qquad (4.1)$$

Similarly, the ratio of the minor true strain rate, $\dot{\varepsilon}_2$, to the major true strain rate, $\dot{\varepsilon}_2$, is defined by the parameter β:

$$\beta = \frac{\dot{\varepsilon}_2}{\dot{\varepsilon}_1} \qquad (4.2)$$

Plasticity theory defines an effective plastic stress, $\bar{\sigma}$, that is a function of the stress tensor components and a set of material parameters. The effective stress function is given by

95

$$\bar{\sigma} = \sqrt{\sigma_1^2 + \sigma_2^2 - \frac{2\bar{R}}{1+\bar{R}}\sigma_1\sigma_2} \tag{4.3}$$

where $\bar{R}$ is the normal plastic anisotropic ratio, defined as Eq. (3.2)

The effective strain rate function is

$$\dot{\bar{\varepsilon}} = \frac{1+\bar{R}}{\sqrt{1+2\bar{R}}}\sqrt{\dot{\varepsilon}_1^2 + \dot{\varepsilon}_2^2 + \frac{2\bar{R}}{1+\bar{R}}\dot{\varepsilon}_1\dot{\varepsilon}_2} \tag{4.4}$$

The ratio between the effective stress and major stress is given by the parameter

$$\xi = \frac{\bar{\sigma}}{\sigma_1} = \sqrt{1+\alpha^2 - \frac{2\bar{R}}{1+\bar{R}}\alpha} \tag{4.5}$$

and the ratio between the effective strain rate and major strain rate is

$$\lambda = \frac{\dot{\bar{\varepsilon}}}{\dot{\varepsilon}_1} = \frac{1+\bar{R}}{\sqrt{1+2\bar{R}}}\sqrt{1+\beta^2 + \frac{2\bar{R}}{1+\bar{R}}\beta} \tag{4.6}$$

where β from Eq. (4.2) is then defined by

$$\beta = \frac{(1+\bar{R})\alpha - \bar{R}}{1+\bar{R} - \bar{R}\alpha} \tag{4.7}$$

and its inverse is

$$\alpha = \frac{(1+\bar{R})\beta + \bar{R}}{1+\bar{R} + \bar{R}\beta} \tag{4.8}$$

The effective strain is defined by the time integral of the effective strain rate as

$$\bar{\varepsilon} = \int \dot{\bar{\varepsilon}}dt \tag{4.9}$$

Butec et al. [2003] and Jain et al. [1996] have shown that the Voce law can suitably

96

describe the flow behavior of aluminum alloys by relating effective stress to effective strain as follows

$$\bar{\sigma} = A - B\exp(C\bar{\varepsilon}) \qquad (4.10)$$

where A, B and C are material constants. Including $\bar{R}$, the material constants were assumed to be the same in the calculation of post-annealing σ-FLDs at different pre-strain and annealing conditions.

A Method to Account for Pre-strain and Annealing Effects

The *EPS* was obtained by overlapping the tensile curve of recovery or pre-strained material with that of the as-received material for a best match of the plastic deformation region. The *EPS* was taken as the magnitude of the strain shift. For example, stress-strain curve of the 0.15 pre-strained specimen annealed at 350°C_10 seconds was shifted by a value of 0.06 true strain in order to overlap the hardening curve of the as-received condition, i.e., *EPS* = 0.06. Additionally, *EPS* was assumed to be constant at the same pre-strain and annealing condition for three different pre-strain paths. Figure 4.11 compares the true stress-true strain curves at different pre-strain and annealing conditions with the as-received data.

There is no switch in strain increment during FLD test. Therefore, if the true major and minor strains at *ith* DIC image are given as $\varepsilon_{1,i}$ and $\varepsilon_{2,i}$, then the principle stresses $(\varepsilon_{1,i}, \varepsilon_{2,i},)$ at this image can be calculated via the flow chart in Figure 4.12, where *i* starts from 1. The detailed assumption in the calculation was reported by Stoughton [2000].

97

When $i=1$, the initial true principle strains, $\varepsilon_{1,0}$ and $\varepsilon_{2,0}$, are set to zero. Pre-strain and

annealing effects are included by adding the *EPS* to the calculation of $\bar{\varepsilon}_i$.
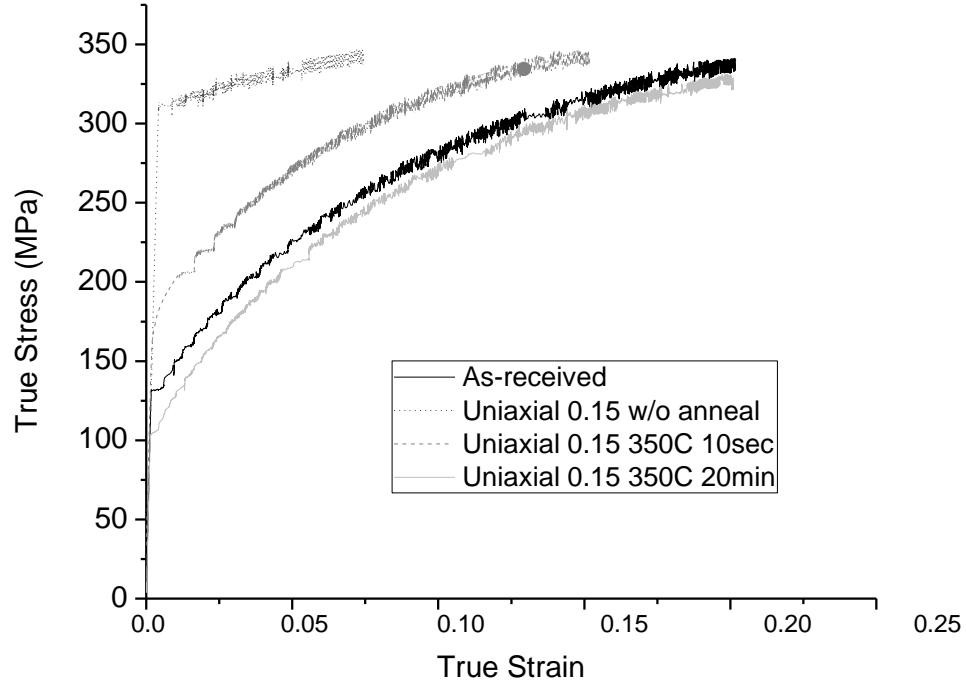
Figure 4.11 Stress-strain tensile curves of as-received, pre-strained and annealed
AA5182-O
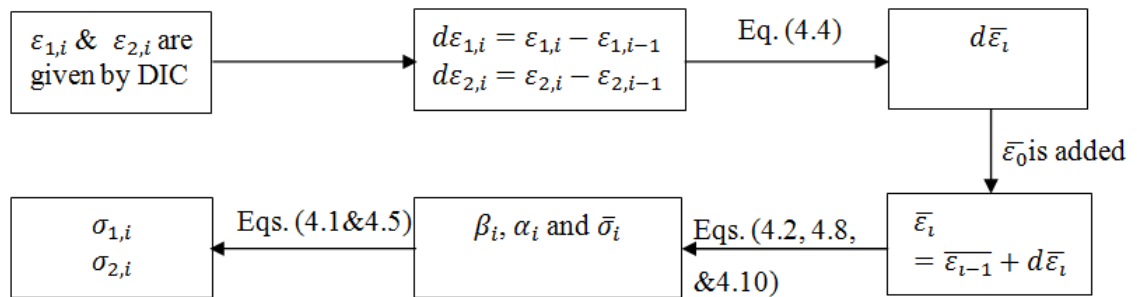
Figure 4.12 Flow chart of principle stress calculation at each DIC image

Validation of *EPS* method

The σ-FLDs calculated from *EPS* method (Approach I) was compared to the results

obtained by inputting the post-annealing material properties, i.e. the Voce parameters and

$\bar{R}$ (Approach II). As mentioned above, in the Approach I, the inputs are hardening

parameters of as-received material and *EPS*. In other words, the post-annealing stress-strain curve used in the calculation has the same shapes with as-received one but with different starting strain, i.e. *EPS*. The σ-FLDs were mapped in stress space by connecting the stress limits that were transformed from the corresponding strain limits.

The σ-FLDs calculated using these two approaches are compared in Figure 4.13, where (a) compares the σ-FLDs for three pre-strain paths annealed at 350°C for 20 minutes, and (b) summarizes the σ-FLDs for uniaxial pre-straining with different heat treatments and as-received σ-FLD is given as a reference. Using these two approaches, the calculated σ-FLDs are close to each other, which indicate the *EPS* method is suitable to capture the post-annealing strain hardening behavior.

The *EPS* method makes the calculation of σ-FLDs practicable, where the post-annealing mechanical properties are unnecessary. To test many post-annealing material properties is not feasible since the point to point in the material has different properties caused by uneven pre-strain or heat treatment. The fitted Voce parameters for post-annealed AA5182-O subjected to different pre-strain level and annealing are listed in Table 4.2, where the pre-strain is along uniaxial TD. The post-annealing $\bar{R}$ are listed in Table 4.3 and the effect of $\bar{R}$ on σ-FLDs is worth to investigate in the future. The following discussions on σ-FLDs are based on the *EPS* method.
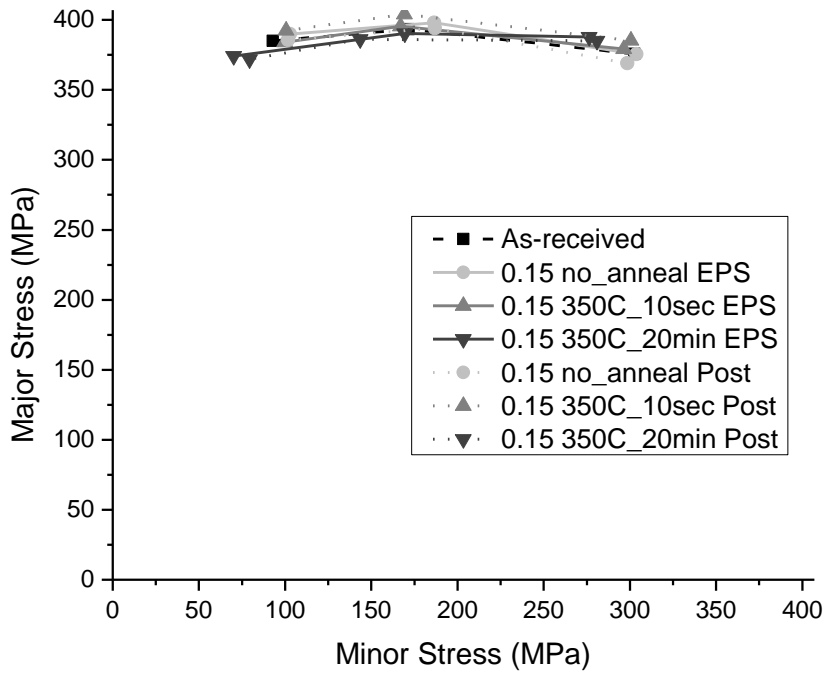
0.15 pre-strain & 350C_20min

(a)

(b)
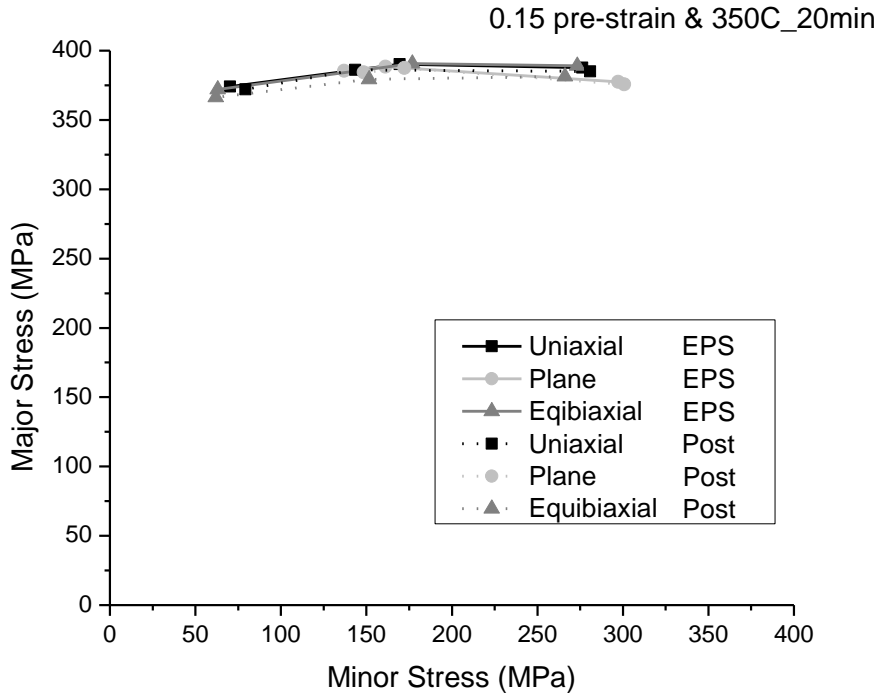
Figure 4.13 Comparison of *σ*-FLDs using *EPS* and post-annealing property methods: (a) three pre-strain paths for 350°C_20min and (b) uniaxial pre-strain for three different annealing conditions

Table 4.2 Post-annealing Voce parameters for 0.15 pre-strain

	A	B	C
no_anneal	352.18	43.65	-18.09
350°C_10 seconds	364.89	186.93	-14.51
350°C_20 minutes	349.23	243.52	-11.87

Table 4.3 The average anisotropy $\bar{R}$ coefficient of post-annealed AA5182-O

Annealing condition Pre-strain level	w/o anneal	350°C_10 seconds	350°C_20 minutes
0.15	0.854	0.847	0.950
0.2	0.794	0.854	0.955

4.4.2 Annealing and Pre-Strain Effects on σ-FLDs

For post-annealed material, the σ-FLDs present the forming limit criterion for stage 2 forming since the annealing and pre-strain effects were included in the calculation via *EPS*.

Annealing Effect

From Figure 4.13b, there are no obvious differences seen produced by different annealing treatments, and the σ-FLDs are close to as-received one. The as-received forming limit is included for reference. To confirm that, more conditions are compared in Figure 4.14, where the specimens were equibiaxial pre-strained for 0.20 equivalent true strains. The highest strain forming limit curve in Figure 4.8, anneal at 350°C for 20 minutes, overlaps the other curves in stress space. Furthermore, in both pre-strain cases (Figure 4.13b and 4.14), the stress-based forming limit curves at different annealing conditions (no_anneal, 350°C_10 seconds, and 350°C_20 minutes), converge to a single curve that overlaps the curve of the as-received condition. A slight variation (around
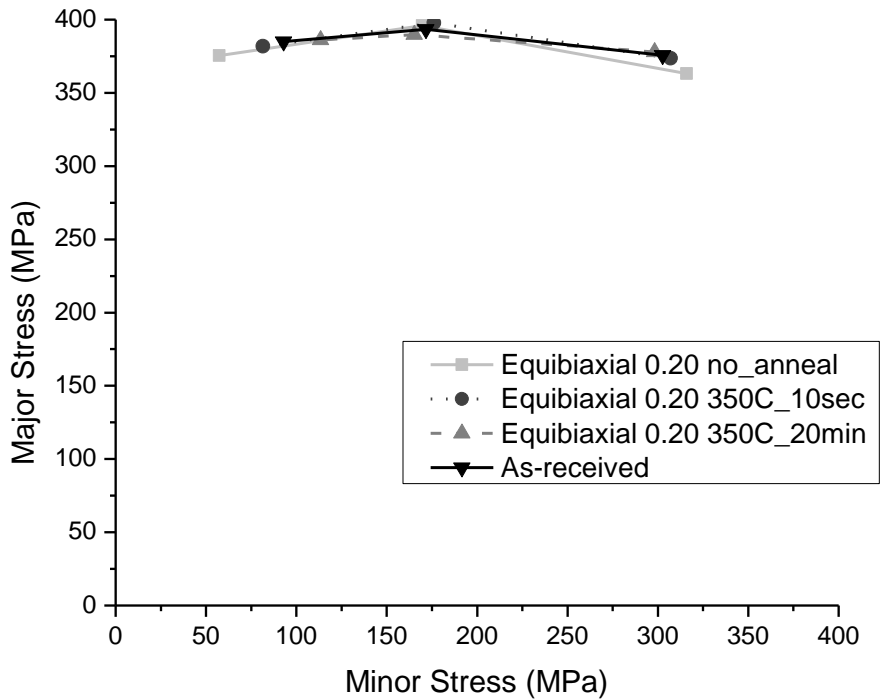
Figure 4.14 Annealing effect on σ-FLDs

20MPa) in major stress is seen for the uniaxial pre-straining (Figure 4.13b), which is only 5%

of the stress limit (above 400 MPa).

Pre-Strain Path and Level Effects

Figures 4.13a shows the σ-FLDs of specimens at three different pre-strain paths (i.e.

equibiaxial, plane, and uniaxial pre-strain) followed by 350°C_20 minute annealing.

However, the forming limit curves of post-annealed material in stress space overlap each

other. This point is clear in Figure 4.15 which summarizes the σ-FLDs of specimens

pre-strained at three different pre-strain paths to different levels and annealed at 350°C for

10 seconds. The forming limit curves converge to a single curve that is close to the

forming limit curve of the as-received material. All of these cases demonstrate the

independence of σ-FLDs on pre-strain path. This agrees to the analysis of Stoughton [2000] who showed that strain path has on influence on the stress-based forming limit of materials pre-strained along various paths.
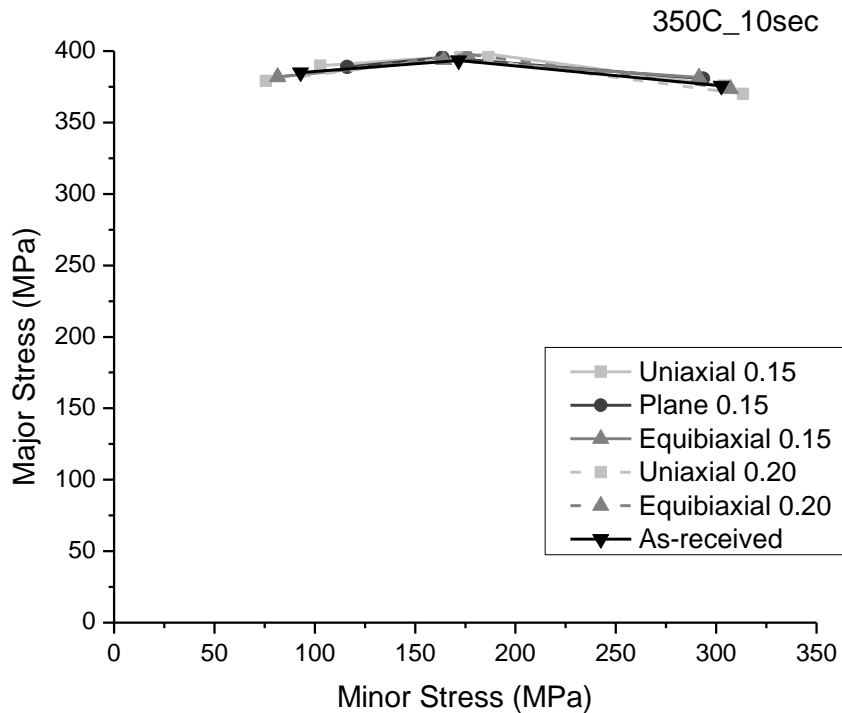
Figure 4.15 Pre-strain path and level effects on σ-FLDs

In addition to the pre-strain path effect, the independency of pre-strain level is seen in Figure 4.15, where two pre-strain levels are compared (0.15 and 0.20). The strain space shows that a high pre-strain level usually increases the total effective forming limit (see Figure 4.10). In stress space, the forming limit curves of the materials pre-strained to different levels are identical to the forming limit of the as-received material.

The Stress History

In previous results, it was shown that the stress-based forming limits of post-annealed

AA5182-O are independence on annealing and pre-strain history. This finding is reinforced when considering the principle stress history. Figure 4.16 presents the stress histories of the point of maximum strain before fracture (section 4.2.2) for different combinations of pre-strain and annealing conditions, where (a) is using *EPS* method, and (b) is using post-annealing material properties. The case presented corresponds to the plane strain LDH test. Both methods show that the stress history curves start from different locations in the plots; however, they convert to a single failure point. 0.2 pre-strains have higher starting locations in stress space than 0.15 pre-strains, but this difference vanishes with a long annealing time (20 minutes). The pre-strained specimens with the no_anneal condition have more stored energy of cold work that provides a higher starting location. Annealing, however, relieved or eliminated the effects of cold work and provided lower starting positions in stress space. In fact, for the long annealing time of 20 minutes, the material was essentially "reset" and behaved similar to the as-received specimen. The agreements of these two approaches confirm that *EPS* is a proper method to proximate the residual cold work in the recovery or pre-strained material.
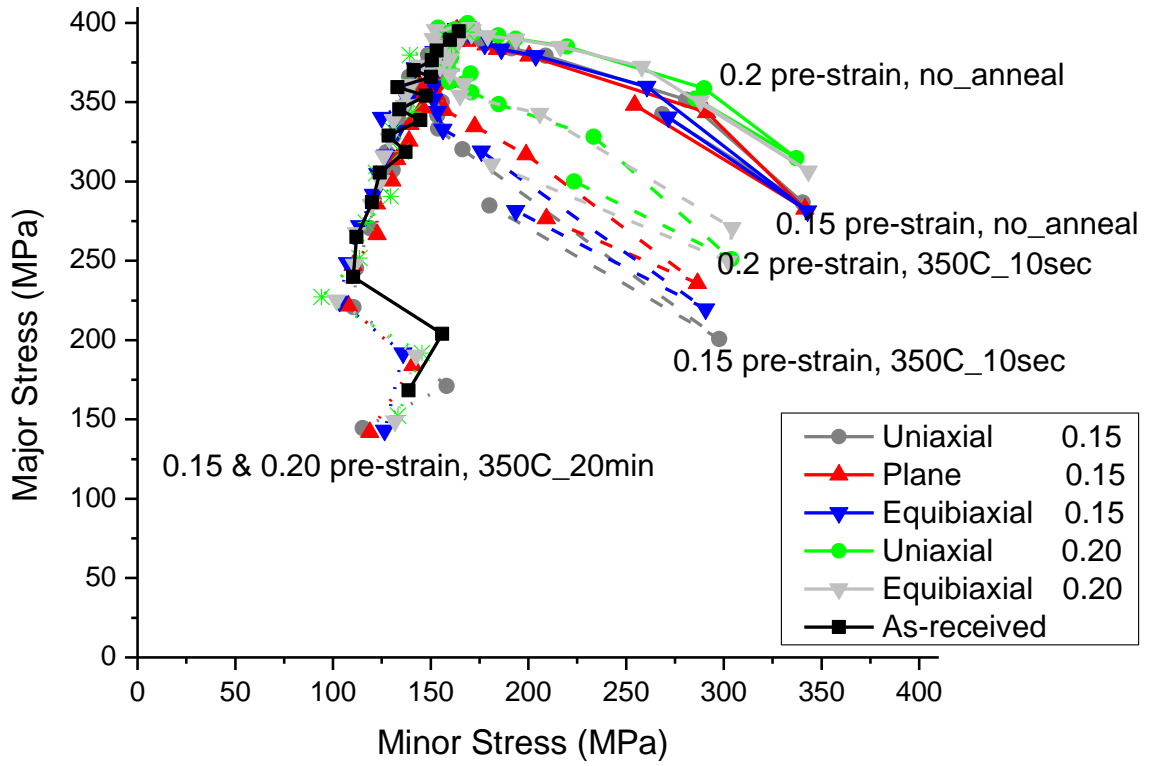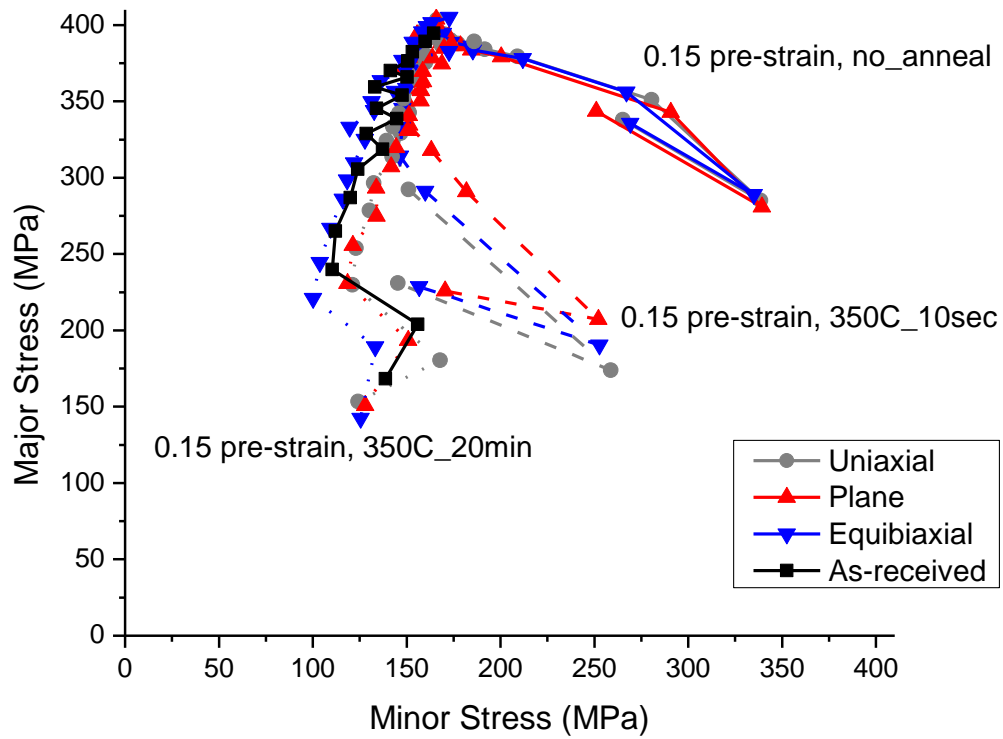
Figure 4.16 Calculated principle stress history for a near plane strain condition in 50mm-LDH test: (a) using *EPS* method and (b) using post-annealing properties

4.5   SUMMARY

A combined experimental/theoretical method for generating stress-based forming limits of AA5182-O for two-stage forming with an annealing was presented.   The strain history during formability testing was recorded via DIC, which made possible observation of changing strain paths during different tests as seen, for example in the near-plane strain LDH test.   DIC was also used to identify the onset of localized necking that was applied to define the forming limit.   Hill's quadratic normal anisotropic model [1948] and the Voce hardening law were used to transform the forming limits strain space to stress space by assuming AA5182-O exhibited close to in-plane isotropy, which can reduce the calculation cost.   In the calculation of σ-FLDs, a constant, *EPS*, was proposed to account for the effects of pre-strain and annealing; and this approach was validated by the results using real post-annealing material properties as inputs.   The effects of process parameters, i.e. pre-strain levels, paths and subsequent annealing, on the ε-FLDs and σ-FLDs were investigated.

In the strain space, both post-annealing and total effective FLDs display dependency on pre-strain and annealing parameters.   The effect of annealing is relatively easy to understand how it can raise the forming limits, and with longer annealing time more improvement is observed.   However, too much heat treatment can lead to grain coarsening and associated degradation of mechanical properties (Chapter 3.3).   The effect of pre-strain is more complicated.   A high pre-strain level reduces the formability of unannealed material, and increases the forming limits after long annealing times because of

the high driving force for recrystallization/grain growth. Pre-strain path has very few impacts on the post-annealing FLDs; however, this does shift the total effective forming limit curve along the pre-strain direction. For the no_anneal cases, pre-strain in uniaxial tension raises the formability along plane strain and equibiaxial tension; plane pre-strain increases the formability in both uniaxial and equibiaxial directions; equibiaxial pre-strain decreases the formability along uniaxial and plane strain paths. For annealed cases, the improvement in formability is apparent for all three pre-strain paths, except a few data points with low formability near plane strain of the equibiaxial pre-strained specimen followed by 10-second annealing.

The strain-based forming limit shows apparent dependence on pre-strain and annealing; however, in stress space the forming limits converge to a single curve comparable to the as-received forming limit. This result validates Stoughton's [2000] finding on the independence of stress-based forming limits on pre-strain. Furthermore the results confirm that the σ-FLD is uninfluenced by annealing. Although Hill's quadratic normal anisotropic model applied in this study is not the best material model for aluminum alloys, as Stoughton [2000] indicated, this convergence is unchanged by different plastic potential functions.

This convenient approach in developing the forming limit of two-stage forming with annealing is important to the FEM analysis of such a complicated forming process. The inputs in the stress calculation are not complex since only the as-received material

constants are needed. Thus, it is not necessary to do many post-annealing tests. The pre-strain and annealing effects can be introduced by the constant (*EPS*) that is obtained by overlapping the post-annealing and as-received stress-strain curves.

REFERENCES

Arrieux R., Bovin, M., Le Maître, F., (1987), "Determination of the forming limit stress curve for anisotropic sheets,"*CIRP Annals - Manufacturing Technology*, 36, 195–198.

ASTM E112-96, (2004), "Standard test methods for determining average grain size," ASTM International, West Conshohocken, PA.

ASTM E8/E8M-09, (2009), "Standard Test Methods for Tension Testing of Metallic Materials," ASTM International, West Conshohocken, PA.

ASTM E2218-02, (2008), "Standard test method for determining forming limit curves," ASTM International, West Conshohocken, PA.

Barata da Rocha, A., Barlat, F., Jalinier, J.M., (1984–1985), "Prediction of the forming limit diagrams of anisotropic sheet in linear and non-linear loading," *Materials Science and Engineering*, 68, 151–164.

Beaver, P. W., (1982/1983), "Localized Thinning, Fracture and Formability of Aluminum Sheet Alloys in Biaxial Tension," *Journal of Mechanical Working Technology*, 7, 215-231.

Bressan, J. D., Williams, J. A., (1983), "The Use of A Shear Instability Criterion to Predict Local Necking in Sheet Metal Deformation," *International Journal of Mechanical Sciences*, 25, 155-168.

Butuc, M. C., Gracio, J. J., Barata da Rocha, A., (2003), "A theoretical study on forming limit diagrams prediction," *Journal of Materials Processing and Technology*, 142, 714-724

Correlated Solutions, Inc., Columbia, SC. 8 August 2011,
<http://www.correlatedsolutions.com/index.php/principle-of-digital-image-correlation>

Chu, C. C., (1982), "An investigation of the strain path dependence of the forming limit curve,"
International Journal of Solids *and Structures*, 18, 205–215.

Dewhurst, P., Boothroyd, G., (1981), "Stretch Forming of Sheet Metal: a Mechanism of Deformation Involving Diffuse Neck Interaction," *CIRP Annals - Manufacturing Technology*, 30, 185-188.

Goodwin, G. M., (1968), "Application of strain analysis to sheet metal forming in the press shop," *SAE paper*, No. 680093.

Gotoh, M., (1985), "A class of plastic constitutive equations with vertex effect—IV: applications to prediction of forming limit strains of metal sheets under nonproportional loadings," *International Journal of* Solids *and Structures*, 21, 1149–1163.

Graf, A. and Hosford, W. F., (1993), "Effect of changing strain paths on forming limit diagram of Al 2008-T4," *Metallurgical   Transaction A*, 24A, 2503–2512.

Gronostajski, (1984), "Sheet metal forming limits for complex strain paths," *Journal of Mechanical Working Technology*, 10, 349–362.

Hill, R., (1948), "A theory of the yielding and plastic flow of anisotropic metals," *Proceedings of the Royal Society of London A*, 193, 281-297.

Humphreys, F. J., Hatherly, M., (2004), "Recrystallization and related annealing phenomena," second ed., Elsevier Ltd., Oxford.

Jain, M., Lloyd, D. J. and Macewen, S. R., (1996), "Hardening laws, surface roughness and biaxial tensile limit strains of sheet aluminum alloys," *International Journal of Mechanical Sciences*, 38, 219-232

Keeler S.P., Backhofen W.A., (1964), "Plastic instability and fracture in sheet stretched over rigid punches," *ASM Transactions Quarterly*, 56, 25-48.

Krajewski, P. E., (2007), "Methods for Production of Stamped Sheet Metals Panels," US Patent 7,260,972, B2.

Kuroda, M., and Tvergaard, V., (2000), "Effect of strain path change on limits to ductility of anisotropic metal sheets," *International Journal of Mechanical Sciences*, 42, 867–887.

Kuwabara T., Yoshida, K., Narihara, K., Takahashi, S., (2005), "Anisotropic plastic deformation of extruded aluminum alloy tube under axial forces and internal pressure," *International Journal of Plasticity*, 21, 101–117.

Lee, T. M., Hartfield-Wünsch, S. E., Xu, S., (2006), "Demonstration of the Preform Anneal Process to Form a One-Piece Aluminum Door Inner Panel," *SAE Paper*, No. 2006-01-0987.
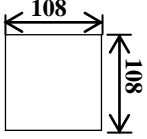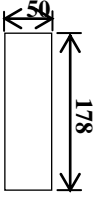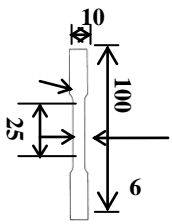
Li, J. J., Kim, S, Lee, T. M., Krajewski, P. E., Wang, H., Hu, S. J., (2011), "The effect of prestrain and subsequent annealing on the mechanical behavior of AA5182-O," *Materials Science and Engineering A*, 582, 3905-3914.

Li, J. J., Hu, S. J., Carsley, J. E., Lee, T. M., Hector, Jr., L. G., Mishra, S., "Post Annealing Mechanical Properties of Pre-strained AA5182-O Sheet," (2011), accepted by *ASME Journal of Manufacturing Science and Engineering*.

Marin J., Hu, L. W., Hamburg, J. F., (1953), "Plastic stress–strain relations of Alcoa 14S-T6 for variable biaxial stress ratios," *Transaction of the American Society of Metals*, 45, 686–709.

Nakazima, K., Kikuma, T., Hasuka, K., (1968), "Study on the formability of steel sheets," Yawata Tech. Rep, 264, 8517–8530.

Needleman, A., and Tvergaard, V., (1984), "Limits to formability in rate-sensitive metal sheets," In: Carlsson, J., Ohlson, N.G. (Eds.), Mechanical Behavior of Materials IV, Proc. 4th Int. Conf., Stockholm, Sweden, 15–19 August 1983, 51–65.

Reedlunn, B., Daly, S., Daly, Hector Jr., L., Zavattieri, P., Shaw, J., (2011), "Tips & Tricks for Characterizing Shape Memory Wire Part 5: Full-field Strain Measurement by Digital Image Correlation," *Experimental Techniques*, Accepted

Stoughton, T. B., (2000), "A general forming limit criterion for sheet metal forming," *International Journal of Mechanical Sciences*, 42, 1–27.

Stoughton, T. B., (2001), "Stress-based forming limits in sheet-metal forming, "*ASME Journal of Engineering Materials and Technology*, 123, 417–422.

Stoughton T. B., and Zhu, X., (2004), "Review of theoretical models of the strain-based FLD and their relevance to the stress-based FLD," *International Journal of Plasticity*, 20,1463–1486.

Wu, P. D., Graf, A., MacEwen, S.R., Lloyd, D. J., Jain, M., Neale, K. W., (2005), "On forming limit stress diagram analysis," International Journal of Solids and Structures, 42, 2225–2241.

Yoshida, K., Kuwabara, T., Narihara, K., Takahashi, S., (2005), "Experimental verification of the path-dependenceof of forming limit stresses," *International Journal of Forming Processes*, 8, 283–298.

Yoshida, K., and Kuwabara, T., (2007), "Effect of strain hardening behavior on forming limit stresses of steel tube subjected to nonproportional loading paths," *International Journal of Plasticity*, 23, 1260-1284.

Zavattieri, P. D., Savic, V., Hector Jr., L.G., Fekete, J. R., Tong, W. Xuan, Y., 2009, "Spatio-temporal Characteristics of the Portevin-Le Chatelier Effect in Austenitic Steel with Twinning Induced Plasticity," *International Journal of Plasticity*, 25, 2298-2330.

Zhao, L.R., Sowerby, R., Sklad, M.P., (1996), "A theoretical and experimental investigation of limit strains in sheet metal forming," *International Journal of Mechanical Sciences*, 38, 1307–1317.

111

APPENDIX

SPECIMEN GEOMETRIES IN FLD DEVELOPMENT USING LDH AND UNIAXIAL TENSILE TESTS

Strain path in FLD	Specimen geometry	Forming method	Test System
Equibiaxial tension	108 × 108	50mm-LDH (CGA, DIC)	ITC SP150 press
Plane Strain	50 × 178	50mm-LDH (CGA, DIC)	ITC SP150 press
Uniaxial tension	10, 100, 25, 6 [ASTM E8/E8M-09, 2009]	Tensile test (DIC)	Instron 5582 universal testing machine

CHAPTER 5

CONCLUSIONS AND FUTURE WORK

5.1   CONCLUSIONS

Preform annealing is an important technology to achieve high deformation stamping

of lightweight vehicle materials, such as aluminum alloy 5xxx, at room temperature.   For

this new technology, little research on the changes of material behavior has been conducted.

However, such research has significant impacts on process simulation, design and

optimization. A most common tool to current FEM simulation is ε-FLDs, which are not

applicable for this two-stage forming with annealing since the ε-FLDs are dependent on

preform and annealing history. To fill this gap, this thesis aims to understand how preform

and annealing influence the mechanical behavior of aluminum alloy 5182-O and to

develop a practical forming limit criterion for this multistage forming process. This

research will be critical to the accurate simulation and optimization for this process that

involves preform, annealing and 2-stage forming.

The major achievements/findings of this dissertation can be summarized in three

parts:

1) *Systematic investigation on the effects of uniaxial pre-strain level, annealing time and temperature on tensile properties and development of kinetic modeling for static recovery and recrystallization of AA5182-O:* The improvement in formability of Al alloys through preform annealing was seen from the increase of total effective elongation that reaches 40% after 20% pre-straining. The different responses of post-annealing elongation and yield stress to process variables (i.e. pre-strain, annealing temperature and exposure time) indicate that it is possible to control the yield stress to different values while ensuring the same post-annealing elongation through different combinations of pre-strain and annealing. An interesting phenomenon is that strain-hardening exponent (n) shows a linear relationship with log yield stress while strength coefficient (K) does not. In addition to the empirical modeling of yield stress, the strain-hardening exponent can also be expressed in terms of process variables.

2) *Research on the relationships between process variables versus mechanical behavior and its relation with microstructure/texture:* For this purpose, statistical methods, such as design of experiment and ANOVA analysis, were applied to identify the important process variables as well as their effects on the mechanical properties. For example, pre-strain and annealing have opposite effects on strength and elongation; and annealing has more impacts

on anisotropy than pre-strain level. The microscopic/EBSD analysis shows that the post-annealing strength is related to grain size and grain average misorientation and *R*-value is strongly dependent on texture.

3) *Development of forming limit criterion for this two-stage forming with annealing treatment*: In the development of FLDs, stereo digital image correlation was applied to capture the strain mappings during LDH tests and provide direct observations of localized necking along different strain paths. Strain-based forming limits that are currently widely used in the FEM exhibit dependencies on pre-strain and annealing histories that differ from point to point in the material, and hence are difficult to define and apply. The stress-based forming limits constructed from a constant, "effective plastic strain (*EPS*)" show the independence on pre-strain levels, strain paths and annealing, and converge to a single forming limit curve that is close to the stress-based forming limit calculated for the as-received material. The constant (*EPS*) can account for the pre-strain and annealing effects. In this approach, the calculation of stress space from strain space will only involve as-received material properties, which is applicable in general to the simulation of this complex forming process. This method was validated to the approach using post-annealing material hardening parameters.

The original contributions of this research can be summarized as follows:

1) Two kinetic models of AA5182-O for static recovery and recrystallization were developed. In the models, yield stress is predictable using the process parameters. These two constitutive models will improve the FEM simulation of annealing process that usually assumes the material properties were reset to as-received condition, but in the reality it is not true. In addition, the constitutive models, for example, can be applied in the microstructure-based multi-scale modeling which incorporates the microstructural inputs [Krajewski, et. al. 2010].

2) The links between AA5182-O mechanical properties and preform annealing process variables were investigated and the procedures for experiments and analysis were developed.

3) The relationship between microscopic behavior of AA5182-O and its macroscopic properties were described.

4) A combined experimental/theoretical method for generating σ-FLDs is presented for this two-stage forming with annealing process. This approach can capture the preform and annealing effects through a constant, effective plastic strain, and simply the stress calculation by involving only as-received material properties.

5) Stress-based forming limits are shown to be independent of both preform strain and annealing history. With DIC, the strain history was recorded,

which is different from the circle grid analysis where only the initial and last strain stages can be observed. Stress history transformed from the strain history shows that material starts to yield from different positions in the stress space caused by different cold work (preform) and recovery (annealing) treatments but converges to a single failure point. The single forming limit criterion will impact the simulation of annealing aided multistage forming process and the local annealing strategies when the forming and recovery histories differ from point to point in the material.

5.2 FUTURE WORK

Aluminum alloy 5182-O is a specific example of the application of preform annealing. The extended research may include the following directions:

1) *Preform annealing on 6xxx aluminum alloys:* 6xxx aluminum alloys (Al-Mg-Si) are heat-treatable with an artificial aging temperature of 160-180°C. To preform and anneal this type of alloys will become more complicated. The annealing and cooling rates will be critical factors as well as the pre-strain, annealing temperature and holding time.

2) *Combining DIC with other characterization methods and plasticity theories:* DIC is a promising experimental technique for exploring deformation mechanisms. With high-speed cameras, images were captured at a rate of 10,000 frames per

117

second which makes it possible to observe the necking and fracture development directly. This observation will help to paint a more complete picture in the development of plasticity and fracture theories. The accuracy of DIC is up to a few hundredth pixels; hence it is practical in the future to combine with other microscope techniques to develop multi-scale modeling for deformations.

3) *Developing multi-scale model to link macro- and micro- behavior aim to improve the process design:* Understanding the links between process variables and material behavior at macro- and micro- scale or how the behavior at one scale affects the properties of another, is an important direction.

REFERENCES

Krajewski, P. E., Hector Jr., L. G., Du, N., Bower, A. F., (2010), "Microstructure-based multiscale modeling of elevated temperature deformation in aluminum alloys," Acta Materialia, 58, 1074-1086.